Redox Targeting Insights and Applications for High-Energy-Density Redox Flow Batteries

Atchuthan Gopalan

A dissertation

submitted in partial fulfilment of the

requirements for the degree of

Doctor of Philosophy

University of Washington

2024

Reading Committee:

Daniel Gamelin, Chair

Brandi Cossairt

Douglas Reed

Program Authorized to Offer Degree:

Chemistry

University of Washington

Abstract

Redox Targeting Insights and Applications for High-Energy-Density Redox Flow Batteries

Atchuthan Gopalan

Chair of Supervisory Committee:

Professor Daniel R. Gamelin

Department of Chemistry

Decarbonizing the grid has been gaining momentum with the shift away from fossil fuels to renewable energy. The addition of energy storage systems will only accelerate this transition and the rapid phase out of conventional power plants. Aqueous redox flow batteries are a potential solution, providing a low-cost storage solution for long-duration energy storage. However, the main barrier to adoption is the low energy density, which require rather large installations to meet energy storage demands. Redox targeting is a solution that breaks the energy density pinning based on the electrolyte solubility limits. This redox chemistry combines the high-energy-density of solid-state media with the low-cost and scalable redox flow battery architecture. Chapter 1 describes the technological developments of redox flow batteries and the current challenges for wide-scale technology adoption. Chapter 2 employs a sodium superionic conductor with aqueous organic redox mediators. Through high surface area macrostructures and solution potential tuning, high material utilization and the largest volumetric capacity enhancement is demonstrated in aqueous anolytes. Chapter 3 describes a new spectrochemical method to probe the ionic diffusion kinetics in Prussian blue/ferricyanide redox targeting systems. The intercalant identity dramatically affects Prussian blue charge-discharge kinetics. The differences reflect the charge-compensation mechanisms and their impact on charge-discharge rates.

Table of Contents

List of Figures

List of Tables

Chapter 1. Introduction

1.1 Renewable Energy and Energy Storage

The global climate has fluctuated throughout history and even endured long periods of extreme weather, the ice age 15,000 years ago is the most recent example but there are numerous examples from data extracted from polar ice cores.[1] The ice age was the consequence of a combination of natural occurrences, such as a minor change to the Earth's orbit, the solar energy output by the Sun, atmospheric composition, ocean currents, and volcano activity.[2] However, since the dawn of civilization, the weather patterns have been mild and stable, providing an environment for humans and life to thrive. The industrial revolution in the 18th century marked the first instance of human activity affecting the global climate.[3] During the revolution, factories were powered by burning coal and today we continue the combustion of fossil fuels for manufacturing, electricity generation, and transportation. Fossil fuels emit greenhouse gases during combustion which adds small molecules that are efficient absorbers of infrared energy. These gases trap some of the infrared energy in the atmosphere and reflect them back to Earth's surface. The most notable greenhouse gas, carbon dioxide (CO_2), is of particular interest because of its significant, and growing, contribution to global warming which can be directly linked to the combustion of fossil fuels. Since the industrial revolution, CO_2 levels globally have increased 35%.[4] Continuing this course of trajectory is widely regarded as unsustainable, leading to higher average surface temperatures and more erratic weather patterns.

Countries worldwide are targeting to curtail global warming to fulfil the Paris agreement, an agreement by 196 parties to limit global temperature increase to 2ºC above pre-industrial levels.[5] Transportation, industry, commercial, residential, and electricity generation are the five sectors that contribute to CO_2 emissions. Aggressively pursuing efficiency improvements and decarbonization in these sectors can drastically reduce greenhouse gas emissions and achieve

net zero emissions by 2050. Currently, fossil fuels remain the dominant source for grid electricity generation, making up ~60% of the grid's capacity.[6] There are various renewable sources contributing to the grid but two of the major sources, wind and solar, suffer from intermittency. Solar is impacted by the number of daylight hours and the weather. In the summer months, solar does contribute more to the electricity supply, however, this is reversed in the winter months. Furthermore, wind is highly unpredictable all year-round. These two sources contribute ~14% of the US grid electricity generation.[6]

Currently, renewable sources make up a small proportion of the total electricity production, accounting for 21% in the US.[6] However, renewables installations have been rapidly developed recently with total renewable energy production doubling since 2010. This expansion of renewable sources has resulted in energy production from renewables surpassing both nuclear and coal in 2020. This has largely been driven by the development of wind and solar which have grown by about 60 and 120-fold, respectively, in the last 20 years. The falling manufacturing costs and more efficient modules have made renewables technology economically competitive with their fossil fuel counterparts. This momentum is likely to continue accelerating with further reductions of manufacturing cost of solar and turbine modules with many countries increasing investment domestically for their own renewable industries to meet emissions targets and to boost energy security. Ultimately, renewable technologies will not only displace fossil fuels, but replace them all together.

Renewables sources, such as wind and solar, possess an Achilles heel – they are intrinsically intermittent sources. The Sun does not shine all the time and the wind does not always blow, but human electricity demand is often regular and predictable (Figure 1.1). The modern world has become accustomed to energy reliability, so maintaining this is a requirement for renewable energy sources too. To overcome this hinderance, the grid will require cheap and efficient energy storage system (ESS) technologies to compensate during peak demand hours

and/or lack of supply from energy sources. ESS solutions can store excess electricity from renewables when the demand is low, and then deploy the stored electricity when the demand is high. By building out the ESS grid infrastructure, gigawatt hours of electricity can be stored and deployed on a daily basis, galvanizing the transition to renewables.

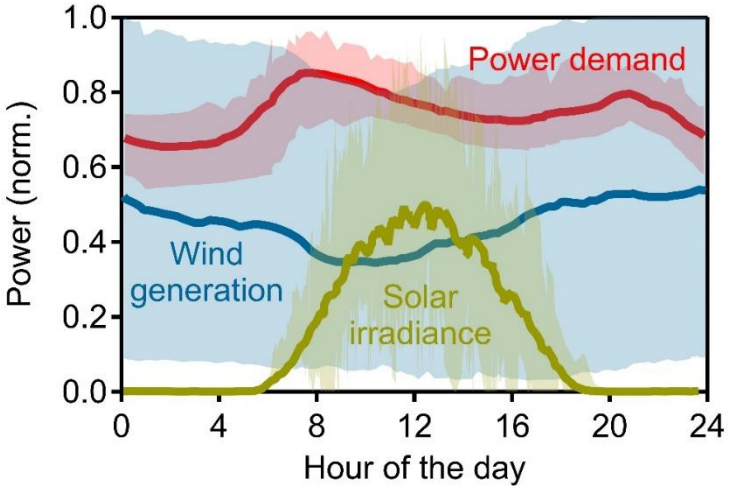

Figure 1.1 Normalized energy demand, wind generation, and solar irradiance. Bold traces indicate the average demand/energy production. Shaded regions indicate the variability of the demand/energy production. Adapted from ref.[7]

When determining the suitability of an ESS technology, the system power rating and the discharge time at the power rating are important factors for consideration.[8,9] The total capacity of the system is simply the multiplication of these two values. As a storage and reserve power source for renewables, discharge times should be in the hours range and the power rating should be at least a MW.

Pumped hydroelectric storage (PHS) is the most well-established and developed ESS. PHS configuration is two water reservoirs at different elevations, which are connected via an underground water channel. There is a turbine toward the base of the channel that can pump water to the upper reservoir to store excess energy, or water can flow down to the lower reservoir and drive the turbine to deploy energy to the grid. PHS purpose is like a giant battery in that energy

can be stored and released when needed, however, electrical energy is stored as potential energy in PHS. PHS currently accounts for 96% of all grid-scale energy storage in the US and is comprised of 43 PHS plants, making up 99% of electrical energy storage (GWh).[10] It is the favored ESS technology as a low-cost technology option for 4 – 16 hour duration storage. However, PHS is a geographically constrained technology, requiring mountainous areas to install the two reservoirs and the availability of vast amounts of water, making it infeasible in many locations. Furthermore, PHS has very high initial construction costs and potential negative environmental impacts on the local ecosystem.[11-13]

Electrochemical solutions are an alternative to existing mature technologies. Electrochemical solutions can outperform PHS on both volumetric energy density and round-trip energy efficiency, therefore, requiring less land to install a system of comparable total output.[14] Furthermore, they have significantly less environmental impacts and geographical restrictions than PHES, making the technologies appealing to more countries. The two most promising electrochemical ESSs are lithium-ion batteries (LIBs) and aqueous redox flow batteries (ARFBs).

LIBs initial interest arose in the 1960s with government militaries pursuing high-energy density storage technologies.[15] In the following decades, researchers identified numerous lithium intercalation hosts, outlining the ideal cathode and anode materials, as well as the supporting electrolytes.[16-18] It was in the late 1980s that the first LIB were commercially available by Asahi Chemical which was acquired and then further developed by Sony for portable electronic devices and electric vehicles.[15] Significant research and development has been undertaken on LIB technology, combined with huge reduction in manufacturing costs of battery modules has led to the prevalence of LIBs in a variety of modern portable electronic devices. The chemistry in small devices can be scaled up to larger devices, such as electric vehicles or stationary grid-scale batteries, simply by installing more battery cells within battery modules. The modular design and high energy density is why LIBs are the best ESS for many applications. LIB ESS has been installed

on various national grids within the past decade in efforts to increase the grid's storage capacity and to improve the grid resiliency as nations are shifting more to renewable energy production. The largest LIB ESS is the Moss Landing Energy Storage Facility with a 400 MW and 1,600 MWh capacity currently. The site is planning to expand to this to 750 MW and 3000 MWh.[19]

LIB ESS will for now be the preferential choice for grid-scale electrochemical ESS. However, many governments have targets to bring down the cost of storing excess electricity.[20, 21] Ultimately, LIBs costs are associated with the battery capacity requirements, the greater the energy and power needed, then the larger the volume of the cathode and anode. To meet the high energy storage requirements, thousands of battery cells will have to be assembled into modules and battery packs to form the larger collective grid-scale LIB. Enlarging the electrodes comprised of critical minerals increases the costs of a system per unit energy. Furthermore, thermally managing all the battery cells is not trivial and requires additional complex infrastructure to address the safety concerns for grid-scale LIBs.

1.2 Aqueous Redox Flow Batteries (ARFBs)

As opposed to LIBs, ARFBs are suitable for long-duration energy storage due to their unique architecture which decouple energy and power, are easily scalable, possess inherent safety features, and have minimal environmental impact.[22, 23] RFBs are comprised of two electrolyte reservoirs, whereby the electrolytes are pumped through an electrochemical cell, shuttling electrons from one reservoir to the other, resulting in the reversible conversion of chemical energy to electrical energy as shown in Figure 1.2. The electrochemical cell consists of two electrodes (a graphite block and porous carbon fiber fabric assembly) and an ion-exchange membrane. The chemical energy is stored in the dissolved redox-active species present in electrolyte reservoirs. The electrolyte with more reductive electrolyte is called the negative electrolyte or "anolyte", whereas the more oxidative electrolyte is called the positive electrolyte

or “catholyte”. The electrolytes in each tank will have their signature reduction/oxidation potentials, passing electrons from the anolyte to the catholyte when discharging and vice versa under charging. The ion-exchange membrane is selective to permit the diffusion of small ionic species, which conserve charge neutrality and avoids resistance build-up, but prevents the diffusion of the redox-active species. The total energy of the system depends on the electrolyte volume, concentration of redox-active species, and the cell potential, whereas the power is determined by the active surface area of the electrodes within the electrochemical cell. This distinct decoupling of energy and power enables either to be scaled independently, hence, RFBs are highly flexible with their modular design to tailor the energy and power rating. A key factor for economically evaluating an ESS is the system cost per kWh of stored energy, and for RFBs that is mainly dependent on the cost of the electrolytes rather than the electrochemical cell components, making it cheaper than LIBs.

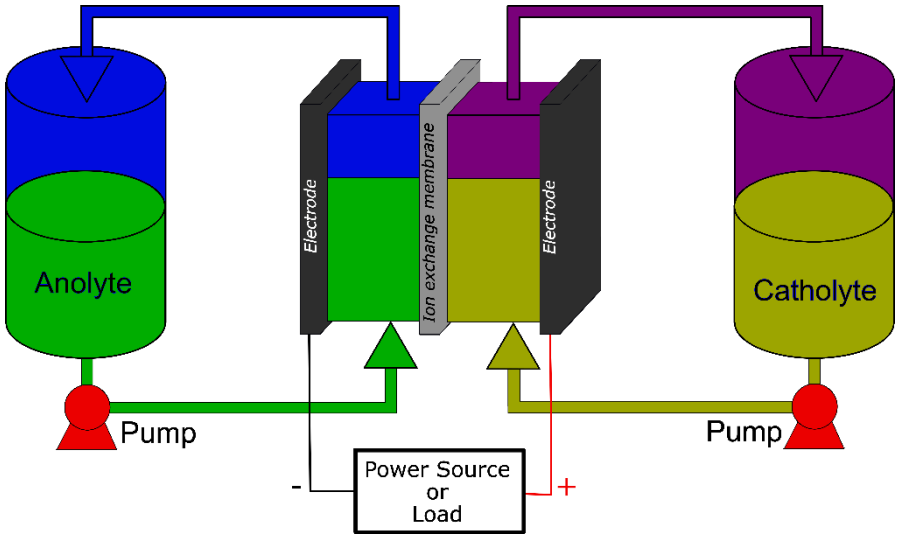

Figure 1.2 A schematic of a redox flow battery comprised of two electrolyte reservoirs, pumps, and an electrochemical cell.

RFBs can be distinguished in two group groups: 1) true RFBs, where the redox-active species are always dissolved in solution; 2) hybrid RFBs, where at least one of the redox-active

species is plated as a solid within the electrochemical cell. True RFBs achieve all the advantages, including the decoupling of energy and power, whereas hybrid RFBs do not achieve this because energy is stored in the reduction of metal ions to plate solid metal into the electrochemical cell during charging. The energy rating of the system therefore scales with the size of the electrochemical cell.

1.2.1 Vanadium redox flow batteries

The ubiquitous RFB is the all-vanadium RFB (VRFBs) which was first pioneered in the 1980s by Professor Maria Skyllas-Kazacos.[24] VRFB utilizes vanadium's many oxidation states, V^{2+}/V^{3+} in the anolyte and VO^{2+}/VO_2^+ in the catholyte. These dissolve and become redox-active electrolytes in strong acidic conditions. The half-cell reactions in a VRFB are as the following:

$$\text{Anolyte: } VO_2^+ + 2H^+ + e^- \underset{\text{charge}}{\overset{\text{discharge}}{\rightleftharpoons}} VO^{2+} + H_2O \qquad (1.1)$$

$$E_{\frac{1}{2}} = +0.80 \text{ V vs Ag/AgCl}$$

$$\text{Catholyte: } V^{2+} + e^- \underset{\text{charge}}{\overset{\text{discharge}}{\rightleftharpoons}} V^{3+} \qquad (1.2)$$

$$E_{\frac{1}{2}} = -0.47 \text{ V vs Ag/AgCl}$$

The overall electrochemical redox reaction yields a cell voltage of 1.26 V. Upon discharge, V^{2+} is oxidized to V^{3+} in the anolyte and VO_2^+ is reduced to VO^{2+} in the catholyte. The acidic electrolyte utilizes protons to diffusion across the ion-exchange membrane to maintain charge neutrality. In 2010, at the Pacific Northwest National Laboratory, a mixed sulfate-chloride electrolyte demonstrated vanadium concentrations of 2.5 M over a -20 and +50 ºC temperature window.[25, 26] The increased stability of V^{5+} electrolyte at elevated temperatures is due to the higher proton concentration shifting the equilibrium of V^{5+} away from V_2O_5, whereas the low temperature

stability is achieved by hindering the precipitation of $V^{4+/3+/2+}$ by disrupting the common ion effect of the sulfate ions.[27]

The small ionic radii of the vanadium cation redox-active species can diffuse through the ion-exchange membrane, and this cross-diffusion leads to capacity loss for that specific cycle. VRFBs are considered cross-diffusion tolerant because the redox-active species are vanadium-based in both electrolytes. Upon subsequent cycling, the capacity loss is reversed as the electrolyte is regenerated to utilize the desired redox couple chemistry. Ultimately, cross-diffusion is not preferential and could develop into more consequential issues, such as membrane fouling, whereby the vanadium ions become irreversibly trapped within the membrane and create dead-regions, resulting in higher cell resistance.[28]

VRFBs are the most mature redox chemistry within RFBs with a 25+ year operational lifespan. VRFBs have been commercialized with the largest installation in Dalian, China as a 200 MW/800 MWh system.[29] A major hurdle for VRFB installations is the high-cost of the vanadium precursor. The commercial precursors for VRFBs are $VOSO_4$ or V_2O_5, the latter is cheaper but it is significantly less soluble than the former.[30] The market value of V_2O_5 is volatile, making it challenging to plan and fund new VRFB installations. It has been reported that a VRFB system cost is estimated to be \$330/kWh for a 10 MW/40MWh,[31] which is far higher than the US Department of Energy (DOE) current target of \$100/kWh and the ambitious future target of \$0.05/kWh.[21, 32]

1.2.2 Iron-based flow batteries

Iron is the most abundant transition metal, making it a great candidate for ARFBs as it would strength a key advantage of the technology since cheap material costs result in low-cost per kWh energy storage. The first example of an iron-based RFB are iron-chromium RFBs (ICRFBs) which were extensively pursued by NASA.[33] Like iron, chromium is also a cheap, widely available

mineral, so a RFB consisting of iron and chromium will result in lower material costs compared to VRFBs. Both the elements utilize the trivalent/divalent redox couple in acidic conditions with the following half-cell reactions for ICRFBs:

$$\text{Anolyte: } Cr^{2+} \underset{\text{charge}}{\overset{\text{discharge}}{\rightleftharpoons}} Cr^{3+} + e^- \qquad (1.3)$$

$$E_{\frac{1}{2}} = -0.62 \text{ V vs Ag/AgCl}$$

$$\text{Catholyte: } Fe^{3+} + e^- \underset{\text{charge}}{\overset{\text{discharge}}{\rightleftharpoons}} Fe^{2+} \qquad (1.4)$$

$$E_{\frac{1}{2}} = +0.57 \text{ V vs Ag/AgCl}$$

The overall cell voltage is 1.18 V. Initial prototypes were prone to cation migration across the membrane, resulting in irreversible capacity fade. Eventually, a mixed electrolyte consisting of iron and chromium for both the anolyte and catholyte eliminated the irreversible capacity fade. Mixing of the two reservoirs recovered any capacity fade during long-term operation.[34] Cycling between Cr^{3+}/Cr^{2+} suffered from slow electrochemical kinetics and hydrogen evolution reaction (HER). This hydrogen evolution lowers the energy efficiency of the system and creates an imbalance in the state of charge (SOC) between the two reservoirs, resulting in capacity fade. It is common to improve sluggish kinetic performance of electrolyte with the addition of a catalyst. Bismuth is a popular electrocatalyst which improves the kinetics of Cr^{3+}/Cr^{2+} redox reaction and suppresses the HER.[35-37] ICRFBs system costs are lower than VRFBs, however, the capacity fade is greater with ICRFB employing mixed chromium/iron electrolytes and bismuth catalysts than VRFBs.[37]

The hybrid all-iron RFB was proposed in the 1980s as the lowest material cost and low toxicity option. This RFB has the following half-cell redox reactions:

$$\text{Anolyte: } Fe^{0} \underset{\text{charge}}{\overset{\text{discharge}}{\rightleftharpoons}} Fe^{2+} + 2e^{-} \quad (1.5)$$

$$E_{\frac{1}{2}} = -0.65 \text{ V vs Ag/AgCl}$$

$$\text{Catholyte: } Fe^{3+} + e^{-} \underset{\text{charge}}{\overset{\text{discharge}}{\rightleftharpoons}} Fe^{2+} \quad (1.6)$$

$$E_{\frac{1}{2}} = +0.57 \text{ V vs Ag/AgCl}$$

The overall cell voltage yielded is 1.21 V.[38] Utilizing these redox reactions, the battery demonstrated a high energy density of 76 Wh L^{-1}.[39] However, due to the nature of the anolyte redox reaction, this hybrid battery does not have all the advantages of true RFBs, whereby power and energy are not decoupled with divalent iron reducing, resulting in iron plating the cathode during charging. Ultimately, hybrid all-iron batteries development was stymied by understanding the limitations of iron by analyzing iron's Pourbaix diagram (Figure 1.3). This RFB operates in acidic conditions, however, only the ionic iron species are stable at low pH. The Fe^{2+}/Fe^{0} redox potential is below that of the HER at pH 0, making this thermodynamically favorable in these operating conditions. Furthermore, metallic iron would react with protons, dissolving the plate and creating an imbalance of charge on either side of the battery. Ferric iron is only stable highly acidic conditions, with the ferric species precipitating out at pH > 2. The redox chemistry drawbacks for both reservoirs have prevented further development for hybrid iron based RFBs.

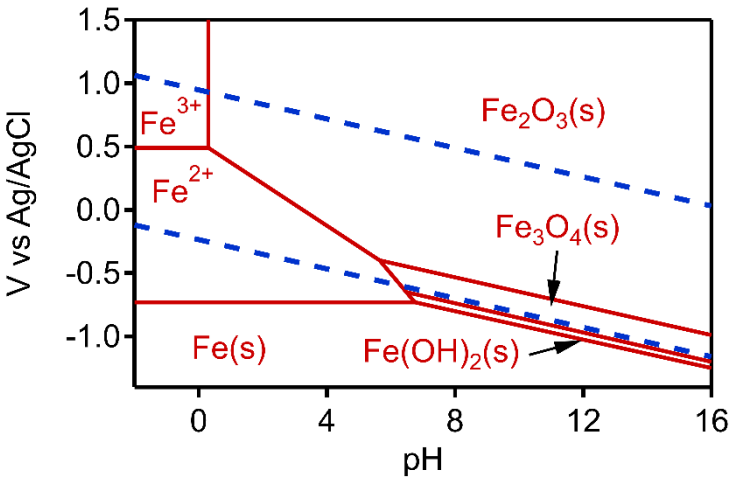

Figure 1.3 Pourbaix diagram of iron in non-complexing aqueous medium a temperature of 25ºC. The two dashed blue lines indicate the oxygen evolution reaction and the hydrogen evolution reaction.

Organic ligands have been used to manipulate the redox properties of transition metal-based electrolytes, allowing modulation of the redox potential, solubility, and redox kinetics.[40-42] Chromium when bound by ethylenediaminetetraacetic acid forms Cr-EDTA complex which modifies the solubility to neutral pH conditions, shifts the redox potential from -0.62 to -1.20 V vs Ag/AgCl, and boosts the redox kinetics by over 10^5.[43] A variant of this metal complex is Chromium 1,3-propylenediaminetetraacetic acid (Cr-PDTA) that boasts improved redox kinetics, suppresses HER, and possesses a more negative redox potential of -1.31 V vs Ag/AgCl.[44] Pairing Cr-PDTA as the anolyte with a ferrocyanide catholyte yields a cell voltage of 1.6 V, an exceptionally large cell voltage for an ARFB.

A vast number of iron complexes have been electrochemically investigated and have long been an interest to the RFB community with iron complexes spanning the full width of the voltage stability window for water. Recently, an all-soluble all-iron aqueous RFB was reported,[45] whereby different iron complexes reside in either reservoir to manipulate and maximize the cell voltage beyond prior reports of iron-based RFBs. Iron-triethanolamine (Fe-TEOA) has a redox potential of

-1.09 V vs Ag/AgCl and acts as the redox active species in the anolyte. In conjunction with ferrocyanide in the catholyte, the overall cell potential is 1.34 V, surpassing that of the hybrid all-iron RFB but with the full benefits of a true RFB with decoupled power and energy. However, Fe-TEOA stability is dependent on the free ligand concentration within the electrolyte due to the weak binding interaction of the deprotonated ligand with iron centers. Crossover of unbound TEOA to the catholyte reduces the coulombic efficiency as TEOA is oxidized by ferricyanide, resulting in a charge imbalance and eventual capacity fade.

The stability of a metal complex is determined by the association constant between the metal cation and the ligand. A prevalent complex for ARFBs is ferricyanide. One factor is the large association constant the cyanide ligand has with both ferrous and ferric iron, therefore, ferro-/ferricyanide are low toxic complexes due to its stability. The cyanide ligand donates its sigma electrons to the iron (σ-donor), while accepting electron density from the overlap of the iron t_{2g} orbital and cyanide π* orbital (π-acceptor), otherwise known as back-bonding. Ferricyanide has been widely demonstrated in catholytes from pH 7 to 14 with a redox potential of 0.27 V vs Ag/AgCl at all pH values within this range. Ferricyanide is unstable in acidic conditions, resulting in the hydrolysis of iron and the protonation of cyanide ligands, evolving toxic hydrogen cyanide gas. The solubility of potassium ferrocyanide is 0.76 M and sodium ferrocyanide is 0.56 M at pH 7, with higher solubilities for the ferricyanide salts.[46] The solubility can be improved with a Na^+/K^+ cation mixture to 1.5 M. Furthermore, the solubility can reach 1.6 M in an ammonium or calcium-based supporting electrolyte, doubling the volumetric capacity of the ferro-/ferricyanide catholyte.[47, 48] For all its popularity, the solubility in very alkaline conditions is lower than in neutral conditions, impairing its potential application in alkaline RFBs.

Ferrocene derivatives have been studied in catholytes for ARFBs. Ferrocene has a redox potential of 0.2 V vs Ag/AgCl and has been widely used as a reference electrode in organic systems. Ferrocene is particularly appealing because the redox potential and water solubility can

be tuned by organic modification of the cyclopentadiene (Cp) rings, a significant advantage over ferricyanide. In non-aqueous systems, the addition of electron-donating groups has been shown to shift the redox potential to more negative potentials.[49] The number of electron-donating groups added to the Cp rings influences the electron density on the iron center, improving the resistance to oxidation. Ferrocene derivatives for ARFBs have included ferrocene functionalized by alkyl-sulfates and alkyl-ammonium groups with redox potentials of 0.16 and 0.41 V vs Ag/AgCl, respectively.[50, 51] The alkyl-ammonium functionalized ferrocene boasts high solubilities of up to 4 M in deionized water and 3 M in 2 M sodium chloride solution. The ammonium functional group is electron withdrawing, which destabilizes the bonding of the Cp rings with the iron center. The alkyl-sulfate functionalized ferrocene (Fc-SO_3Na) is robust in electrochemical cycling because of its electron-donating functional groups. However, ferrocenium can react and decompose in the presence of oxygen, therefore, it is important to exclude oxygen from the system when cycling ferrocene.[50] Ferrocenium is also prone to nucleophilic attack from weak ligands, such as Cl^- and H_2O. A ligand exchange couples with the reduction of ferrocene, resulting in irreversible redox reactions and Cp radical transformations.[32] This is the main decomposition pathway of ferrocene-based RFBs leading to capacity fade.

1.2.3 Zinc-based flow batteries

Zinc is an appealing element for use in anolytes and has been thoroughly investigated in aqueous Zn-ion, and Zn-based hybrid flow batteries.[52] Zinc batteries can boast some of the lowest material costs due to the abundance of zinc, high volumetric capacity with its two electron redox reaction and high solubility, and low redox potential. Although a low redox potential is ideal for achieving a high cell voltage, Zn-based batteries operating in acidic conditions are susceptible to the HER, which impacts the coulombic efficiency and contributes to capacity fade, without thoughtful material design in choosing inert substrates for the zinc electrodeposition and

suppressing the HER with a suitable electrolyte. Another issue is the divalent zinc species between pH 8 and 10 is insoluble, requiring complex fluid dynamics to operate in flow batteries. In more alkaline conditions, especially beyond pH 13, zincate is fully soluble and has a redox potential of -1.4 V vs Ag/AgCl.

Zinc-bromide RFB is a notable Zn-based system with an electrolyte cost 16-fold less than VRFBs at $5/kWh.[53] These systems have a high cell voltage (~1.8 V) and a high theoretical energy density (440 Wh kg^{-1}).[53] Typically, commercial systems lag far behind the theoretical energy density and achieve 60 – 85 Wh kg^{-1}, just 20% of the theoretical threshold.[54] The redox reaction in the catholyte is the interconversion between bromine and bromide. Bromine has poor solubility in aqueous systems, therefore, a sequestering agent is present in the catholyte that stores the bromine within an oily phase.[55] The addition of these agents that introduce sequestering/dissociation steps does kinetically impact the redox chemistry of the catholyte, yielding more sluggish redox properties. Furthermore, zinc dendrite formation is another drawback for Zn-based RFBs. Dendrite formation results in low coulombic efficiency and, with cycling, will eventually penetrate the membrane and short-circuit the system. Dendrite formation has been minimized by understanding the mechanism behind its growth. Dendrite minimization strategies include: 1) employing low/moderate overpotentials to mitigate the Zn chemical potential gradient which causes needle-like dendrites, 2) adding supporting electrolyte or surface-active agents to hinder Zn crystal formation, 3) electrode engineering, where electrodeposition occurs, with a carbon nanotube array provides a homogeneous electric field that suppresses dendrite formation.[56]

1.2.4 Sulfur-based flow batteries

Sulfur is one of the most abundant elements globally and is produced on a ton-scale as a by-product from the oil and gas refining industry, therefore, the material costs are incredibly low. Coupled with the high-water solubility and stability of polysulfides, there is immense interest for RFB applications.[57, 58] The redox potential of sulfide/polysulfide is -0.65 V vs Ag/AgCl making it a candidate for aqueous anolytes. A major drawback of sulfur-based anolytes is the sluggish kinetics which alone is not practical for RFB. It has been shown that kinetics can be improved by impregnating the carbon cloth electrode with Cu_2S nanoparticles, acting as an electrocatalyst for the S^{2-}/S_2^{2-} redox reaction.[59] There is no discussion to whether this system is durable in the long-term. Another issue is to potential to generate toxic hydrogen sulfide gas, which is achieved at pH levels < 10.

1.2.5 Aqueous Organic Redox Flow Batteries (AORFBs)

A tremendous amount of research is currently being done on investigating redox-active organic molecules for RFB applications. Many different classes of redox-active organics have been studies for AORFBs, including quinone,[60-66] viologen,[67-70] phenazine,[35, 71-73] alloxazine,[35, 74] and (2,2,6,6-tetramethylpiperidin-1-yl)oxyl (TEMPOs)[68, 69, 75] derivatives. These molecules have great potential for AORFBs because of their low cost, earth-abundant materials, and can be modified via organic synthetic routes. By functionalizing redox-active organics, the electrochemical properties are altered, such as the redox potential, molecular net charge, and water solubility. Furthermore, redox-active organics are sterically large, drastically reducing their propensity for crossover. Many redox-active molecules demonstrate fast electrochemical kinetics and good stability with minimal capacity fade for thousands of cycles.

Although there are examples of redox-active molecules demonstrating good electrochemical reversibility, fast redox kinetics, and high tunability of redox properties, the main

challenge for AORFBs is achieving long-term cycling stability. It has been commonly observed that these molecules under cycling conditions have a tendency for side reactions, reducing the effective concentration of the redox-active molecules, resulting in capacity fade. Similar to capacity fade in inorganic RFBs, there are mitigation strategies or regeneration processes to counter this capacity fade with intermittent maintenance cycling.[76-78]

1.2.6 Aqueous Redox-Targeting Redox Flow Batteries (aqueous RT-RFBs)

In 2006, Wang *et al.*[79] proposed the mechanism of utilizing insulating solid intercalation host materials within an electrochemical cell, whereby the solid additive is indirectly charge-discharged via a redox mediator that either possesses a similar Fermi energy to the solid additive, or a pair of redox mediators are employed to straddle the Fermi energy of the solid – a thermodynamically large driving force to reversibly charge-discharge the solid. The advantage of this redox-targeting mechanism is the solid can act as a charge reservoir and undergo interfacial charge-transfer with the redox mediator(s) without the need of conductive additives, which are commonly used when directly charging these insulating solid battery materials directly on the electrode. This boosts the atomic efficiency of an electrochemical cell involved in redox reactions, enabling the design of high energy density batteries.

Redox targeting has gained a lot of traction within the RFB field and is a solution to overcome the inherent low energy density of many RFB systems, due to solubility limit of redox-active species. Slurry flow batteries show remarkable energy densities with high solid material loadings; however, the high viscosity and the engineering difficulties of proper electrolyte-solid mixing continuously hampers practical operation.[80] Redox targeting-based flow systems (Figure 1.4) have the solid additive immobilized in the reservoir tank with only the redox mediator flowing between the reservoir tank and the electrochemical stack. This configuration possesses good

fluidity, negating the need to engineer a long-term complex fluid dynamic solution. RT-RFBs integrate the advantages of RFBs and solid-state batteries.

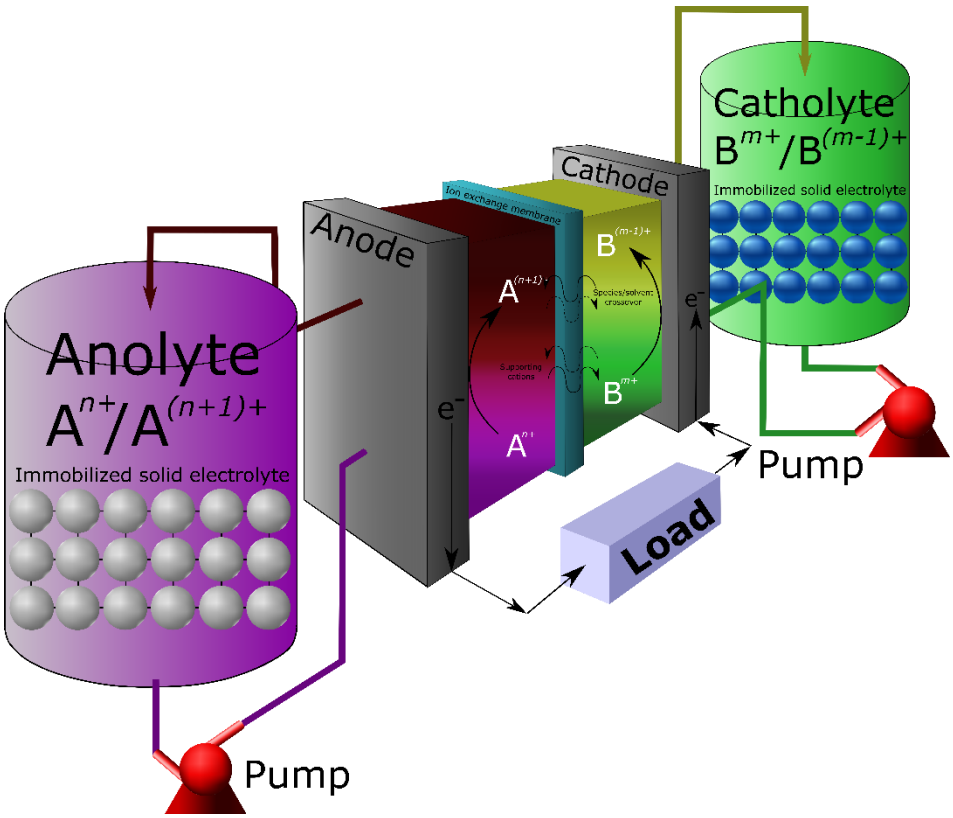

Figure 1.4 A schematic of a redox-targeting redox flow battery highlighting the redox reactions within the electrochemical stack and within the electrolyte reservoir tanks.

A class of materials that has gained significant interest are Prussian blue and Prussian blue analogues (PBAs). Prussian blue has been around since the 18th century and is the first modern synthetic pigment.[81] PBAs consist of metal ion centers coordinated by six cyanide linkers, whereby neighboring metal centers cyanide coordination sphere alternates as either carbon-bound or nitrogen-bound. Therefore, the lattice is cubic with channels throughout, resulting in this simple metal-organic framework to be an excellent ionic conductor. In 2019, Chen *et al.*[82] demonstrated a ferricyanide-based electrolyte with a Prussian blue redox targeting reservoir as a RFB catholyte. In this report, the Prussian blue was immobilized in the catholyte

reservoir as pellets composed of 85 *wt.*% Prussian blue with carbon black conductive additive and polyvinylidene fluoride (PVDF) binder constituting the remaining 15 *wt.*%. Redox targeting was achieved with potassium ferricyanide as the redox mediator and they demonstrated the ferricyanide electrolyte alone has a volumetric density of 21.4 Ah L^{-1}, however, with Prussian blue the volumetric capacity increases to 61.9 Ah L^{-1}, breaking the solubility limit of potassium ferricyanide.

Ultimately, demonstrating exceptional volumetric capacities for both the catholyte and the anolyte are vital for aqueous RT-RFBs to supersede conventional RFBs. The vast majority of articles focus on the redox-targeting chemistry within the catholyte, typically demonstrating capacities increasing up to 4-fold.[83-86] In contrast, few examples of redox-targeting in aqueous anolytes are currently present. The lack of development for the anolyte hinders scaling up the technology because the anolyte capacity is currently multiples lower than the catholyte, resulting in the anolyte dictating the maximum capacity. In this current scenario, scaling the technology would require the anolyte to be volumetrically larger than the catholyte to compensate for the lower energy density. In an ideal case, the capacities of both reservoirs are equal, therefore, scaling both reservoirs would be the determining factor of the stored energy of the system rather than one specific reservoir.

1.2.7 ARFB performance metrics

Battery performance is evaluated on cycling stability, energy and power density, energy efficiency, and system costs normalized per unit energy (MWh). Cycling stability of ARFB is commonly evaluated as the average decay per cycle, however, this is not representative of long-term cycling effects. Many literature reports employ systems with small electrolyte volumes, each individual cycle lasting only minutes, not hours as required of the technology to be

implemented as a grid-scale ESS. A more rigorous approach would factor in the time of cycling – time is a superior factor that highlights long-term decay reaction pathways or crossover effects.[87]

The theoretical capacity, C_{ap}, is the maximum amount of charge that the battery can store, typically represented in Ah, as described by equation 1.7:

$$C_{ap} = \frac{n \times F}{3600} = \frac{C \times V \times F}{3600} \tag{1.7}$$

Where n is the number of electrons involved in the redox event, C is the concentration of the redox-active species of the capacity-limiting electrolyte with units of mol L^{-1}, V is the volume of the capacity-limiting electrolyte with units of L, and F is Faraday's constant which is 96,485 C mol^{-1}. The volumetric capacity of a system can be calculated by multiplying the measured capacity by a factor that scales the electrolyte volume to one liter.

The theoretical energy density, E_d, evaluates the energy that can be stored per unit volume, typically represented in Wh L^{-1}, as described by equation 1.8:

$$E_d = \frac{U \times C_{ap}}{V} \tag{1.8}$$

The cell voltage, U, is the difference in redox potentials of the two reservoirs with units of volts, V. The cell current, I, is the current supplied within an hour during cycling with units of Ah. The product of these two terms over the volume of the reservoir yields the energy density. For calculating the achieved energy density, the measured capacity would be substituted in for the theoretical capacity.

The power density, P, is the power per unit area of the active surface area of the electrodes, typically represented in W cm^{-2}, as described by equation 1.9:

$$P = \frac{U_d \times I_d}{A} \tag{1.9}$$

Where U_d is the discharge voltage, I_d is the discharge current, and A is the active surface area of the electrodes. Unlike volumetric capacity and energy density, the battery voltage and power density are influenced by the electrolyte conductivity, membrane resistance, electrolyte redox kinetics, and operating conditions, such as temperature, flow rate and flow fields. The overpotential is a contribution of three elements: 1) the ohmic overpotential, η_{ohm}, 2) activation overpotential, η_a, and 3) concentration overpotential, η_c. The ohmic overpotential is determined by ohm's law and is described by equation 1.10:

$$\eta_{ohm} = R_{cell}.I \tag{1.10}$$

The cell resistance, R_{cell}, embodies the electrolyte resistance, membrane resistance, and all electronic contact resistance, such as between the current collector plates and electrodes or any electrical cables and connections. The membrane resistance is a major contributing factor to cell resistance, making it is an area of high research activity. As a matter of fact, developing a membrane with high ionic conductivity raises the power density.[88-91] The activation overpotential, η_a, is the resistance due to the electrochemical charge-discharging kinetics of the electrolyte at the electrodes. The greater the kinetic rate constants of the redox-active molecules, the lower the activation overpotential. Concentration overpotential, η_c, is from the concentration gradient of the charged/discharged electrolyte in the reservoir versus at the electrode surface. This can be mitigated by current density employed and the electrolyte flow rate. Operating with a lower current density will decrease the concentration gradient between the electrochemical stack and the reservoir tank. Furthermore, pumping at sufficiently fast flow rates will alleviate mass transport issues. Operating a system with kinetically fast redox-active molecules and a low-resistance membrane will decrease the cell overpotential, and thus, improve the power density.

For RT-RFBs, the theoretical specific capacity, C_s, is the maximum amount of charge that the redox-active solid can store, typically represented in mAh g^{-1}, as described by equation 1.11:

$$C_s = \frac{n \times F}{3.6 \times M} \quad (1.11)$$

Where n is the number of electrons involved in the redox event, F is Faraday's constant which is 96,485 C mol^{-1}, and M is the molar mass of the redox-active solid with units of g mol^{-1}.

For RT-RFBs, the efficiency of the redox-targeting reaction, η_{RT}, is the volume of the solid accessed during cycling, as described by equation 1.12:

$$\eta_{RT} = \frac{C_{RT} - C_{Ele}}{C_s} \quad (1.12)$$

Where C_{RT} is the discharge capacity achieved with the redox-active solid, C_{Ele} is the discharge capacity achieved for the liquid electrolyte alone, and C_s is the theoretical specific capacity of the redox-active solid.

ARFB performance metrics also include coulombic efficiency and energy efficiency. Coulombic efficiency, also known as Faradaic efficiency, is the ratio of number of electrons collected from the discharge cycle versus the number of electrons injected from the charge cycle – this represents the reversibility of a system. Irreversible side-reactions, such as HER and OER, and redox-active molecule crossover will result in poor coulombic efficiency (< 95%). The voltage efficiency is the ratio of the average discharge voltage versus the average charge voltage. This is predominantly due to cell resistance, which can be mitigated by the solutions previously discussed. The electrochemical kinetics of the redox-active molecules can also contribute, so it is advantageous to employ molecules with fast redox kinetics. The round-trip energy efficiency is the ratio of output energy during a discharge cycle versus the input energy during a charge cycle. This can be calculated by the product of the coulombic and voltage efficiencies. A high energy efficiency is crucial for AORFB adoption with VRFB and PHES achieving ~80%.

1.3 References

(1) Severinghaus, J. P.; Brook, E. J. Abrupt Climate Change at the End of the Last Glacial Period Inferred from Trapped Air in Polar Ice. *Science* **1999**, *286* (5441), 930-934. DOI: doi:10.1126/science.286.5441.930.

(2) Lofverstrom, M.; Thompson, D. M.; Otto-Bliesner, B. L.; Brady, E. C. The importance of Canadian Arctic Archipelago gateways for glacial expansion in Scandinavia. *Nature Geoscience* **2022**, *15* (6), 482-488. DOI: 10.1038/s41561-022-00956-9.

(3) Ramaswamy, V.; Schwarzkopf, M. D.; Randel, W. J.; Santer, B. D.; Soden, B. J.; Stenchikov, G. L. Anthropogenic and Natural Influences in the Evolution of Lower Stratospheric Cooling. *Science* **2006**, *311* (5764), 1138-1141. DOI: doi:10.1126/science.1122587.

(4) Cheng, W.; Dan, L.; Deng, X.; Feng, J.; Wang, Y.; Peng, J.; Tian, J.; Qi, W.; Liu, Z.; Zheng, X.; et al. Global monthly gridded atmospheric carbon dioxide concentrations under the historical and future scenarios. *Scientific Data* **2022**, *9* (1), 83. DOI: 10.1038/s41597-022-01196-7.

(5) Bodansky, D. The Paris Climate Change Agreement: A New Hope? *American Journal of International Law* **2016**, *110* (2), 288-319. DOI: 10.5305/amerjintelaw.110.2.0288 From Cambridge University Press Cambridge Core.

(6) Ray, S.; Gorski, A.; Cassar, C.; Yildiz, O. Electric Power Monthly May 2024. *U.S. Energy Information Administration* **2024**.

(7) Barnhart, C. J.; Dale, M.; Brandt, A. R.; Benson, S. M. The energetic implications of curtailing versus storing solar- and wind-generated electricity. *Energy & Environmental Science* **2013**, *6* (10), 2804-2810, 10.1039/C3EE41973H. DOI: 10.1039/C3EE41973H.

(8) Dunn, B.; Kamath, H.; Tarascon, J.-M. Electrical Energy Storage for the Grid: A Battery of Choices. *Science* **2011**, *334* (6058), 928-935. DOI: doi:10.1126/science.1212741.

(9) Yang, Z.; Zhang, J.; Kintner-Meyer, M. C. W.; Lu, X.; Choi, D.; Lemmon, J. P.; Liu, J. Electrochemical Energy Storage for Green Grid. *Chemical Reviews* **2011**, *111* (5), 3577-3613. DOI: 10.1021/cr100290v.

(10) Uria-Martinez, R.; Johnson, M. M. U.S. Hydropower Market Report. *Department of Energy* **2023**.

(11) Ma, T.; Yang, H.; Lu, L. Feasibility study and economic analysis of pumped hydro storage and battery storage for a renewable energy powered island. *Energy Conversion and Management* **2014**, *79*, 387-397. DOI: https://doi.org/10.1016/j.enconman.2013.12.047.

(12) McCartney, M. Living with dams: managing the environmental impacts. *Water Policy* **2009**, *11* (S1), 121-139. DOI: 10.2166/wp.2009.108 (acccessed 7/7/2024).

(13) Schmutz, S.; Moog, O. Dams: ecological impacts and management. *Riverine ecosystem management: Science for governing towards a sustainable future* **2018**, 111-127.

(14) Blakers, A.; Stocks, M.; Lu, B.; Cheng, C. A review of pumped hydro energy storage. *Progress in Energy* **2021**, *3* (2), 022003. DOI: 10.1088/2516-1083/abeb5b.

(15) Winter, M.; Barnett, B.; Xu, K. Before Li Ion Batteries. *Chemical Reviews* **2018**, *118* (23), 11433-11456. DOI: 10.1021/acs.chemrev.8b00422.

(16) Auborn, J. J.; Barberio, Y. L. Lithium Intercalation Cells Without Metallic Lithium: and. *Journal of The Electrochemical Society* **1987**, *134* (3), 638. DOI: 10.1149/1.2100521.

(17) Mizushima, K.; Jones, P. C.; Wiseman, P. J.; Goodenough, J. B. LixCoO2 (0<x<-1): A new cathode material for batteries of high energy density. *Materials Research Bulletin* **1980**, *15* (6), 783-789. DOI: https://doi.org/10.1016/0025-5408(80)90012-4.

(18) Mizushima, K.; Jones, P. C.; Wiseman, P. J.; Goodenough, J. B. LixCoO2 (0<x⩽1): A new cathode material for batteries of high energy density. *Solid State Ionics* **1981**, *3-4*, 171-174. DOI: https://doi.org/10.1016/0167-2738(81)90077-1.

(19) Lewis, M. *The world's largest battery storage system just got even larger*. Electrek, 2023. https://electrek.co/2023/08/03/worlds-largest-battery-storage-system-just-got-even-larger/ (accessed.

(20) IRENA. Electricity Storage and Renewables: Cost and Markets to 2030. *International Renewable Energy Agency, Abu Dhabi* **2017**.

(21) Fitzsimmons, A.; Pesin, M.; Hsieh, E.; Lightner, V.; Harsha, M. G.; Moreno, A.; Vetrano, J. Energy Storage Grand Challenge Roadmap. *U.S. Department of Energy* **2020**.

(22) Ashimura, S.; Miyake, Y. Denki Kagaku. *Journal of Power Sources* **1971**, *39* (977).

(23) Larcher, D.; Tarascon, J. M. Towards greener and more sustainable batteries for electrical energy storage. *Nature Chemistry* **2015**, *7* (1), 19-29. DOI: 10.1038/nchem.2085.

(24) Rychcik, M.; Skyllas-Kazacos, M. Characteristics of a new all-vanadium redox flow battery. *Journal of Power Sources* **1988**, *22* (1), 59-67. DOI: https://doi.org/10.1016/0378-7753(88)80005-3.

(25) Li, L.; Kim, S.; Wang, W.; Vijayakumar, M.; Nie, Z.; Chen, B.; Zhang, J.; Xia, G.; Hu, J.; Graff, G.; et al. A Stable Vanadium Redox-Flow Battery with High Energy Density for Large-Scale Energy Storage. *Advanced Energy Materials* **2011**, *1* (3), 394-400. DOI: https://doi.org/10.1002/aenm.201100008.

(26) Yang, Y.; Zhang, Y.; Tang, L.; Liu, T.; Huang, J.; Peng, S.; Yang, X. Investigations on physicochemical properties and electrochemical performance of sulfate-chloride mixed acid electrolyte for vanadium redox flow battery. *Journal of Power Sources* **2019**, *434*, 226719. DOI: https://doi.org/10.1016/j.jpowsour.2019.226719.

(27) Choi, C.; Kim, S.; Kim, R.; Choi, Y.; Kim, S.; Jung, H.-y.; Yang, J. H.; Kim, H.-T. A review of vanadium electrolytes for vanadium redox flow batteries. *Renewable and Sustainable Energy Reviews* **2017**, *69*, 263-274. DOI: https://doi.org/10.1016/j.rser.2016.11.188.

(28) Vijayakumar, M.; Bhuvaneswari, M. S.; Nachimuthu, P.; Schwenzer, B.; Kim, S.; Yang, Z.; Liu, J.; Graff, G. L.; Thevuthasan, S.; Hu, J. Spectroscopic investigations of the fouling process

on Nafion membranes in vanadium redox flow batteries. *Journal of Membrane Science* **2011**, *366* (1), 325-334. DOI: https://doi.org/10.1016/j.memsci.2010.10.018.

(29) Phiddian, E. World's biggest flow battery opens in China. **2022**.

(30) El Hage, R.; Chauvet, F.; Biscans, B.; Cassayre, L.; Maurice, L.; Tzedakis, T. Kinetic study of the dissolution of vanadyl sulfate and vanadium pentoxide in sulfuric acid aqueous solution. *Chemical Engineering Science* **2019**, *199*, 123-136. DOI: 10.1016/j.ces.2019.01.024.

(31) Mongird, K.; Viswanathan, V. V.; Alam, J.; Vartanian, C.; Sprenkle, V. 2020 Grid Energy Storage Technology Cost and Performance Assessment. **2020**.

(32) Luo, J.; Hu, B.; Hu, M.; Zhao, Y.; Liu, T. L. Status and Prospects of Organic Redox Flow Batteries toward Sustainable Energy Storage. *ACS Energy Letters* **2019**, *4* (9), 2220-2240. DOI: 10.1021/acsenergylett.9b01332.

(33) Hagedorn, N. H. NASA Redox Storage System Development Project. Final report. **1984**. DOI: 10.2172/6472995.

(34) Gahn, R. F.; Hagedorn, N. H.; Johnson, J. A. Cycling performance of the ironchromium redox energy storage system. National Aeronautics and Space Administration. **1985**.

(35) Ahn, Y.; Moon, J.; Park, S. E.; Shin, J.; Wook Choi, J.; Kim, K. J. High-performance bifunctional electrocatalyst for iron-chromium redox flow batteries. *Chemical Engineering Journal* **2021**, *421*, 127855. DOI: https://doi.org/10.1016/j.cej.2020.127855.

(36) Sun, C.; Zhang, H. Review of the Development of First-Generation Redox Flow Batteries: Iron-Chromium System. *ChemSusChem* **2022**, *15* (1), e202101798. DOI: https://doi.org/10.1002/cssc.202101798.

(37) Zeng, Y. K.; Zhao, T. S.; An, L.; Zhou, X. L.; Wei, L. A comparative study of all-vanadium and iron-chromium redox flow batteries for large-scale energy storage. *Journal of Power Sources* **2015**, *300*, 438-443. DOI: https://doi.org/10.1016/j.jpowsour.2015.09.100.

(38) Tucker, M. C.; Phillips, A.; Weber, A. Z. All-Iron Redox Flow Battery Tailored for Off-Grid Portable Applications. *ChemSusChem* **2015**, *8* (23), 3996-4004. DOI: https://doi.org/10.1002/cssc.201500845.

(39) Hruska, L. W.; Savinell, R. F. Investigation of Factors Affecting Performance of the Iron-Redox Battery. *Journal of The Electrochemical Society* **1981**, *128* (1), 18. DOI: 10.1149/1.2127366.

(40) Gordon, Z.; Drummond, M. J.; Bogart, J. A.; Schelter, E. J.; Lord, R. L.; Fout, A. R. Tuning the Fe(II/III) Redox Potential in Nonheme Fe(II)–Hydroxo Complexes through Primary and Secondary Coordination Sphere Modifications. *Inorganic Chemistry* **2017**, *56* (9), 4852-4863. DOI: 10.1021/acs.inorgchem.6b03071.

(41) Ruan, W.; Mao, J.; Yang, S.; Shi, C.; Jia, G.; Chen, Q. Designing Cr complexes for a neutral Fe–Cr redox flow battery. *Chemical Communications* **2020**, *56* (21), 3171-3174, 10.1039/C9CC09704J. DOI: 10.1039/C9CC09704J.

(42) Yamaguchi, K. S.; Sawyer, D. T. The Redox Chemistry of Manganese(III) and -(IV) Complexes. *Israel Journal of Chemistry* **1985**, *25* (2), 164-176. DOI: https://doi.org/10.1002/ijch.198500026.

(43) Ogino, H.; Nagata, T.; Ogino, K. Redox potentials and related thermodynamic parameters of (diaminopolycarboxylato)metal(III/II) redox couples. *Inorganic Chemistry* **1989**, *28* (19), 3656-3659. DOI: 10.1021/ic00318a009.

(44) Waters, S. E.; Robb, B. H.; Marshak, M. P. Effect of Chelation on Iron–Chromium Redox Flow Batteries. *ACS Energy Letters* **2020**, *5* (6), 1758-1762. DOI: 10.1021/acsenergylett.0c00761.

(45) Gong, K.; Xu, F.; Grunewald, J. B.; Ma, X.; Zhao, Y.; Gu, S.; Yan, Y. All-Soluble All-Iron Aqueous Redox-Flow Battery. *ACS Energy Letters* **2016**, *1* (1), 89-93. DOI: 10.1021/acsenergylett.6b00049.

(46) Luo, J.; Hu, B.; Debruler, C.; Bi, Y.; Zhao, Y.; Yuan, B.; Hu, M.; Wu, W.; Liu, T. L. Unprecedented Capacity and Stability of Ammonium Ferrocyanide Catholyte in pH Neutral

Aqueous Redox Flow Batteries. *Joule* **2019**, *3* (1), 149-163. DOI: https://doi.org/10.1016/j.joule.2018.10.010.

(47) Reber, D.; Thurston, J. R.; Becker, M.; Marshak, M. P. Stability of highly soluble ferrocyanides at neutral pH for energy-dense flow batteries. *Cell Reports Physical Science* **2023**, *4* (1), 101215. DOI: https://doi.org/10.1016/j.xcrp.2022.101215.

(48) Wang, G.; Zou, H.; Xu, Z.; Tang, A.; Zhong, F.; Zhu, X.; Qin, C.; Ding, M.; You, W.; Jia, C. Unlocking the solubility limit of ferrocyanide for high energy density redox flow batteries. *Materials Today Energy* **2022**, *28*, 101061. DOI: https://doi.org/10.1016/j.mtener.2022.101061.

(49) Paul, A.; Borrelli, R.; Bouyanfif, H.; Gottis, S.; Sauvage, F. Tunable Redox Potential, Optical Properties, and Enhanced Stability of Modified Ferrocene-Based Complexes. *ACS Omega* **2019**, *4* (12), 14780-14789. DOI: 10.1021/acsomega.9b01341.

(50) Beh, E. S.; De Porcellinis, D.; Gracia, R. L.; Xia, K. T.; Gordon, R. G.; Aziz, M. J. A Neutral pH Aqueous Organic–Organometallic Redox Flow Battery with Extremely High Capacity Retention. *ACS Energy Letters* **2017**, *2* (3), 639-644. DOI: 10.1021/acsenergylett.7b00019.

(51) Yu, J.; Salla, M.; Zhang, H.; Ji, Y.; Zhang, F.; Zhou, M.; Wang, Q. A robust anionic sulfonated ferrocene derivative for pH-neutral aqueous flow battery. *Energy Storage Materials* **2020**, *29*, 216-222. DOI: https://doi.org/10.1016/j.ensm.2020.04.020.

(52) Yuan, Z.; Yin, Y.; Xie, C.; Zhang, H.; Yao, Y.; Li, X. Advanced Materials for Zinc-Based Flow Battery: Development and Challenge. *Advanced Materials* **2019**, *31* (50), 1902025. DOI: https://doi.org/10.1002/adma.201902025.

(53) Khor, A.; Leung, P.; Mohamed, M. R.; Flox, C.; Xu, Q.; An, L.; Wills, R. G. A.; Morante, J. R.; Shah, A. A. Review of zinc-based hybrid flow batteries: From fundamentals to applications. *Materials Today Energy* **2018**, *8*, 80-108. DOI: https://doi.org/10.1016/j.mtener.2017.12.012.

(54) Rajarathnam, G. P. The Zinc/Bromine Flow Battery: Fundamentals and Novel Materials for Technology Advancement. 2016. http://hdl.handle.net/2123/16394.

(55) Cathro, K. J.; Hoobin, P. M.; Constable, D. C. Zinc-Bromide Batteries for Energy Storage Applications. *Department of Resource and Energy* **1987**.

(56) Parker, J. F.; Chervin, C. N.; Nelson, E. S.; Rolison, D. R.; Long, J. W. Wiring zinc in three dimensions re-writes battery performance—dendrite-free cycling. *Energy & Environmental Science* **2014**, *7* (3), 1117-1124, 10.1039/C3EE43754J. DOI: 10.1039/C3EE43754J.

(57) Liu, J.; Zhou, W.; Zhao, R.; Yang, Z.; Li, W.; Chao, D.; Qiao, S.-Z.; Zhao, D. Sulfur-Based Aqueous Batteries: Electrochemistry and Strategies. *Journal of the American Chemical Society* **2021**, *143* (38), 15475-15489. DOI: 10.1021/jacs.1c06923.

(58) Zhang, S.; Guo, W.; Yang, F.; Zheng, P.; Qiao, R.; Li, Z. Recent Progress in Polysulfide Redox-Flow Batteries. *Batteries & Supercaps* **2019**, *2* (7), 627-637. DOI: https://doi.org/10.1002/batt.201900056.

(59) Yu, J.; Fan, L.; Yan, R.; Zhou, M.; Wang, Q. Redox Targeting-Based Aqueous Redox Flow Lithium Battery. *ACS Energy Letters* **2018**, *3* (10), 2314-2320. DOI: 10.1021/acsenergylett.8b01420.

(60) Yang, Z.; Tong, L.; Tabor, D. P.; Beh, E. S.; Goulet, M.-A.; De Porcellinis, D.; Aspuru-Guzik, A.; Gordon, R. G.; Aziz, M. J. Alkaline Benzoquinone Aqueous Flow Battery for Large-Scale Storage of Electrical Energy. *Advanced Energy Materials* **2018**, *8* (8), 1702056. DOI: https://doi.org/10.1002/aenm.201702056.

(61) Wedege, K.; Dražević, E.; Konya, D.; Bentien, A. Organic Redox Species in Aqueous Flow Batteries: Redox Potentials, Chemical Stability and Solubility. *Scientific Reports* **2016**, *6* (1), 39101. DOI: 10.1038/srep39101.

(62) Hasan, F.; Mahanta, V.; Abdelazeez, A. A. A. Quinones for Aqueous Organic Redox Flow Battery: A Prospective on Redox Potential, Solubility, and Stability. *Advanced Materials Interfaces* **2023**, *10* (24), 2300268. DOI: https://doi.org/10.1002/admi.202300268.

(63) Lin, K.; Chen, Q.; Gerhardt, M. R.; Tong, L.; Kim, S. B.; Eisenach, L.; Valle, A. W.; Hardee, D.; Gordon, R. G.; Aziz, M. J.; et al. Alkaline quinone flow battery. *Science* **2015**, *349* (6255), 1529-1532. DOI: doi:10.1126/science.aab3033.

(64) Park, M.; Beh, E. S.; Fell, E. M.; Jing, Y.; Kerr, E. F.; De Porcellinis, D.; Goulet, M.-A.; Ryu, J.; Wong, A. A.; Gordon, R. G.; et al. A High Voltage Aqueous Zinc–Organic Hybrid Flow Battery. *Advanced Energy Materials* **2019**, *9* (25), 1900694. DOI: https://doi.org/10.1002/aenm.201900694.

(65) Cao, J.; Tao, M.; Chen, H.; Xu, J.; Chen, Z. A highly reversible anthraquinone-based anolyte for alkaline aqueous redox flow batteries. *Journal of Power Sources* **2018**, *386*, 40-46. DOI: https://doi.org/10.1016/j.jpowsour.2018.03.041.

(66) Hu, B.; Luo, J.; Hu, M.; Yuan, B.; Liu, T. L. A pH-Neutral, Metal-Free Aqueous Organic Redox Flow Battery Employing an Ammonium Anthraquinone Anolyte. *Angewandte Chemie International Edition* **2019**, *58* (46), 16629-16636. DOI: https://doi.org/10.1002/anie.201907934.

(67) Hu, B.; DeBruler, C.; Rhodes, Z.; Liu, T. L. Long-Cycling Aqueous Organic Redox Flow Battery (AORFB) toward Sustainable and Safe Energy Storage. *Journal of the American Chemical Society* **2017**, *139* (3), 1207-1214. DOI: 10.1021/jacs.6b10984.

(68) Janoschka, T.; Morgenstern, S.; Hiller, H.; Friebe, C.; Wolkersdörfer, K.; Häupler, B.; Hager, M. D.; Schubert, U. S. Synthesis and characterization of TEMPO- and viologen-polymers for water-based redox-flow batteries. *Polymer Chemistry* **2015**, *6* (45), 7801-7811, 10.1039/C5PY01602A. DOI: 10.1039/C5PY01602A.

(69) Liu, T.; Wei, X.; Nie, Z.; Sprenkle, V.; Wang, W. A Total Organic Aqueous Redox Flow Battery Employing a Low Cost and Sustainable Methyl Viologen Anolyte and 4-HO-TEMPO Catholyte. *Advanced Energy Materials* **2016**, *6* (3), 1501449. DOI: https://doi.org/10.1002/aenm.201501449.

(70) Luo, J.; Hu, B.; Debruler, C.; Liu, T. L. A π-Conjugation Extended Viologen as a Two-Electron Storage Anolyte for Total Organic Aqueous Redox Flow Batteries. *Angewandte Chemie International Edition* **2018**, *57* (1), 231-235. DOI: https://doi.org/10.1002/anie.201710517.

(71) Hollas, A.; Wei, X.; Murugesan, V.; Nie, Z.; Li, B.; Reed, D.; Liu, J.; Sprenkle, V.; Wang, W. A biomimetic high-capacity phenazine-based anolyte for aqueous organic redox flow batteries. *Nature Energy* **2018**, *3* (6), 508-514. DOI: 10.1038/s41560-018-0167-3.

(72) Wang, C.; Li, X.; Yu, B.; Wang, Y.; Yang, Z.; Wang, H.; Lin, H.; Ma, J.; Li, G.; Jin, Z. Molecular Design of Fused-Ring Phenazine Derivatives for Long-Cycling Alkaline Redox Flow Batteries. *ACS Energy Letters* **2020**, *5* (2), 411-417. DOI: 10.1021/acsenergylett.9b02676.

(73) Winsberg, J.; Stolze, C.; Muench, S.; Liedl, F.; Hager, M. D.; Schubert, U. S. TEMPO/Phenazine Combi-Molecule: A Redox-Active Material for Symmetric Aqueous Redox-Flow Batteries. *ACS Energy Letters* **2016**, *1* (5), 976-980. DOI: 10.1021/acsenergylett.6b00413.

(74) Lin, K.; Gómez-Bombarelli, R.; Beh, E. S.; Tong, L.; Chen, Q.; Valle, A.; Aspuru-Guzik, A.; Aziz, M. J.; Gordon, R. G. A redox-flow battery with an alloxazine-based organic electrolyte. *Nature Energy* **2016**, *1* (9), 16102. DOI: 10.1038/nenergy.2016.102.

(75) Liu, Y.; Goulet, M.-A.; Tong, L.; Liu, Y.; Ji, Y.; Wu, L.; Gordon, R. G.; Aziz, M. J.; Yang, Z.; Xu, T. A Long-Lifetime All-Organic Aqueous Flow Battery Utilizing TMAP-TEMPO Radical. *Chem* **2019**, *5* (7), 1861-1870. DOI: 10.1016/j.chempr.2019.04.021 (acccessed 2024/07/11).

(76) Bahari, M.; Jing, Y.; Jin, S.; Goulet, M. A.; Tsukamoto, T.; Gordon, R. G. 200-fold lifetime extension of 2,6-dihydroxyanthraquinone during flow battery operation. *ChemRxiv* **2024**. DOI: 10.26434/chemrxiv-2024-grfq9.

(77) Goulet, M.-A.; Tong, L.; Pollack, D. A.; Tabor, D. P.; Odom, S. A.; Aspuru-Guzik, A.; Kwan, E. E.; Gordon, R. G.; Aziz, M. J. Extending the Lifetime of Organic Flow Batteries via Redox State Management. *Journal of the American Chemical Society* **2019**, *141* (20), 8014-8019. DOI: 10.1021/jacs.8b13295.

(78) Jing, Y.; Zhao, E. W.; Goulet, M.-A.; Bahari, M.; Fell, E. M.; Jin, S.; Davoodi, A.; Jónsson, E.; Wu, M.; Grey, C. P.; et al. In situ electrochemical recomposition of decomposed redox-active species in aqueous organic flow batteries. *Nature Chemistry* **2022**, *14* (10), 1103-1109. DOI: 10.1038/s41557-022-00967-4.

(79) Wang, Q.; Zakeeruddin, S. M.; Wang, D.; Exnar, I.; Grätzel, M. Redox Targeting of Insulating Electrode Materials: A New Approach to High-Energy-Density Batteries. *Angewandte Chemie International Edition* **2006**, *45* (48), 8197-8200. DOI: https://doi.org/10.1002/anie.200602891.

(80) Wang, X.; Chai, J.; Jiang, J. J. Redox flow batteries based on insoluble redox-active materials. A review. *Nano Materials Science* **2021**, *3* (1), 17-24. DOI: https://doi.org/10.1016/j.nanoms.2020.06.003.

(81) Fan, S.; Liu, Y.; Gao, Y.; Liu, Y.; Qiao, Y.; Li, L.; Chou, S.-L. The design and synthesis of Prussian blue analogs as a sustainable cathode for sodium-ion batteries. *SusMat* **2023**, *3* (6), 749-780. DOI: https://doi.org/10.1002/sus2.170.

(82) Chen, Y.; Zhou, M.; Xia, Y.; Wang, X.; Liu, Y.; Yao, Y.; Zhang, H.; Li, Y.; Lu, S.; Qin, W.; et al. A Stable and High-Capacity Redox Targeting-Based Electrolyte for Aqueous Flow Batteries. *Joule* **2019**, *3* (9), 2255-2267. DOI: https://doi.org/10.1016/j.joule.2019.06.007.

(83) Cheng, Y.; Wang, X.; Huang, S.; Samarakoon, W.; Xi, S.; Ji, Y.; Zhang, H.; Zhang, F.; Du, Y.; Feng, Z.; et al. Redox Targeting-Based Vanadium Redox-Flow Battery. *ACS Energy Letters* **2019**, *4* (12), 3028-3035. DOI: 10.1021/acsenergylett.9b01939.

(84) Fan, L.; Jia, C.; Zhu, Y. G.; Wang, Q. Redox Targeting of Prussian Blue: Toward Low-Cost and High Energy Density Redox Flow Battery and Solar Rechargeable Battery. *ACS Energy Letters* **2017**, *2* (3), 615-621. DOI: 10.1021/acsenergylett.6b00667.

(85) Schröter, E.; Stolze, C.; Saal, A.; Schreyer, K.; Hager, M. D.; Schubert, U. S. All-Organic Redox Targeting with a Single Redox Moiety: Combining Organic Radical Batteries and

Organic Redox Flow Batteries. *ACS Applied Materials & Interfaces* **2022**, *14* (5), 6638-6648. DOI: 10.1021/acsami.1c21122.

(86) Zhu, Y. G.; Du, Y.; Jia, C.; Zhou, M.; Fan, L.; Wang, X.; Wang, Q. Unleashing the Power and Energy of LiFePO4-Based Redox Flow Lithium Battery with a Bifunctional Redox Mediator. *Journal of the American Chemical Society* **2017**, *139* (18), 6286-6289. DOI: 10.1021/jacs.7b01146.

(87) Goulet, M.-A.; Aziz, M. J. Flow Battery Molecular Reactant Stability Determined by Symmetric Cell Cycling Methods. *Journal of The Electrochemical Society* **2018**, *165* (7), A1466. DOI: 10.1149/2.0891807jes.

(88) Jeong, S.; Kim, L.-H.; Kwon, Y.; Kim, S. Effect of nafion membrane thickness on performance of vanadium redox flow battery. *Korean Journal of Chemical Engineering* **2014**, *31* (11), 2081-2087. DOI: 10.1007/s11814-014-0157-5.

(89) Jiang, B.; Wu, L.; Yu, L.; Qiu, X.; Xi, J. A comparative study of Nafion series membranes for vanadium redox flow batteries. *Journal of Membrane Science* **2016**, *510*, 18-26. DOI: https://doi.org/10.1016/j.memsci.2016.03.007.

(90) Luo, Q.; Zhang, H.; Chen, J.; You, D.; Sun, C.; Zhang, Y. Preparation and characterization of Nafion/SPEEK layered composite membrane and its application in vanadium redox flow battery. *Journal of Membrane Science* **2008**, *325* (2), 553-558. DOI: https://doi.org/10.1016/j.memsci.2008.08.025.

(91) Zeng, J.; Jiang, C.; Wang, Y.; Chen, J.; Zhu, S.; Zhao, B.; Wang, R. Studies on polypyrrole modified nafion membrane for vanadium redox flow battery. *Electrochemistry Communications* **2008**, *10* (3), 372-375. DOI: https://doi.org/10.1016/j.elecom.2007.12.025.

Chapter 2. Redox Targeting of Sodium Superionic Conductors in Aqueous Anolytes for High-Energy-Density Batteries

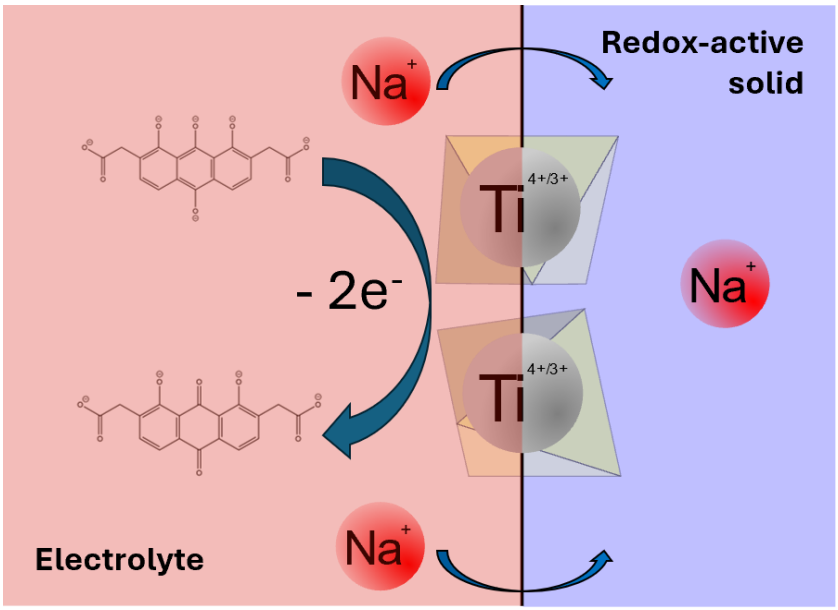

2.1 Overview

Electrolyte-solid additive interfacial charge transfer chemistry, otherwise known as "redox targeting" within redox flow battery (RFB) literature, is a promising solution to break the barrier of energy densities as determined by the solubility limits of electrolytes. The addition of an energy-dense redox-active solid extends the charge capacity of the electrolyte reservoir with minimal volumetric expansion of the reservoir tank. Currently, few examples of redox targeting chemistries exist for aqueous negative electrolyte (anolytes) and are greatly outperformed by all aqueous redox targeting positive electrolyte (catholyte) systems. Here, we present a system comprised of the sodium superionic conductor $NaTi_2(PO_4)_3$ (NTP) with two anthraquinone-based electrolytes, a single redox shuttle and a dual redox shuttle molecular system. We probe the thermodynamics and kinetics of the redox targeting with NTP, illustrating the impact on a multitude of battery performance metrics and how they are influenced by the redox reaction driving forces and the employed current densities. Furthermore, we highlight the slow internal

redox kinetics within the core of NTP crystals require a high-surface area immobilization strategy to maximize the battery efficiency. Optimizing for the thermodynamic and kinetics considerations, we have developed a redox targeting system achieving over 100% of the electrolyte capacity alone, the first demonstration of a shift in primary shift energy storage from the electrolyte to the high-energy-density solid for aqueous anolytes.

2.2 Introduction

To achieve net zero emissions by 2050, electricity generation from fossil fuels will need to be replaced with clean alternative technologies, such as wind, solar, geothermal, and/or tidal. Electricity is the most in-demand energy source and with widespread electrification expected to significantly rise, the electricity demand is forecasted to increase up to 40% by 2050.[1] Electrification of existing technologies and the introduction of new electric technologies are the key drivers for the predicted increase in demand, with sectors, such as transportation and heating, to expect the greatest transition toward electric. This evolving energy demand will shift current peak loads timings on the grid, affecting grid operations, reliability, and energy markets. Currently, fossil fuels remain the dominant source for grid electricity generation, making up ~60% of the grid's capacity.[2] There are various renewable sources contributing to the grid but two of the major sources, wind and solar, suffer from intermittency. Solar is impacted by the number of daylight hours and the weather. In the summer months, solar does contribute more to the electricity supply, however, this is reversed in the winter months. Furthermore, wind is highly unpredictable all year-round. These two sources contribute ~14% of the US grid electricity generation.[2]

Scalable, cost-effective, and long-duration storage solutions are a prerequisite for decarbonization of the grid, whereby the intermittency of renewables can be compensated by stored forms of energy, hence, enhances the resiliency of the grid. A diverse array of energy

storage systems (ESSs) will be required to cope with the often-predictable electrical fluctuations throughout the day and usher in the transition to decarbonization of the energy sector.[3,4] The variety of ESSs can satisfy the broad range of characteristics demanded to cater for capacity, power, and discharge timescales design criteria, as no single ESS solution can technically or financially fulfil all the criteria demands.[5,6] A key evaluation metric for the role of an ESSs is discharge duration – the ratio of the energy capacity over power rating – to determine the application the ESS is best suited for. Currently by capacity, the world's most developed energy storage technology is pumped hydro. Although a valuable energy storage source, installations of these are limited due to geographical technology requirements. Electrochemical solutions, such as battery energy storage systems (BESSs), have long been projected as an energy storage solution for the grid that can be deployed virtually anywhere. In recent years, large stationary MW-capacity lithium-ion (Li-ion) battery have been installed globally with the goal to rapidly multiply the storage capacity to prepare for current and future energy demands.[7] Short-duration batteries typically can discharge for 4 – 6 hours, ideal to assist the grid during peak demand, whereas long-duration batteries discharge range is 10+ hours, enhancing grid reliability versus its short-duration counterparts.[8]

Stationary grid-scale electrical energy storage is a process for excess electrical energy to be stored as chemical or potential energy, which can be transformed back into electricity upon demand. These systems can alleviate a power supply shortage, such as assisting in demand spikes, which in turn avoid quickly ramping steam generators, ensuring the safe and stable operation of the power grid. A BESS would provide more value than a conventional generator or turbine of similar capacity size because of the fast responsive times. Installing more BESSs with fast response times would more efficiently meet the grid's capacity demands, as these are better suited to ramping versus conventional generators, eliminating the need for backup conventional generators.[9] Wider deployment of grid-scale ESSs would facilitate greater investment in renewable energy sources, encouraging the energy transition from fossil fuels to renewables.

Beyond safely and quickly responding to demand spikes, another benefit from the proliferation of electrical energy storage systems is peak shaving, whereby long-duration storage solutions would charge up when electricity demand is weak, therefore, when the price of electricity is cheaper. This electricity can then be discharged at peak demand times when the real time electricity cost is higher.

Redox flow batteries (RFBs) have been envisioned as grid-scale ESS and as a potential solution to addressing the long-duration storage requirements to assist in supplying the grid, especially compensating for the intermittency of renewable sources.[7] Two reservoir tanks store dissolved redox-active species within liquid electrolytes which are pumped into an electrochemical cell, where they are separated by an ion-exchange membrane to maintain charge neutrality, converting the stored chemical energy within the electrolyte into electrical energy and vice versa. The energy is determined by the concentration and volume of the electrolyte reservoirs and the power is determined by electrode active surface area and the number of cells in the battery stack.[10-12] This unique architectural separation decouples the energy capacity from the maximum power output, therefore, low-cost long-duration discharge is a possibility with RFB technology.[13, 14]

Aqueous redox flow batteries (ARFBs) are inherently safe employing water-based electrolytes which are non-flammable, crucial for grid-scale BESS, reducing the infrastructure costs and widens the number of suitable geographical installation sites.[15, 16] Vanadium RFBs (VRFBs) are the most mature ARFB technology and the only MW-capacity installations globally. However, widescale adoption is limited by the toxicity of the electrolytes, the price-volatility, and generally high cost of vanadium precursors.[17-20] An alternative are aqueous organic redox flow batteries (AORFBs) which are comprised of earth-abundant and cheap elements, such as carbon, oxygen, hydrogen, and nitrogen.[21-23] Furthermore, these organic redox-active molecules are infinitely tunable through structural modifications. This molecular diversity enables targeting

desirable electrochemical properties, such as high solubilities, fast redox kinetics, chemical stability, and the required redox potential.[21, 23-26]

Many different classes of redox-active organics have been studied for AORFBs, including quinone,[27-31] viologen,[32-35] phenazine,[36-38] alloxazine,[25, 36] and (2,2,6,6-tetramethylpiperidin-1-yl)oxyl (TEMPOs)[33, 34] derivatives. The majority of molecules reported are not chemically stable, therefore, not fit for long-duration discharge applications. There are a few examples of anthraquinone[39-41], phenazine[42], and viologen[43, 44] derivatives that exhibit excellent long-term cycling stability. Anthraquinones are advantageous over viologens because these are vulnerable to react with protons and hydroxide, resulting in side-reactions, affecting the energy efficiency and alters the electrolyte pH.[43] Furthermore, phenazines require expensive precursors and precious metal catalysts for their syntheses, hindering their up-scale manufacture.[42] Dihydroxyanthraquinones (DHAQs) vary significantly in cost depending on the isomer – the position of the hydroxy substituents. Many are commercially available at a low cost, however, 2,6-DHAQ and 2,7-DHAQ are particularly expensive because these are synthesized as a mixture and suffer from high purification costs.[41]

DHAQs possess redox potentials that span -0.74 to -0.90 V vs Ag/AgCl, making them suitable redox mediators for aqueous anolytes and they also demonstrate fast redox kinetics, however, the solubilities of these are low with most saturating at >0.2 M.[27] A strategy to impart higher solubility, would be to add ionic substituent groups to the molecular structure, such as – SO_3^-, – COO^-, and – NR_3^+. Conveniently, the hydroxy groups can be easily modified via a Williamson ether synthesis to add a solubilizing functional group, such as polyethylene glycol and alkyl ammonium chains, boosting the solubilities >1 M.[28, 39, 45] Furthermore, hydrotropic additives, such as urea, caffeine, and nicotinamide, can improve the solubility of poorly soluble organic molecules.[42, 46] Although these systems can demonstrate high volumetric capacities, the additives and the redox-active molecules are at high concentrations (2 – 5 M) that the viscosity of

the electrolyte complicates the fluid dynamics of the system and the hydrotropic additives can inhibit the redox kinetics of one or both of the redox-active species in the two electrolyte reservoirs.[27]

An alternative strategy for achieving high-energy-density flow batteries is the addition of a redox-active solid additive to the electrolyte reservoir tanks, merging materials commonly used in solid-state batteries within RFBs to hybridize the advantages of each technology.[12, 47, 48] Redox-targeting redox flow batteries (RT-RFBs) combine the high energy density of redox-active solids with the RFB platform that decouples energy and power, while maintaining a low-cost, scalable ESS. In addition to the redox chemistry occurring in the battery stack, the redox-targeting redox reaction in the reservoir tank involves the redox-active solid acting as an energy sink during a charge cycle. Upon charging, the redox mediator reduces at the electrode within the battery stack, this then is pumped into the reservoir tank and encounters the redox-active solid surface and undergoes interfacial charge transfer, reducing the solid and oxidizing the redox mediator. This redox mediator is then available to collect more electrons back at the electrode, effectively increasing the charge capacity of the system. The following discharge step applies an oxidizing current, this will oxidize the redox mediator at the electrode. Once returned to the reservoir, it is recharged by the redox-active solid, further extending the discharge capacity. Therefore, when discharging, the solid becomes a charge source for the redox mediator. Thus, redox targeting can in theory dramatically increase the volumetric energy density of a reservoir. For ARFBs, redox targeting has been demonstrated in the catholytes with the charge capacity improving nearly 4-fold,[48-50] however, redox targeting anolyte systems have been elusive. A report achieved a modest ~37% capacity boost pairing a polysulfide electrolyte with $LiTi_2(PO_4)_3$ solid medium.[49] A high-energy-density anolyte is required along with a well-performing redox targeting catholyte for a RT-RFB to supersede existing established RFB technologies.

Here, we report $NaTi_2(PO_4)_3$ (NTP) as a high-energy-density solid suitable for redox targeting in aqueous anolytes. NTP in Na^+ batteries is found to be robust even after thousands of charge/discharge cycles,[51] but it has not been studied in aqueous redox reactions. To demonstrate NTP's potential in aqueous redox targeting flow battery applications, we are using different electrolytes with a particular focus on a single shuttle electrolyte (SSE) versus a dual shuttle electrolyte (DSE), whereby both electrolytes are organic anthraquinone derivatives.

2.3 Results and discussion

Employing a solid-electrolyte system whereby both components have similar redox potentials (±30 mV), makes it thermodynamically favorable for reversible charge transfer between the liquid and solid components.[52] Alternatively, a liquid electrolyte consisting of a pair of redox-active species can have redox potentials the straddles that of the solid additive. Figure 2.1 shows cyclic voltammograms (CVs) of NTP (carbon coated, on an electrode) and the two electrolytes studied here. NTP shows cathodic and anodic peaks at -0.82 and -0.72 V vs Ag/AgCl, respectively. The reduction wave corresponds to a two-electron process accompanied by intercalation of two Na^+ ions to form $Na_3Ti_2(PO_4)_3$.[53] One mole of NTP thus contains two moles of reducible Ti^{4+}. To evaluate the redox-targeting effect on capacities, a galvanostatic H-cell was used to measure the charge-discharge capacities of the anolyte without and with NTP (Figure A.12, see Appendix A. for details).

The equimolar mixture of anthraflavic acid and anthraquinone-2,7-disulfonic acid disodium salt (2,7-ADS) in 0.1 M NaOH (pH ~ 13) shows two sets of redox peaks, with redox potentials at -0.91 and -0.51 V vs Ag/AgCl, respectively. Likewise, the mixture of $[Fe(TEOA)OH]^{-/2-}$ and $[Mn(TEOA)OH]^{-/2-}$ complexes in 5 M NaOH (pH ~ 14) shows two sets of peaks with redox potentials at -1.0 and -0.43 V vs Ag/AgCl, respectively. The redox waves of each mixed electrolyte bracket those of NTP, and these two electrolytes should therefore be capable of charging and

discharging NTP. We note that selection of electrolytes that more tightly match the redox potential of NTP will improve battery energy efficiency, but the initial focus here is on assessing NTP's fundamental viability as a redox-active solid for aqueous anolytes.

Figure A.13a shows the voltage profile of a single charge/discharge cycle using the organic anolyte. Because these anthraquinones undergo two-electron reduction, the maximum charge/discharge capacity of this electrolyte is 19.3 C (5.36 mAh, dashed vertical line) based on concentration, compared to the experimental charge/discharge capacity of 16.9/15.7 C (4.69/4.36 mAh). Repeating the measurement with 4 molar equivalents (0.4 mmol) of NTP in the H-cell, the charge and discharge capacity increased nearly fourfold, reaching ~67.0 C and ~60.0 C (~18.6 and ~16.7 mAh), respectively. Powder X-ray diffraction confirms reversible changes in the NTP crystal structure when reduced and reoxidized during cycling (Figure A.8). These data thus demonstrate successful aqueous redox targeting.

Critically, these results show that more charge can now be stored in the solid state than in the liquid electrolyte itself. Such inversion has not been previously observed in any aqueous redox-targeting anolyte. Quantitatively, the 4-equivalents data translate to a volumetric capacity of at least 1.67 Ah L^{-1}. Although low compared to typical RFB volumetric capacities, this reflects a physical limitation of the H-cell configuration, and the results below indicate that there is no fundamental chemical limitation to increasing both electrolyte and NTP concentrations that would prevent transitioning from H-cell to RFB configurations.

Figure A.13b plots relative charge/discharge capacities vs equivalents of NTP in the anolyte. Relative capacities were calculated as $Q_R(\%) = {}^{Q_{exp}}\!/_{Q_{el}} \times 100\%$, where Q_{exp} is the experimentally measured charge or discharge capacity with NTP, and Q_{el} is the experimental charge/discharge capacity of the electrolyte without NTP is 4.69/4.36 mAh (16.9/15.7 C). These data show steadily increasing capacities with NTP addition, indicating reversible redox targeting between the electrolyte and NTP at various relative concentrations. The data in Figure A.13b

(dashed line) indicate ~60% $Ti^{4+/3+}$ use during cycling, similar to the 60–80% capacity utilization of NTP anodes in sealed Na^+ batteries.[51, 54-56]

The stability of this redox-targeting system was tested by charge/discharge cycling. Figure A.14b shows data for 12 charge-discharge cycles capacities and Coulombic efficiencies vs cycle number of the anthraflavic acid/2,7 ADS mixture without and with the addition of 1 molar equivalent of NTP (0.1 mmol), measured at ±5 mA. One equivalent of NTP increases the average charge/discharge capacities from 16.2/15.5 to 29.5/28.0 C (4.50/4.31 to 8.19/7.78 mAh), and only minimal capacity fade is observed with cycling over many hours. High Coulombic efficiencies of ~95% are maintained throughout. These data thus demonstrate good stability and cyclability of this electrolyte/NTP system.

To test the versatility of NTP as a solid-state charge-storage material for RFBs, we also examined transition-metal electrolytes in place of the organics described above. Proof-of-concept results are presented for electrolytes involving $[Fe(TEOA)OH]^{-/2-}$ and $[Mn(TEOA)OH]^{-/2-}$. $[Fe(TEOA)OH]^{-/2-}$ has been explored as an RFB anolyte,[57-59] but $[Mn(TEOA)OH]^{-/2-}$ has received no attention. This electrolyte contrasts the anthraquinone mixture in that the redox reactions are simpler, the pH is higher (~14 vs ~13), and lower currents are used. Addition of 1 equivalent of NTP increases the capacity by roughly 40%, similar to the anthraflavic acid/2,7-ADS mixed electrolyte. Figure A.14c plots the capacities and Coulombic efficiencies for this anolyte measured over 10 charge/discharge cycles without and with 1 molar equivalent of NTP. Good cycling stability is observed, albeit with a smaller Coulombic efficiency than found for the anthraquinones. Overall, these results illustrate redox targeting of NTP using a second, distinct electrolyte. Furthermore, these electrolyte systems with strong charge transfer driving forces demonstrate the accesible volume of the NTP is 60%. The theoretical specific capacity of NTP is 133 mAh g^{-1}, resulting in the accessible specific capacity of 79.8 mAh g^{-1}.

Upon initial inspection, 1,8-DHAQ and 1,5-DHAQ have a redox potentials of -0.78 and -0.76 V vs Ag/AgCl, each with a 10 mV difference with the redox potential of NTP, therefore, it is thermodynamically favorable to reversibly charge transfer with NTP. However, with galvanostatic H-cell experiments, it was evident that in the presence of NTP had a detrimental effect on the measured capacity (Figure A.11a).

To corroborate the capacity drop, Figure A.11b shows CVs that were measured before and after cycling along for 1,5-DHAQ. The concentration of redox-active species within the electrolyte is proportional to the CV current response (eq. A.2) and it was evident the ratio of capacities without and with NTP was identical to the ratio of CV current response before and after cycling, highlighting a 14% reduction. We hypothesis the lack of redox targeting and the effective concentration reduction is due to the affinity of the reduced molecule to bind to the titanium metal centers via the deprotonated enol and hydroxy groups. These molecules effectively have precipitated from the electrolyte so no longer participate in redox reactions at the electrode. Furthermore, the bound reduced molecule shields NTP, preventing redox-targeting redox-reactions with the electrolyte. The 1,8-DHAQ derivative suffers from low water solubility, 0.08 M at pH 14, hindering applications in AORFBs.

FnChrysazin, a carboxylic acid derivative of 1,8-DHAQ synthesized and reported by Wu et al.,[60] demonstrate a redox potential of -0.76 V vs Ag/AgCl and a solubility of 1.3 M at pH 14. Therefore, FnChrysazin, with its superior solubility, is necessary to circumvent the NTP surface passivation and to achieve a high-energy-density aqueous anolyte. Herein, we employ FnChrysazin for the SSE. The DSE is an equimolar mixture of FnChrysazin and 2,7-ADS, showing two redox features with redox potentials at -0.76 and -0.51 V vs Ag/AgCl at pH 14, respectively.

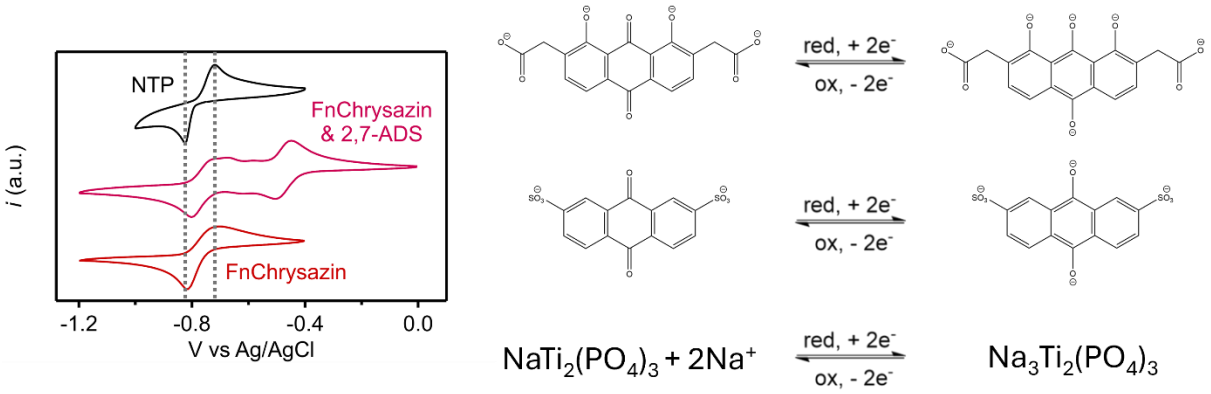

Figure 2.1 Cyclic voltammograms of NTP (on glassy carbon electrode, 0.5 mV s^{-1} in 1 M Na_2SO_4), an organic mixed electrolyte (5 mM FnChrysazin, 5 mM 2,7-ADS, 1 M NaOH, 100 mV s^{-1}), and FnChrysazin electrolyte (10 mM, 1 M NaOH, 100 mV s^{-1}), offset vertically for clarity. The dashed vertical lines indicate the potentials of the peaks of NTP. Relevant redox reactions are shown on the right.

In a galvanostatic H-cell experiment with the SSE, Figure A.19a shows a single charge-discharge voltage profile using only FnChrysazin without and with NTP. The theoretical capacity of the electrolyte, which undergoes a two-electron redox reaction, is 5.36 mAh (dashed horizonal line, Figure A.19b). The experimental charge/discharge capacities achieved are 3.38/3.22 mAh. Repeating the experiment with the addition of one molar equivalent (0.1 mmol) of NTP in the H-cell anolyte, the charge/discharge capacities increased to 4.54/4.12 mAh. This represents a charge and discharge capacity increase of 34 and 28%, respectively, demonstrating successful redox targeting within this system. We note the capacities with the NTP addition do decay, but this is due to the physical constraint of the H-cell with NTP settling in regions of worse electrolyte flow. Theoretically, the capacities should double with one molar equivalent NTP addition, however, it is evident in Figure A.19b that upon the initial charge and discharge cycle that more charge is injected into the system and less is extracted. The subsequent cycles show a reduction in charge injection but an increase in charge extraction, hence, high Coulombic efficiency is achieved from cycle 2. These results suggest that the reduction of NTP by FnChrysazin is more favorable than oxidation of NTP. These have remarkably similar redox potentials that indicate,

thermodynamically, reversible charge transfer will occur, however, the anodic wave of the NTP CV is broader than the cathodic wave suggesting more quasi-reversible properties. This potentially indicates the oxidation reaction requires a greater thermodynamic driving force to achieve high material utilization.

We know using redox mediators with strong charge transfer driving forces in both directions increases capacities by ~60%, so in theory an equimolar mixture of FnChrysazin and 2,7-ADS should achieve high material utilization with the additional oxidative driving force of 2,7-ADS. Figure A.20a shows a charge-discharge voltage profile of the FnChrysazin/2,7-ADS mixture. Like the SSE, the capacities increase with one molar equivalent addition of NTP. However, the charge/discharge capacities increased from 3.12/3.01 to 7.16/6.80 mAh after the NTP addition. This represents a 126% average discharge capacity increase to the system. We note this is greater than the NTP theoretical capacity increase, however, the capacity of the electrolyte alone was ~55% of the theoretical capacity so the total capacity increase of the system may also, in part, be due to enhanced electrolyte performance.

While useful for screening redox systems, H-cells suffer from low performance due to mass transfer limitations and poor mixing of electrolytes and solids. To further optimize the redox targeting systems, we moved to a flow battery configuration. The transfer of chemistry from the H-cell pilots to a flow battery requires an immobilization strategy for the redox-active solid. Commonly, the active material is pressed into pellets with carbon, for conductivity, and polyvinylidene fluoride (PVDF) binder.[49, 50] The mass of active material in the pellets can vary from 70 to 85%. It has been demonstrated that $LiTi_2(PO_4)_3$, the lithium counterpart to NTP, only produces a modest capacity increase of 37%.[49] Although the pellets are porous, this immobilization strategy is a low surface area solution. To maximize redox targeting, various immobilization strategies were investigated.

To screen NTP immobilization methods we first used the equimolar mixture of 25 mM each anthraflavic acid and 2,7-ADS in 1 M NaOH. The highest surface area achievable is to employ the NTP powder within a powder inline filter, fitted with a particle exclusion membrane (Figure A.1). In a flow battery configuration, Figure A.15a shows flow battery data for 10 mL of anolyte with one molar equivalent of NTP in the powder inline filter cycled at a current density of 10 mA cm^{-2}. The initial 10 cycles show stable and impressive capacities with the charge/discharge capacities increasing from 29.3/28.4 to 53.8/50.4 mAh - this is an 80% capacity increase. This translates to 80% material utilization, which is the upper end of prior reported values.[51, 54-56] However, with time, the powder settles in the filter where the electrolyte flow is the poorest, reducing the available surface area for redox targeting, resulting in a capacity decay with cycling. Resolving this issue requires a complex engineering solution. However, accepting the surface area will be reduced, immobilizing the NTP powder to a substrate will allow the NTP to remain suspended within the flow of the electrolyte to result in sustained redox targeting. These results pointed towards the need for a high-surface-area morphology of NTP and proper mixing with the anolyte in a flow-through configuration.

We first explored 2-D immobilization method by depositing NTP on strips of flexible polypropylene mesh and incorporating them into an inline filter. Figure A.16 shows baseline anolyte cycling data for 100 mL of anolyte. After establishing good baseline performance (~83 mAh out of a theoretical maximum of 107 mAh), the filter with NTP/polypropylene strips was added to the anolyte flow path. The capacity increased to ~220 mAh, a 165% capacity boost. The Coulombic efficiency, however, was low compared to the electrolyte alone, and the capacity faded with cycling. Given this 2-D configuration of NTP in a tightly coiled strip (Figure A.2), we believe that mixing of the entire surface of the strip with the anolyte is difficult. For example, layers of the strip may be pressed against each other, preventing proper mixing with the anolyte. Additionally, the strip remained stained with the electrolyte after disassembling and washing with deionized water, indicating that the anthraquinones remain bound to the surface of the strip.

These factors could ultimately lead to a capacity fade with cycling. We note, however, that the capacity remained high, and the fade was significantly less than the loose powder configurations, where the NTP settled and became inaccessible to the anolyte.

Next, we explored a 3-D configuration of the NTP medium. Figure A.6 shows NTP that was directly synthesized as a high-surface-area foam using polyurethane sponge substrates. These NTP foams were treated with Nafion ionomer to give structural support, prevent dissolution, and facilitate Na^+ exchange during redox reactions. Flow battery cycling measurements were conducted by adding the 60 pores-per-inch (ppi) Nafion-coated NTP foams to an inline filter and incorporating them into the anolyte flow path. Figure A.17 shows flow battery cycling data using 10 mL of anolyte and 0.937 g (~4.8 equivalents, 125 mAh) of the Nafion-coated NTP foams. We note the upper most foam was not submerged below the level of the anolyte so mixing with the electrolyte was suboptimal. The return line was dripping the anolyte onto the uppermost part of the foam. A large capacity boost was observed and maintained for the first 7 cycles, before the capacity began to fade linearly with cycling.

We hypothesize that the capacity fade is due to the NTP foam compacting, and as it compacts, the core volume of the macrostructure becomes inaccessible to the anolyte. In the extreme case of NTP powder, we observed that as powder settles in the inline powder filter and becomes inaccessible to the anolyte, the capacity fades drastically. Therefore, we synthesized NTP using a denser, 100 ppi polyurethane foam substrate. This is overall a more durable macrostructure with a more comprehensive network of NTP pores to prevent compacting, and therefore its volume would remain accessible to the anolyte.

Incorporating 0.867 g (~4.3 equivalents, 115 mAh) of the 100 ppi Nafion-coated NTP foams into a flow battery, using the same electrolyte conditions as the 60 ppi experiment but at half of the current density (5 mA cm^{-2}). Figure A.18a shows the capacity increases by 37%. This is significantly poorer NTP utilization compared to the more porous 60 ppi Nafion-coated NTP

foams. However, the capacities were stable throughout the cycling measurement, which at half the current, thus longer cycling times, confirm the denser 100 ppi Nafion-coated NTP foams are robust and show little to no degradation. These foams demonstrate an NTP utilization of ~9% vs the more porous 60 ppi foams with an NTP utilization of 57%.

The denser foam morphology hinders the flow of electrolyte and forces the majority of the electrolyte to find the path of least resistance. This poor mixing between the NTP and the electrolyte effectively reduces the active surface area for interfacial charge transfer, therefore, counters efforts to increase the surface area through the high-density foam macrostructure. It is evident that a degree of porosity is required for any redox-active material-bearing matrix to achieve uniform fluid flow throughout the redox filter. The Nafion-coated NTP foams are near-pure NTP structures, therefore, the structure is a hard, but brittle, ceramic foam.

Composites are employed in many applications to merge the desirable properties of various components, resulting in a product that outperforms any pure material counterpart. The porosity of the 60 ppi Nafion-coated NTP foam demonstrated high surface area and NTP utilization at short timescales, therefore, these foams do not significantly impede the electrolyte flow and facilitate high material utilization. The polyurethane foam was a template that was calcined away in the synthesis of the Nafion-coated NTP foam; however, this substrate can act as a skeleton for the redox-active solid. Silicone caulk is a suitable binding agent due to good chemical resistance and viscosity properties making it ideal for the basic electrolytes in this work and pliable to coat the foam substrate. A thin layer of NTP powder can be bound to the polyurethane foam using silicone caulk, mimicking the Nafion-coated NTP foam, whereby the surface area of the foam macrostructure is the redox-active NTP. A proportion of the NTP is inactive for the Nafion-coated NTP foams due to the charging mechanism limitations of ionic diffusion through the lattice, therefore, this composite NTP foam strategy facilitates efficient

material utilization and conserves resources, substituting the core materials of the composite macrostructure for cheap, widely available materials.

Galvanostatic charge and discharge flow battery measurements of the FnChrysazin electrolyte without NTP foam composites demonstrated a charge/discharge capacity of 18.2/17.9 mAh (theoretical maximum is 21.4 mAh). The addition of the NTP foam composite redox filter (0.246 mg NTP, ~1.5 equivalent, 33 mAh) demonstrates stable redox targeting with the capacity growing in over the first 35 cycles. The cycling time for the first 35 cycles is the equilibrium time required for electrolyte to flow through the NTP foam composites optimally, thus undergoing more interfacial charge transfer. Figure 2.2a shows that after cycle 35 the charge/discharge capacities no longer increase and remain stable at 21.4/21.0 mAh. This equates to a 17% discharge capacity boost. Operating at lower current densities, this capacity increase can be extended to 26.8/26.6 mAh using a current density of 2.5 mA cm^{-2}. This is a 49% discharge capacity boost, surpassing the prior redox targeting in aqueous anolytes benchmark of 37%.[49] Furthermore, FnChrysazin exhibits fast redox kinetics which alleviates the requirement of a catalyst embedded electrode to kinetically improve the redox reaction, a possible long-term capacity decay pathway.

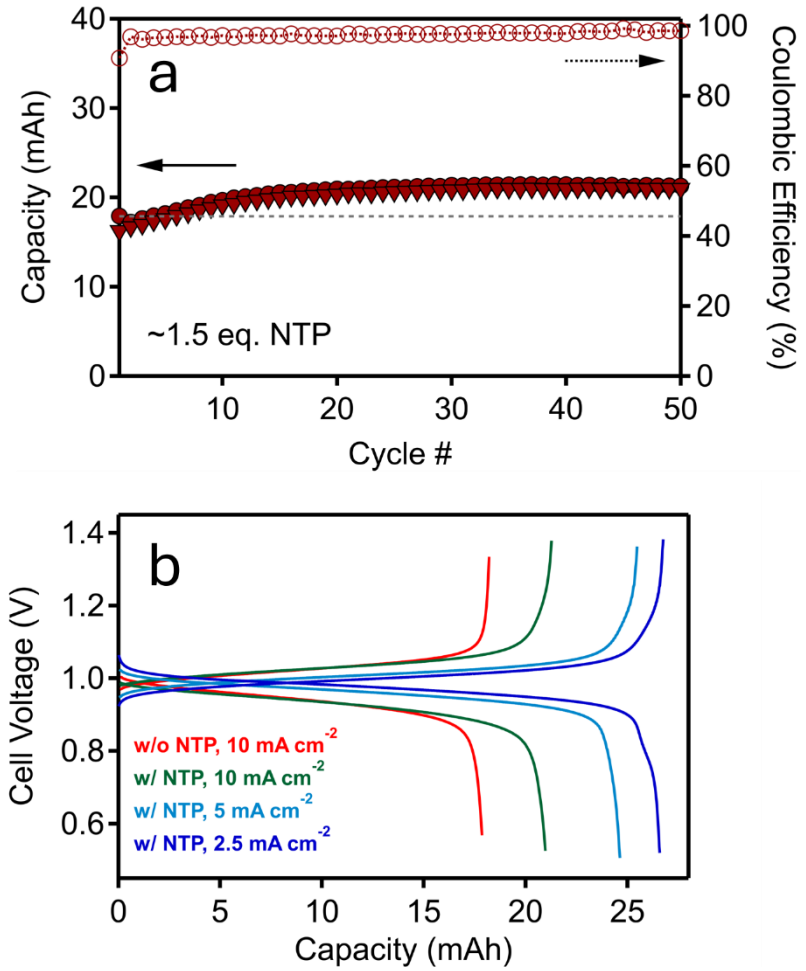

Figure 2.2 (a) Flow battery measurement of capacity (left axis, solid lines) and Coulombic efficiency (right axis, dashed lines) vs cycle number of 8 mL 50 mM FnChrysazin in 1 M NaOH with ~1.5 molar equivalents (0.246 g) of NTP foam composites. The catholyte is 100 mL $Na_4[Fe(CN)_6]$ in 1 M NaOH. Charge capacity is indicated by circles, and discharge capacity is indicated by triangles. The dashed gray line represents the discharge capacity of the electrolyte alone based on prior cycling without NTP foam composite redox filter. **(b)** Voltage profiles of a single charge/discharge cycle at various current densities with the NTP foam composite redox filter. Data at lower current densities was collected subsequently after 50 cycles at 10 mA cm^{-2}.

By employing lower current densities, the bulk electrolyte potential fluctuates more slowly due to the reduced rate of charging/discharging that occurs at the electrode. In effect, this increases the resonance time between the electrolyte and NTP within the reservoir tank. The increased mixing time compensates for the interfacial charge transfer redox kinetics, enabling greater material utilization, thus demonstrating a significant improvement in the system energy

density. To underpin the correlation between capacity boost and redox targeting kinetics, we performed RFB cycling at different current densities. Figure A.21 shows that cycling the electrolyte alone at varying current densities only produces a marginal increase in capacity, as expected with the fast redox kinetics of FnChrysazin. In contrast, using lower current densities when NTP is present shows a much greater boost in capacity compared to higher current densities.

As observed in the H-cell data prior and in Figure A.19b, the first cycle of FnChrysazin and NTP shows poor Coulombic efficiency, indicating an imbalance and a weak NTP oxidative driving force. Repeating the same measurement with 8 mL of 25 mM each of FnChrysazin and 2,7-ADS in 1 M NaOH shows a charge/discharge capacity of 15.2/15.0 mAh (theoretical maximum is 21.4 mAh). This mixture provides a greater oxidative/reductive driving force as indicated by the CVs in Figure 2.1a. Figure 2.3a shows the addition of the NTP foam composite redox filter (0.306 mg NTP, ~1.9 equivalent, 41 mAh) demonstrates stable redox targeting, albeit lower capacity boost than the FnChrysazin electrolyte Over the course of the 50 cycles rises steadily as the electrolyte flow improves through the NTP foam composites. However, the capacity growth is very small and the charge/discharge capacities are 16.2/16.1 mAh with the NTP foam composite redox filter. This is an 8% discharge capacity boost, significantly less than the single redox mediator system which also employed less NTP. This DSE contains the same concentration of redox-active anthraquinones as the SSE, therefore, the FnChrysazin concentration is half of the prior system. The expectation was the 2,7-ADS would oxidize the reduced NTP, which would be evident in the voltage profiles by an elongated 2,7-ADS discharge plateau at ~0.65 V. We observe from the prior H-cell data, that FnChrysazin is responsible for charging and discharging NTP powder. The current density and FnChrysazin concentration are not optimal for redox targeting with NTP, however. As was observed for the SSE, employing lower currents compensates for the slow redox targeting kinetics. Galvanostatic cycling at lower currents increases the charge/discharge capacities to 25.2/24.9 mAh at 5 mA cm^{-2} which are further extended to 31.6/31.1 mAh at 2.5 mA

cm^{-2}. This is a 67 and 108% discharge capacity boost, respectively. The NTP utilization when the applied current density was 5 and 2.5 mA cm^{-2} is 35 and 57%, respectively, the latter being close to the NTP utilization limit observed from the H-cell data. We note, similar to the initial 50 cycles at 10 mA cm^{-2}, the capacities are steadily increasing throughout the additional cycles (Figure A.22).

Similar to the prior H-cell data, the voltage profiles in Figure 2.3b show that charging and discharging of NTP is facilitated primarily by FnChrysazin, since the extended charging/discharging plateaus correspond to the redox potentials of FnChrysazin. Moreso, the charge and discharge profiles of 2,7-ADS is unaffected by the change in applied current. The presence of a strong oxidative redox mediator within the electrolyte enhances the NTP oxidation via FnChrysazin. The redox potentials of FnChrysazin and 2,7-ADS are separated by over 200 mV, therefore, charge transfer from 2,7-ADS to FnChrysazin is thermodynamically unviable in cycling conditions. This result raises the question of what role 2,7-ADS plays in the system as a *spectator* species to the redox targeting reaction. We hypothesize the presence of 2,7-ADS has no direct role in interfacial charge transfer between NTP and FnChrysazin, as an intermediate charge donor/acceptor, but in fact influences the redox targeting by tuning the bulk solution potential. Once the concentration of reduced FnChrysazin is near-depleted, the bulk solution potential drifts to more positive potentials, but now the solution potential is more thermodynamically favorable to oxidize NTP and there is a high concentration of oxidized FnChrysazin to oxidize NTP. Importantly, this is the highest capacity enhancement via redox targeting demonstrated in aqueous anolytes. This is also the first report demonstrating charge inversion in aqueous anolytes, whereby the solid is responsible for most of the charge storage within the reservoir.

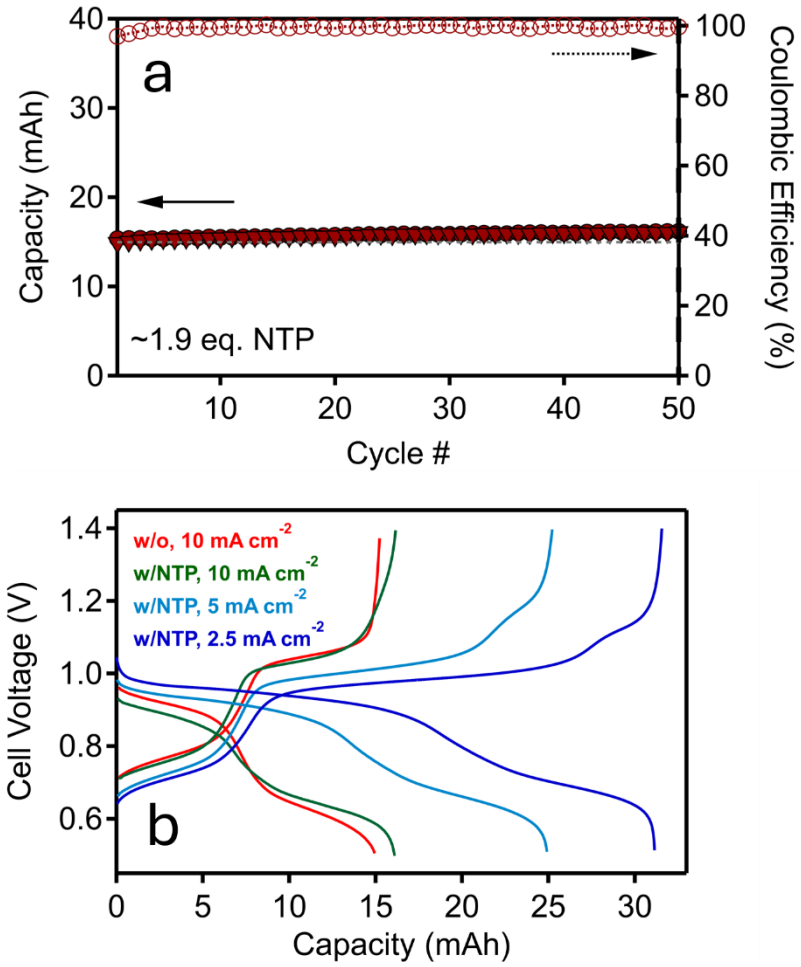

Figure 2.3 (a) Flow battery measurement of capacity (left axis, solid lines) and Coulombic efficiency (right axis, dashed lines) vs cycle number of 8 mL 25 mM each of FnChrysazin and 2,7-ADS in 1 M NaOH with ~1.9 molar equivalents (0.306 g) of NTP foam composites. The catholyte is 100 mL $Na_4[Fe(CN)_6]$ in 1 M NaOH. Charge capacity is indicated by circles, and discharge capacity is indicated by triangles. The dashed gray line represents the discharge capacity of the electrolyte alone based on prior cycling without NTP foam composite redox filter. **(b)** Voltage profiles of a single charge/discharge cycle at various current densities with the NTP foam composite redox filter. Data at lower current densities was collected subsequently after 50 cycles at 10 mA cm^{-2}.

A SSE is typically an objective for RT-RFBs because if the electrolyte and the redox-active solid have overlapping redox potentials, the energy loss is minimized and will be predominantly from cell resistance (which is unavoidable but can be minimized) and the current density. However, as demonstrated, the additional thermodynamic driving force in a DSE unlocks higher material utilization, and in turn results in a greater energy density. Figure 2.4 is a direct

comparison of the two electrolytes' performance that considers the inherent additional voltage losses from the DSE. As expected, the energy efficiency of the SSE consistently outperforms the DSE. However, both electrolytes demonstrate good energy efficiency, especially the SSE which was consistently >90% energy efficiency cycling at 5 and 2.5 mA cm^{-2}, considerably higher than mature EESs. The energy difference between the two systems is significant at 10 mA cm^{-2}, where the energy is determined predominantly by the electrolytes with a minor contribution from the redox-targeting of NTP. As lower currents are employed, more NTP participates in redox targeting, therefore, the energy of both systems increases. With our prior hypothesis, the NTP utilization is further extended in the DSE over the SSE due to the greater variance in bulk solution potential during a charge/discharge step and the increased resonance time facilitating more redox targeting. Hence, at lower currents, the increase in energy performance for DSE is greater than SSE.

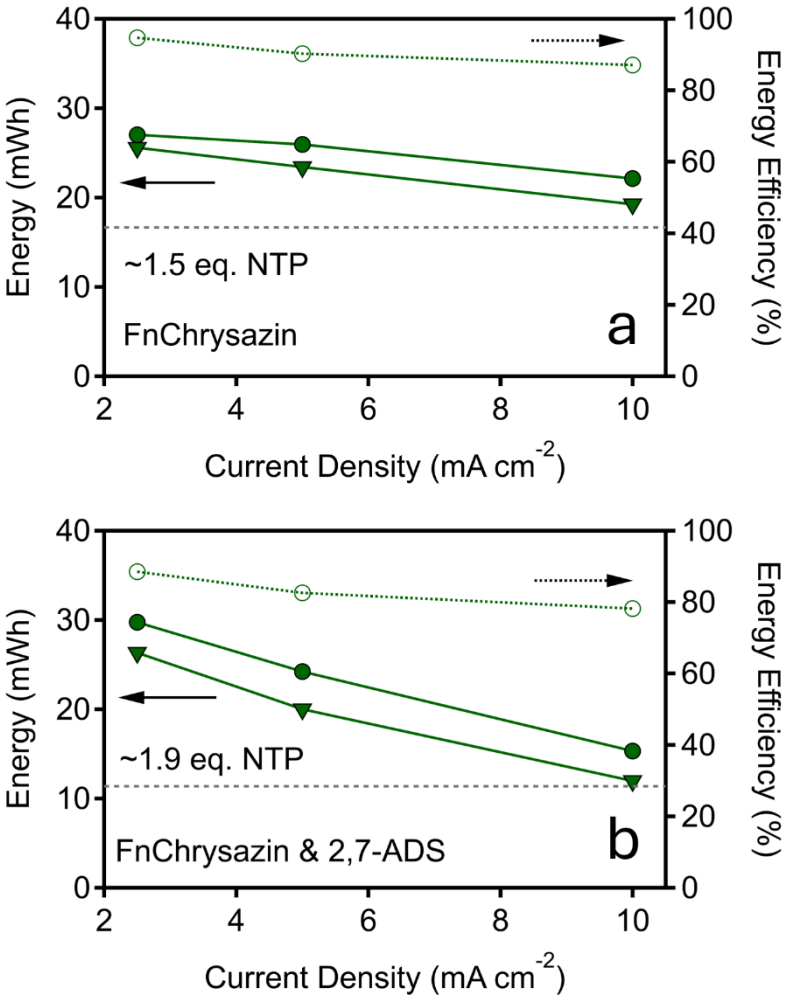

Figure 2.4 Select cycles from flow battery measurements of energy (left axis, solid lines) and energy efficiency (right axis, dashed lines) vs current density of **(a)** 8 mL 50 mM FnChrysazin in 1 M NaOH with ~1.5 molar equivalents (0.246 g) of NTP foam composites and **(b)** 8 mL 25 mM each of FnChrysazin and 2,7-ADS in 1 M NaOH with ~1.9 molar equivalents (0.306 g) of NTP foam composites. The catholyte is 100 mL $Na_4[Fe(CN)_6]$ in 1 M NaOH. Charge energy is indicated by circles, and discharge energy is indicated by triangles. The dashed gray line represents the discharge energy of the electrolyte alone based on prior cycling without NTP foam composite redox filter.

Due to the nature of producing the NTP foam composites, there is variance in the ratio of polyurethane foam, silicone caulk binder, and NTP powder, therefore, each flow battery measurement must be independently evaluated for volumetric capacity/energy density (see Appendix.A.7.2, NTP foam composites volume calculations). We note that these NTP foam composites are not volumetrically efficient with <20% of the volume consisting of NTP, however,

the principle of an immobilized 3-D porous network of NTP efficiently utilizes NTP in redox targeting reactions. Nevertheless, Figure 2.5 shows the additional volumetric capacity and energy density achieved by both electrolytes with the NTP foam composite redox filter. The volumetric capacity and energy density of the electrolytes alone were determined from the 2.5 mA cm^{-2} data shown in Figures A.21 and A.22. The volumetric capacities for FnChrysazin and FnChrysazin/2,7-ADS electrolytes are 2.15 and 2.01 Ah L^{-1}, respectively. With the addition of the NTP redox filter, the volumetric capacities for FnChrysazin and FnChrysazin/2,7-ADS electrolytes increase to 3.08 and 3.63 Ah L^{-1}, respectively. Furthermore, the energy densities for FnChrysazin and FnChrysazin/2,7-ADS electrolytes are 2.10 and 1.77 Wh L^{-1}, respectively, which increase to 2.97 and 3.07 Wh L^{-1}, respectively, with the addition of the NTP redox filter. FnChrysazin shows >40% in volumetric and energy density, whereas the FnChrysazin/2,7-ADS electrolyte displays even greater volumetric and energy density enhancements of >70%. These are the highest volumetric and energy density enhancements demonstrated in aqueous anolytes.

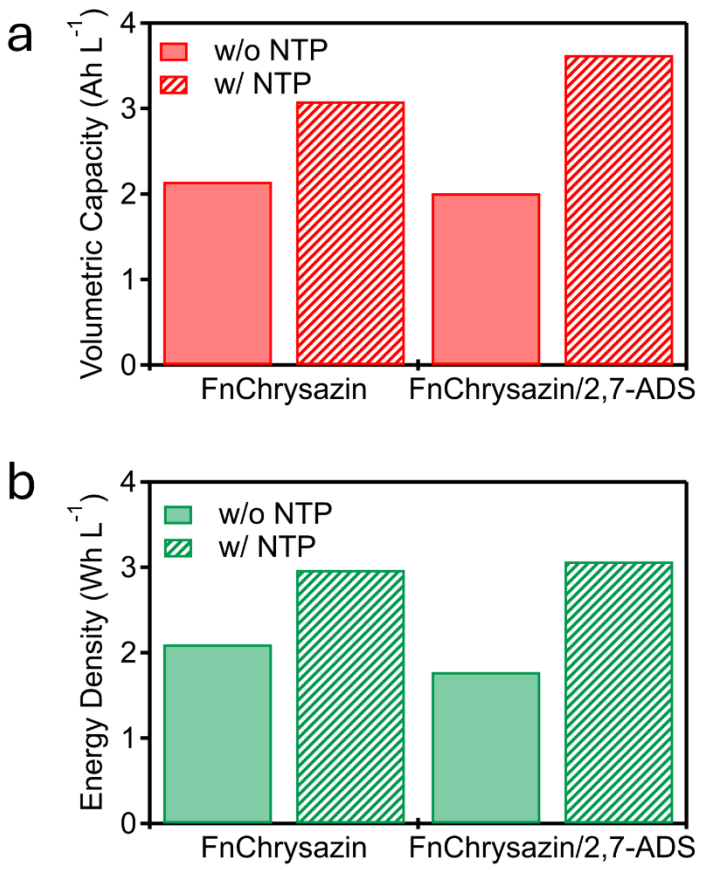

Figure 2.5 (a) The experimentally measured volumetric capacity of the FnChrysazin and FnChrysazin/2,7-ADS system without and with NTP. **(b)** The experimentally measured energy density of the FnChrysazin and FnChrysazin/2,7-ADS system without and with NTP.

Given these results, we took a theoretical approach to calculate the maximum capacities attainable with this system. While we employed relatively low electrolyte concentrations here for experimental practicality, we note that the maximum solubilities of the redox mediators are significantly higher, with FnChrysazin and 2,7-ADS solubilities as high as 1.3 and 0.74 M, respectively.[21, 60] Furthermore, we have discussed the synthesis of near-pure NTP 3-D structure (Appendix A.4.1) and demonstrated its potential in RT-RFBs (Figure A.17 & A.18a). Given that the dense 3-D NTP foam structures are durable, if we assume optimal fluid dynamics and 50% porosity (comparable to pellets porosity) the theoretical maximum volumetric capacity for the SSE and DSE electrolytes can be calculated, as highlighted by Figure 2.6. For 1.3 M FnChrysazin

(0.65 mol) and ~5.6 molar equivalents of NTP (3.65 mol), the calculated maximum volumetric capacity is 233 Ah L^{-1}. However, the flow battery observations show that not all the NTP's volume is accessible. Assuming the same 57% capacity enhancement as prior results, the theoretical maximum volumetric capacity is 97 Ah L^{-1}. The equimolar FnChrysazin/2,7-ADS electrolyte demonstrated complete NTP utilization, hence it can theoretically achieve a higher volumetric capacity because the majority of the charge is stored in the solid. The theoretical maximum volumetric capacity of equimolar 0.74 M FnChrysazin/2,7-ADS (0.37 mol) and ~9.9 equivalents NTP (3.65 mol) is therefore 131 Ah L^{-1}, based off the maximum solubility of 2,7-ADS.

Earlier we hypothesized that the NTP utilization is high with the equimolar DSE because 2,7-ADS favorably tunes the solution potential. Hence, the oxidation of NTP is not dependent on the relative concentrations of the redox shuttles. Only a small fraction of the electrolyte needs to be composed of a redox shuttle with a significantly positive (≥100 mV) redox potential relative to NTP to generate the thermodynamic driving force. A 95/5 FnChrysazin/2,7-ADS electrolyte can achieve higher solubilities than an equimolar molecular mixture and minimize voltage losses, as the electrolyte properties are dominated by FnChrysazin. The theoretical maximum volumetric capacity for 1.27 M 95/5 FnChrysazin/2,7-ADS mixture (0.64 mol) and ~5.7 equivalents NTP (3.65 mol) is 146 Ah L^{-1}. The 95/5 mixture and NTP would produce 49 Ah L^{-1} greater volumetric capacity than FnChrysazin with NTP, a significant boost achieved by activating more NTP in the redox targeting reactions. All the discussed electrolyte systems theoretically demonstrate >45% volumetric capacity than the state-of-the-art VRFB, particularly the 95/5 mixture which is 118% greater than VRFB.

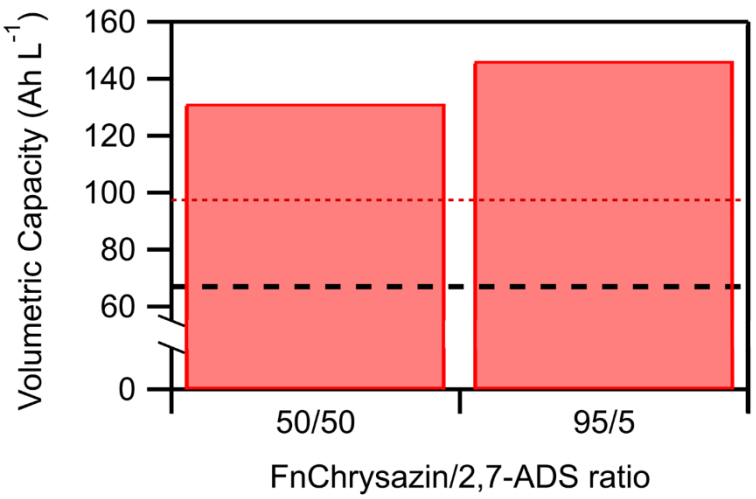

Figure 2.6 Theoretical volumetric capacity of the equimolar and 95/5 FnChrysazin/2,7-ADS electrolyte mixtures with NTP are displayed against the theoretical volumetric capacity of FnChrysazin with NTP (red dashed line) and the theoretical volumetric capacity of state-of-the-art VRFB system (2.5 M, black dashed bold line).

2.4 Summary

We demonstrate a low-cost, robust anthraquinone-based system, enhanced by a high-energy-density sodium superionic conductor $NaTi_2(PO_4)_3$ for grid-scale ESSs. An unprecedented capacity boost in aqueous anolytes via redox targeting has been achieved through novel immobilization strategies maximizing the interfacial charge transfer reactions occurring on the high-surface-area macrostructures. Furthermore, we have explored the thermodynamics and kinetics through various redox shuttles and the redox targeting resonance time to enhance the redox targeting reactions, more efficiently utilizing the redox-active solid and achieving a higher energy density. This thermodynamic mechanistic understanding of solution potential tuning via a spectator redox species is the first example in redox-targeting literature, resulting in the first demonstration of charge inversion for aqueous anolytes. An extensive 3-D NTP macrostructure facilitating good fluid dynamics for maximal interfacial charge transfer can produce a flow battery with twice the volumetric capacity of VRFB, surpassing *the* state-of-the-art flow battery technology on environmental impact, cost, and performance parameters.

2.5 References

(1) Mai; Trieu; Jadun, P.; Logan, J.; McMillan, C.; Muratori, M.; Steinberg, D.; Vimmerstedt, L.; Jones, R.; Haley, B.; et al. Electrification Futures Study: Scenarios of Electric Technology Adoption and Power Consumption for the United States. *National Renewable Energy Laboratory, Golden, CO* **2018**, *NREL/TP-6A20-71500*.

(2) Ray, S.; Gorski, A.; Cassar, C.; Yildiz, O. Electric Power Monthly May 2024. *U.S. Energy Information Administration* **2024**.

(3) Rahman, M. A.; Kim, J.-H.; Hossain, S. Recent advances of energy storage technologies for grid: A comprehensive review. *Energy Storage* **2022**, *4* (6), e322. DOI: https://doi.org/10.1002/est2.322.

(4) Gür, T. M. Review of electrical energy storage technologies, materials and systems: challenges and prospects for large-scale grid storage. *Energy & Environmental Science* **2018**, *11* (10), 2696-2767, 10.1039/C8EE01419A. DOI: 10.1039/C8EE01419A.

(5) Denholm, P.; Sun, Y.; Mai, T. An Introduction to Grid Services: Concepts, Technical Requirements, and Provision from Wind. *National Renewable Energy Laboratory, Golden, CO* **2019**.

(6) Barton, J. P.; Infield, D. G. Energy storage and its use with intermittent renewable energy. *IEEE Transactions on Energy Conversion* **2004**, *19* (2), 441-448. DOI: 10.1109/TEC.2003.822305.

(7) Faunce, T. A.; Prest, J.; Su, D.; Hearne, S. J.; Iacopi, F. On-grid batteries for large-scale energy storage: Challenges and opportunities for policy and technology. *MRS Energy & Sustainability* **2018**, *5* (1), 10. DOI: 10.1557/mre.2018.11.

(8) Ibrahim, H.; Ilinca, A.; Perron, J. Energy storage systems—Characteristics and comparisons. *Renewable and Sustainable Energy Reviews* **2008**, *12* (5), 1221-1250. DOI: https://doi.org/10.1016/j.rser.2007.01.023.

(9) Lu, N.; Weimar, M.; Makarov, Y.; Ma, J.; Viswanathan, V. V. The Wide-Area Energy Storage and Management System-Battery Storage Evaluation. *Pacific Northwest National Laboratory: Richland, WA* **2009**, *PNNL-18679*.

(10) Ding, Y.; Zhang, C.; Zhang, L.; Wei, H.; Li, Y.; Yu, G. Insights into Hydrotropic Solubilization for Hybrid Ion Redox Flow Batteries. *ACS Energy Letters* **2018**, *3* (11), 2641-2648. DOI: 10.1021/acsenergylett.8b01828.

(11) Wei, X.; Duan, W.; Huang, J.; Zhang, L.; Li, B.; Reed, D.; Xu, W.; Sprenkle, V.; Wang, W. A High-Current, Stable Nonaqueous Organic Redox Flow Battery. *ACS Energy Letters* **2016**, *1* (4), 705-711. DOI: 10.1021/acsenergylett.6b00255.

(12) Ye, J.; Xia, L.; Wu, C.; Ding, M.; Jia, C.; Wang, Q. Redox targeting-based flow batteries. *Journal of Physics D: Applied Physics* **2019**, *52* (44), 443001. DOI: 10.1088/1361-6463/ab3251.

(13) Skyllas-Kazacos, M.; Chakrabarti, M. H.; Hajimolana, S. A.; Mjalli, F. S.; Saleem, M. Progress in Flow Battery Research and Development. *Journal of The Electrochemical Society* **2011**, *158* (8), R55. DOI: 10.1149/1.3599565.

(14) Yang, Z.; Zhang, J.; Kintner-Meyer, M. C. W.; Lu, X.; Choi, D.; Lemmon, J. P.; Liu, J. Electrochemical Energy Storage for Green Grid. *Chemical Reviews* **2011**, *111* (5), 3577-3613. DOI: 10.1021/cr100290v.

(15) Dunn, B.; Kamath, H.; Tarascon, J.-M. Electrical Energy Storage for the Grid: A Battery of Choices. *Science* **2011**, *334* (6058), 928-935. DOI: doi:10.1126/science.1212741.

(16) Weber, A. Z.; Mench, M. M.; Meyers, J. P.; Ross, P. N.; Gostick, J. T.; Liu, Q. Redox flow batteries: a review. *Journal of Applied Electrochemistry* **2011**, *41* (10), 1137. DOI: 10.1007/s10800-011-0348-2.

(17) Choi, C.; Kim, S.; Kim, R.; Choi, Y.; Kim, S.; Jung, H.-y.; Yang, J. H.; Kim, H.-T. A review of vanadium electrolytes for vanadium redox flow batteries. *Renewable and Sustainable Energy Reviews* **2017**, *69*, 263-274. DOI: https://doi.org/10.1016/j.rser.2016.11.188.

(18) Cunha, Á.; Martins, J.; Rodrigues, N.; Brito, F. P. Vanadium redox flow batteries: a technology review. *International Journal of Energy Research* **2015**, *39* (7), 889-918. DOI: https://doi.org/10.1002/er.3260.

(19) Lourenssen, K.; Williams, J.; Ahmadpour, F.; Clemmer, R.; Tasnim, S. Vanadium redox flow batteries: A comprehensive review. *Journal of Energy Storage* **2019**, *25*, 100844. DOI: https://doi.org/10.1016/j.est.2019.100844.

(20) Zhang, M.; Moore, M.; Watson, J. S.; Zawodzinski, T. A.; Counce, R. M. Capital Cost Sensitivity Analysis of an All-Vanadium Redox-Flow Battery. *Journal of The Electrochemical Society* **2012**, *159* (8), A1183-A1188. DOI: 10.1149/2.041208jes.

(21) Hasan, F.; Mahanta, V.; Abdelazeez, A. A. A. Quinones for Aqueous Organic Redox Flow Battery: A Prospective on Redox Potential, Solubility, and Stability. *Advanced Materials Interfaces* **2023**, *10* (24), 2300268. DOI: https://doi.org/10.1002/admi.202300268.

(22) Kwabi, D. G.; Ji, Y.; Aziz, M. J. Electrolyte Lifetime in Aqueous Organic Redox Flow Batteries: A Critical Review. *Chemical Reviews* **2020**, *120* (14), 6467-6489. DOI: 10.1021/acs.chemrev.9b00599.

(23) Wedege, K.; Dražević, E.; Konya, D.; Bentien, A. Organic Redox Species in Aqueous Flow Batteries: Redox Potentials, Chemical Stability and Solubility. *Scientific Reports* **2016**, *6* (1), 39101. DOI: 10.1038/srep39101.

(24) Beh, E. S.; De Porcellinis, D.; Gracia, R. L.; Xia, K. T.; Gordon, R. G.; Aziz, M. J. A Neutral pH Aqueous Organic–Organometallic Redox Flow Battery with Extremely High Capacity Retention. *ACS Energy Letters* **2017**, *2* (3), 639-644. DOI: 10.1021/acsenergylett.7b00019.

(25) Lin, K.; Gómez-Bombarelli, R.; Beh, E. S.; Tong, L.; Chen, Q.; Valle, A.; Aspuru-Guzik, A.; Aziz, M. J.; Gordon, R. G. A redox-flow battery with an alloxazine-based organic electrolyte. *Nature Energy* **2016**, *1* (9), 16102. DOI: 10.1038/nenergy.2016.102.

(26) Liu, Y.; Goulet, M.-A.; Tong, L.; Liu, Y.; Ji, Y.; Wu, L.; Gordon, R. G.; Aziz, M. J.; Yang, Z.; Xu, T. A Long-Lifetime All-Organic Aqueous Flow Battery Utilizing TMAP-TEMPO Radical. *Chem* **2019**, *5* (7), 1861-1870. DOI: 10.1016/j.chempr.2019.04.021 (acccessed 2024/07/11).

(27) Cao, J.; Tao, M.; Chen, H.; Xu, J.; Chen, Z. A highly reversible anthraquinone-based anolyte for alkaline aqueous redox flow batteries. *Journal of Power Sources* **2018**, *386*, 40-46. DOI: https://doi.org/10.1016/j.jpowsour.2018.03.041.

(28) Hu, B.; Luo, J.; Hu, M.; Yuan, B.; Liu, T. L. A pH-Neutral, Metal-Free Aqueous Organic Redox Flow Battery Employing an Ammonium Anthraquinone Anolyte. *Angewandte Chemie International Edition* **2019**, *58* (46), 16629-16636. DOI: https://doi.org/10.1002/anie.201907934.

(29) Lin, K.; Chen, Q.; Gerhardt, M. R.; Tong, L.; Kim, S. B.; Eisenach, L.; Valle, A. W.; Hardee, D.; Gordon, R. G.; Aziz, M. J.; et al. Alkaline quinone flow battery. *Science* **2015**, *349* (6255), 1529-1532. DOI: doi:10.1126/science.aab3033.

(30) Park, M.; Beh, E. S.; Fell, E. M.; Jing, Y.; Kerr, E. F.; De Porcellinis, D.; Goulet, M.-A.; Ryu, J.; Wong, A. A.; Gordon, R. G.; et al. A High Voltage Aqueous Zinc–Organic Hybrid Flow Battery. *Advanced Energy Materials* **2019**, *9* (25), 1900694. DOI: https://doi.org/10.1002/aenm.201900694.

(31) Yang, Z.; Tong, L.; Tabor, D. P.; Beh, E. S.; Goulet, M.-A.; De Porcellinis, D.; Aspuru-Guzik, A.; Gordon, R. G.; Aziz, M. J. Alkaline Benzoquinone Aqueous Flow Battery for Large-Scale Storage of Electrical Energy. *Advanced Energy Materials* **2018**, *8* (8), 1702056. DOI: https://doi.org/10.1002/aenm.201702056.

(32) Hu, B.; DeBruler, C.; Rhodes, Z.; Liu, T. L. Long-Cycling Aqueous Organic Redox Flow Battery (AORFB) toward Sustainable and Safe Energy Storage. *Journal of the American Chemical Society* **2017**, *139* (3), 1207-1214. DOI: 10.1021/jacs.6b10984.

(33) Janoschka, T.; Morgenstern, S.; Hiller, H.; Friebe, C.; Wolkersdörfer, K.; Häupler, B.; Hager, M. D.; Schubert, U. S. Synthesis and characterization of TEMPO- and viologen-polymers for

water-based redox-flow batteries. *Polymer Chemistry* **2015**, *6* (45), 7801-7811, 10.1039/C5PY01602A. DOI: 10.1039/C5PY01602A.

(34) Liu, T.; Wei, X.; Nie, Z.; Sprenkle, V.; Wang, W. A Total Organic Aqueous Redox Flow Battery Employing a Low Cost and Sustainable Methyl Viologen Anolyte and 4-HO-TEMPO Catholyte. *Advanced Energy Materials* **2016**, *6* (3), 1501449. DOI: https://doi.org/10.1002/aenm.201501449.

(35) Luo, J.; Hu, B.; Debruler, C.; Liu, T. L. A π-Conjugation Extended Viologen as a Two-Electron Storage Anolyte for Total Organic Aqueous Redox Flow Batteries. *Angewandte Chemie International Edition* **2018**, *57* (1), 231-235. DOI: https://doi.org/10.1002/anie.201710517.

(36) Ahn, Y.; Moon, J.; Park, S. E.; Shin, J.; Wook Choi, J.; Kim, K. J. High-performance bifunctional electrocatalyst for iron-chromium redox flow batteries. *Chemical Engineering Journal* **2021**, *421*, 127855. DOI: https://doi.org/10.1016/j.cej.2020.127855.

(37) Wang, C.; Li, X.; Yu, B.; Wang, Y.; Yang, Z.; Wang, H.; Lin, H.; Ma, J.; Li, G.; Jin, Z. Molecular Design of Fused-Ring Phenazine Derivatives for Long-Cycling Alkaline Redox Flow Batteries. *ACS Energy Letters* **2020**, *5* (2), 411-417. DOI: 10.1021/acsenergylett.9b02676.

(38) Winsberg, J.; Stolze, C.; Muench, S.; Liedl, F.; Hager, M. D.; Schubert, U. S. TEMPO/Phenazine Combi-Molecule: A Redox-Active Material for Symmetric Aqueous Redox-Flow Batteries. *ACS Energy Letters* **2016**, *1* (5), 976-980. DOI: 10.1021/acsenergylett.6b00413.

(39) Ji, Y.; Goulet, M.-A.; Pollack, D. A.; Kwabi, D. G.; Jin, S.; De Porcellinis, D.; Kerr, E. F.; Gordon, R. G.; Aziz, M. J. A Phosphonate-Functionalized Quinone Redox Flow Battery at Near-Neutral pH with Record Capacity Retention Rate. *Advanced Energy Materials* **2019**, *9* (12), 1900039. DOI: https://doi.org/10.1002/aenm.201900039.

(40) Kwabi, D. G.; Lin, K.; Ji, Y.; Kerr, E. F.; Goulet, M.-A.; De Porcellinis, D.; Tabor, D. P.; Pollack, D. A.; Aspuru-Guzik, A.; Gordon, R. G.; et al. Alkaline Quinone Flow Battery with Long

Lifetime at pH 12. *Joule* **2018**, *2* (9), 1894-1906. DOI: https://doi.org/10.1016/j.joule.2018.07.005.

(41) Wu, M.; Jing, Y.; Wong, A. A.; Fell, E. M.; Jin, S.; Tang, Z.; Gordon, R. G.; Aziz, M. J. Extremely Stable Anthraquinone Negolytes Synthesized from Common Precursors. *Chem* **2020**, *6* (6), 1432-1442. DOI: https://doi.org/10.1016/j.chempr.2020.03.021.

(42) Pang, S.; Wang, X.; Wang, P.; Ji, Y. Biomimetic Amino Acid Functionalized Phenazine Flow Batteries with Long Lifetime at Near-Neutral pH. *Angewandte Chemie International Edition* **2021**, *60* (10), 5289-5298. DOI: https://doi.org/10.1002/anie.202014610.

(43) Jin, S.; Fell, E. M.; Vina-Lopez, L.; Jing, Y.; Michalak, P. W.; Gordon, R. G.; Aziz, M. J. Near Neutral pH Redox Flow Battery with Low Permeability and Long-Lifetime Phosphonated Viologen Active Species. *Advanced Energy Materials* **2020**, *10* (20), 2000100. DOI: https://doi.org/10.1002/aenm.202000100.

(44) Liu, W.; Liu, Y.; Zhang, H.; Xie, C.; Shi, L.; Zhou, Y.-G.; Li, X. A highly stable neutral viologen/bromine aqueous flow battery with high energy and power density. *Chemical Communications* **2019**, *55* (33), 4801-4804, 10.1039/C9CC00840C. DOI: 10.1039/C9CC00840C.

(45) Jin, S.; Jing, Y.; Kwabi, D. G.; Ji, Y.; Tong, L.; De Porcellinis, D.; Goulet, M.-A.; Pollack, D. A.; Gordon, R. G.; Aziz, M. J. A Water-Miscible Quinone Flow Battery with High Volumetric Capacity and Energy Density. *ACS Energy Letters* **2019**, *4* (6), 1342-1348. DOI: 10.1021/acsenergylett.9b00739.

(46) Coffman, R. E.; Kildsig, D. O. Effect of Nicotinamide and Urea on the Solubility of Riboflavin in Various Solvents. *Journal of Pharmaceutical Sciences* **1996**, *85* (9), 951-954. DOI: https://doi.org/10.1021/js960012b.

(47) Wang, Q.; Zakeeruddin, S. M.; Wang, D.; Exnar, I.; Grätzel, M. Redox Targeting of Insulating Electrode Materials: A New Approach to High-Energy-Density Batteries. *Angewandte*

Chemie International Edition **2006**, *45* (48), 8197-8200. DOI: https://doi.org/10.1002/anie.200602891.

(48) Cheng, Y.; Wang, X.; Huang, S.; Samarakoon, W.; Xi, S.; Ji, Y.; Zhang, H.; Zhang, F.; Du, Y.; Feng, Z.; et al. Redox Targeting-Based Vanadium Redox-Flow Battery. *ACS Energy Letters* **2019**, *4* (12), 3028-3035. DOI: 10.1021/acsenergylett.9b01939.

(49) Yu, J.; Fan, L.; Yan, R.; Zhou, M.; Wang, Q. Redox Targeting-Based Aqueous Redox Flow Lithium Battery. *ACS Energy Letters* **2018**, *3* (10), 2314-2320. DOI: 10.1021/acsenergylett.8b01420.

(50) Chen, Y.; Zhou, M.; Xia, Y.; Wang, X.; Liu, Y.; Yao, Y.; Zhang, H.; Li, Y.; Lu, S.; Qin, W.; et al. A Stable and High-Capacity Redox Targeting-Based Electrolyte for Aqueous Flow Batteries. *Joule* **2019**, *3* (9), 2255-2267. DOI: https://doi.org/10.1016/j.joule.2019.06.007.

(51) Yang, G.; Song, H.; Wu, M.; Wang, C. Porous NaTi2(PO4)3 nanocubes: a high-rate nonaqueous sodium anode material with more than 10 000 cycle life. *Journal of Materials Chemistry A* **2015**, *3* (36), 18718-18726, 10.1039/C5TA04491J. DOI: 10.1039/C5TA04491J.

(52) Moghaddam, M.; Sepp, S.; Wiberg, C.; Bertei, A.; Rucci, A.; Peljo, P. Thermodynamics, Charge Transfer and Practical Considerations of Solid Boosters in Redox Flow Batteries. *Molecules* **2021**, *26* (8), 2111.

(53) Wu, M.; Ni, W.; Hu, J.; Ma, J. NASICON-Structured $NaTi_2(PO_4)_3$ for Sustainable Energy Storage. *Nano-Micro Lett.* **2019**, *11:44* (1), 1-36. DOI: 10.1007/s40820-019-0273-1.

(54) Pang, G.; Yuan, C.; Nie, P.; Ding, B.; Zhu, J.; Zhang, X. Synthesis of NASICON-Type Structured $NaTi_2(PO_4)_3$-Graphene Nanocomposite as an Anode for Aqueous Rechargeable Na-Ion Batteries. *Nanoscale* **2014**, *6* (12), 6328-6334. DOI: 10.1039/c3nr06730k.

(55) Yang, J.; Wang, H.; Hu, P.; Qi, J.; Guo, L.; Wang, L. A High-Rate and Ultralong-Life Sodium-Ion Battery Based on NaTi2(PO4)3 Nanocubes with Synergistic Coating of Carbon and Rutile TiO2. *Small* **2015**, *11* (31), 3744-3749. DOI: https://doi.org/10.1002/smll.201500144.

(56) Mohamed, A. I.; Whitacre, J. F. Capacity Fade of NaTi2(PO4)3 in Aqueous Electrolyte Solutions: Relating pH Increases to Long Term Stability. *Electrochimica Acta* **2017**, *235*, 730-739. DOI: https://doi.org/10.1016/j.electacta.2017.03.106.

(57) Arroyo-Currás, N.; Hall, J. W.; Dick, J. E.; Jones, R. A.; Bard, A. J. An Alkaline Flow Battery Based on the Coordination Chemistry of Iron and Cobalt. *J. Electrochem. Soc.* **2014**, *162* (3), A378-A383. DOI: 10.1149/2.0461503jes.

(58) Gong, K.; Xu, F.; Grunewald, J. B.; Ma, X.; Zhao, Y.; Gu, S.; Yan, Y. All-Soluble All-Iron Aqueous Redox-Flow Battery. *ACS Energy Letters* **2016**, *1* (1), 89-93. DOI: 10.1021/acsenergylett.6b00049.

(59) Noh, C.; Chung, Y.; Kwon, Y. Organometallic Redox Flow Batteries Using Iron Triethanolamine and Cobalt Triethanolamine Complexes. *J. Power Sources* **2020**, *466*, 228333. DOI: 10.1016/j.jpowsour.2020.228333.

(60) Wu, M.; Bahari, M.; Fell, E. M.; Gordon, R. G.; Aziz, M. J. High-performance anthraquinone with potentially low cost for aqueous redox flow batteries. *Journal of Materials Chemistry A* **2021**, *9* (47), 26709-26716, 10.1039/D1TA08900E. DOI: 10.1039/D1TA08900E.

Chapter 3. Spectroelectrochemical Revelations of Prussian Blue Redox Targeting Reaction Kinetics

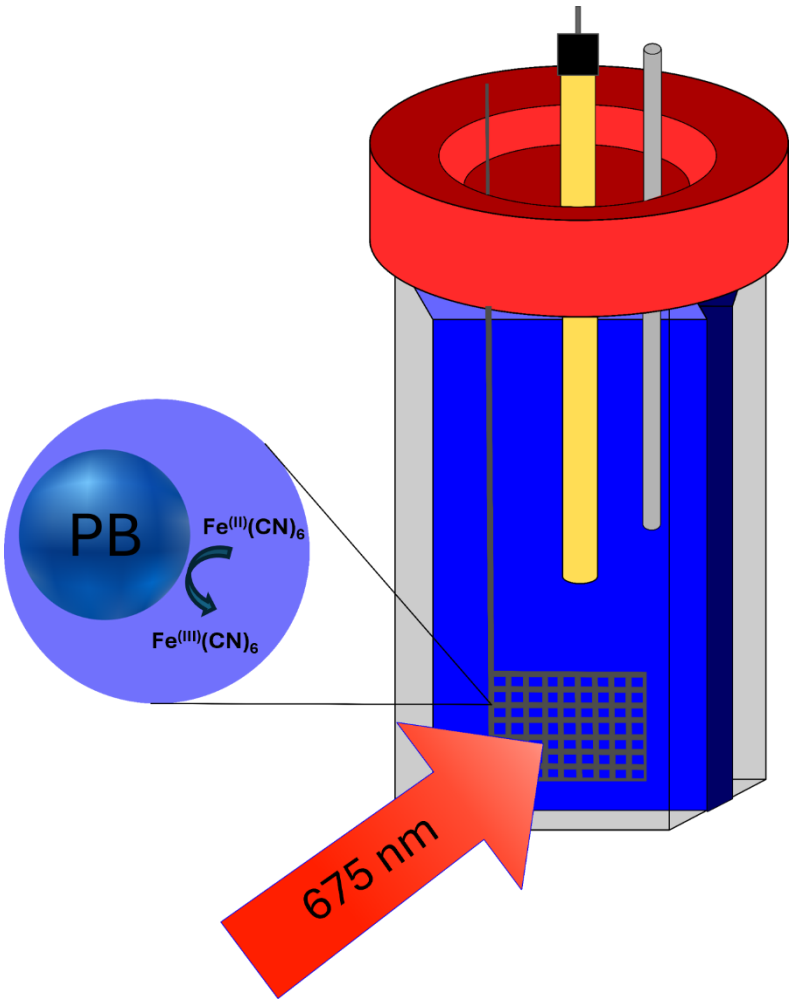

3.1 Overview

Understanding the interfacial charge transfer kinetics is crucial knowledge in the choice of redox-active solids for energy storage applications. Here, we use spectroelectrochemistry to probe a prevalent redox-targeting mechanism in literature, Prussian blue and ferricyanide. Mechanistic insights are revealed via *in situ* absorbance measurements that would otherwise not be possible through purely electrochemical methods alone. Real-time charging kinetics are monitored throughout a charge-discharge cycle through absorbance changes as Prussian blue nanocrystals transform to Prussian white. The redox-targeting mechanism demonstrates charging phases, whereby the charging rate fluctuates throughout a charge cycle. Altering the

supporting electrolyte dramatically impacts the charging profile with a higher propensity for intercalants that greater stabilizes the Prussian white transformation.

3.2 Introduction

Energy storage systems (ESSs) are the focus of recent efforts to decarbonize the grid as we are pivoting from fossil fuel generation towards renewable energy.[1-6] Redox flow batteries (RFBs) are envisioned as a long-duration discharge solution for the grid because they possess many benefits, including flexible time, quick response time, long service lifespan, inherently safe, and decouples power and energy making the technology scalable.[3, 7-10] Recently, RFBs have employed energy-dense redox-active solids as a solution to surpass the volumetric capacity pinned by the solubility limit of the redox-active species.[7, 11-13] These solids remain in the electrolyte reservoir tank and underdo redox reactions with the liquid electrolyte, known as redox targeting, therefore, circumvent this chemical barrier to achieve high-energy-density RFBs. Typically, these solids are poorly conducting materials that require conductive additives for electrochemical applications, however, within the electrolyte reservoirs, these materials are immersed by the electrolyte, and it has been demonstrated to efficiently redox target with the native material. An advantage of RFBs is quick response times, however, it is also vital that ESSs can output power that matches demand to be viable solution to cope with the intermittency of renewables. Therefore, it is valuable to investigate the kinetics of redox targeting reactions to scrutinize the viability of redox targeting RFBs vs conventional RFBs. Redox-active solids with fast redox reaction kinetics are promising additives for high-energy, high-power RFBs. However, slow kinetics could be detrimental if material utilization is poor, consuming volume that could otherwise be occupied by the liquid electrolyte. The peak power output of RFBs depends on the electrolyte redox reaction kinetics, electrolyte flow rate, and the internal resistances (i.e. ion-

exchange membrane, electrolyte conductivity). In addition to these, redox-targeting RFBs (RT-RFBs) must factor in the interfacial charge transfer kinetics within the reservoir tanks.

Prussian blue (PB)[14] and Prussian blue analogues (PBAs)[15, 16] have garnered a lot of attention as redox-targeting solids with many reports demonstrating improved volumetric capacity and achieving high energy density systems. Most notably, the $K_3[Fe(CN)_6]$/PB system demonstrated a 3-fold volumetric capacity increase of the catholyte.[12] PB consists of iron centers with cyanide linkers between each pair of iron centers, this results in an open channel structure. In PB, half of the iron centers are in the reduced divalent state, whereas the other half are in the oxidized trivalent state. These trivalent iron centers can be reduced, hence, the lattice stores charge with the injected electrons localized at the iron centers. The reduction event of PB generates Prussian white (PW) and the redox reaction can be described by equation 3.1:

$$A Fe^{(II)}[Fe^{(III)}(CN)_6] + A^+ + e^- \underset{\text{discharge}}{\overset{\text{charge}}{\rightleftharpoons}} A_2 Fe^{(II)}[Fe^{(II)}(CN)_6] \qquad (3.1)$$

The electron injection is accompanied by intercalation of a cation, which maintains charge neutrality and stabilizes the lattice. The intercalation charging mechanism is possible because of the open channel lattice of PB.

There are literature examples investigating the ion intercalation upon charging in PB, however, these studies tend to overestimate the ionic diffusion kinetics.[17-24] Commonly, the PB is deposited directly onto the electrode (via electrodeposition) as a film and the diffusion length is regarded as the film depth. This overlooks the polycrystallinity of films, composed of small grain domains and grain boundaries. Ionic diffusion is slow within the domains but orders of magnitude faster along the grain boundaries.

There are limited studies investigating redox-targeting kinetics with only two such reports from the Wang group.[25, 26] Both of these reports investigate the ferrocene–$LiFe(PO_4)_3$ redox targeting system, however, neither experimental setup is truly representative of a RT-RFB and

assumptions are invoked for the diffusion lengths that are not representative of the ionic diffusion within single domains.

Herein, we investigate colloidal PB nanocrystals immersed in $K_3[Fe(CN)_6]$ electrolyte. The effect of supporting electrolyte on redox targeting kinetics is examined. We employ potentiometric intermittent titration technique (PITT) with *in situ* absorbance measurements for real-time data collection of the current response and absorption changes simultaneously. PITT is an established electrochemical probe for diffusion kinetics, commonly used to investigate Li^+ diffusion kinetics of electrode materials for Li-ion batteries. Furthermore, it is a clean method for electron injection/extraction vs chemical reductants/oxidants as it mitigates the potential for any side reactions and avoids introducing cation species that may interfere with the intercalation kinetics. Absorption has only garnered attention for probing the relative concentrations of reduced vs oxidized redox mediators and is overlooked as a diffusion processes probe.

3.3 Theory

Utilizing pseudo-spherical 15.5 nm PB nanocrystals, we consider a 1-D diffusion model of the intercalation species from the surface towards the core. Furthermore, by utilizing colloidal PB nanocrystals, the diffusion length is equal to the radius of the nanoparticle ensemble. Carrying the measurements in a 2 mm path-length cuvette restricts the electrolyte flow, in effect having the PB nanocrystals "frozen" in solution. We assume this because nanocrystals possess slow diffusion kinetics, orders of magnitude lower than the redox mediators. For this system, ferricyanide demonstrates ~10^4 faster diffusion kinetics.[27] Therefore, this system experimentally simulates the redox chemistries observed in a redox-targeting redox flow battery. The redox mediator undergoes charge transfer at the electrode and within the electrolyte reservoir upon the

surface of the redox-active solid medium, rather than direct charging of the redox-active solid by charge injection at the electrode.

Initially, the system will be completely discharged, with charging occurring with a negative applied potential with respect to the open circuit potential (OCP) that will inject electrons into the redox mediator, and these will diffuse and charge the PB nanocrystals as described by equation 3.2:

$$PB + [Fe^{(II)}(CN)_6] + A^+ \underset{\text{discharge}}{\overset{\text{charge}}{\rightleftharpoons}} PW + [Fe^{(III)}(CN)_6] \qquad (3.2)$$

In the PITT experiment, the potential is controlled while the current response is measured. Assuming 1-D transport for the chemical diffusion process in the redox reaction of PB (eq. 3.2), the time dependence of the transient current difference between an electrolyte without and with PB is described by equation 3.3:[28]

$$i_{PB}(t)-i_{RM}(t)= \frac{2z_AFS(C_s-C_o)D_0}{L} exp\left(-\frac{\pi^2 D_0 t}{4L^2}\right) \qquad \text{when } t >> L^2/D_0 \qquad (3.3)$$

Where F is Faraday's constant, S is the surface area of the electrode, (C_s-C_o) is the concentration difference at the surface at time t and at the beginning of the potential pulse, D_0 is the ionic diffusion coefficient, and L is the diffusion length. The diffusion coefficient, D_0, is related to the log natural (ln) of the current, Δi, against time resulting from the potential pulse, as described by equation 3.4:[28]

$$D_0= \frac{d\ ln(\Delta i/A)}{dt}\ \frac{4L^2}{\pi^2} \qquad (3.4)$$

Tracking the absorption variation is a direct probe of the transformation of PB to PW during a charge period with the absorption feature at 675 nm decaying with charging. The relative reduction in the 675 nm absorption is proportional to the ratio of PB to PW, hence, the change of

SOC can also be determined. We note that we deem the system fully charged once the normalized absorption change is <0.05 for 30 seconds. The ionic diffusion kinetics are related to the rate of PB to PW transformation, therefore, the ionic diffusion coefficient can be calculated as described by equation 3.5:[29, 30]

$$D_0 = \frac{L^2}{2\tau} \tag{3.5}$$

Where τ is the time. For the calculation of the ionic diffusion coefficient, ≥95% of the change in absorption data during the PB charge/discharge regions is used to determine the diffusion length as described by equation 3.6:

$$L = r \times \frac{\Delta A_\tau}{1 - A_{min}} \tag{3.6}$$

Where r is the PB nanocrystal radius, ΔA_τ is the change in absorption within time τ, and A_{min} is the absorption minimum achieved at full charge.

3.4 Results and discussion

PITT experiments were initially conducted with an all potassium-based system, employing potassium ferricyanide as the redox mediator and KCl as the supporting electrolyte. The total K^+ concentration was 0.05 M. From the OCP of the discharged system, the potential was stepped to negative potentials to charge inject. The system was stepped hundreds of millivolts in total during the charge and an equal amount to more positive potentials to subsequently discharge the system.

Figure 3.1a shows the change in absorption against time for PB with various concentrations of potassium ferricyanide, where molar equivalents are equivalent of ferricyanide relative to PB iron centers. This redox mediator concentration series shows that the charging rates

of PB can vary significantly depending on the molar equivalents of ferricyanide. PB does show limited charging in the absence of ferricyanide, however, the initial charging rate diminishes with time. A fraction of the PB nanocrystal population will be in close proximity to the WE, therefore, can undergo charge transfer directly. However, the stationary nanocrystals prevent the whole nanocrystal surface from engaging in direct charge transfer with the WE. Charge transfer occurs at a limited region upon the nanocrystal surface, the surface region closest to the WE. Therefore, electrons and cations must diffuse from this small surface region, throughout the lattice, which inherently is a slower process than surface charging. Furthermore, not all nanocrystals are in close proximity to the WE, thus will not charge. Repeating the experiment but with the addition of ~0.01 molar equivalents of ferricyanide has a huge impact on the charging rate, with the rate doubling. Higher concentrations of ferricyanide (≥1 molar equivalents) exhibit different charging profiles compared to low ferricyanide concentrations, whereby the rate of charging appears to be similar and sustained throughout the charging period. A difference between these higher ferricyanide concentrations is that with increasing concentrations, there is a delay from the initial charging pulse to when the PB nanocrystals begin the charge. This is because the more mobile ferricyanide species dominates the initial interfacial charge transfer reactions with the high frequency of collisions. The PB nanocrystals state-of-charge (SOC) during this period remain constant because the reduction and oxidation reactions upon the surface are occurring at the same rate. Therefore, the majority of the redox mediator concentration must first be in the reduced state before subsequent charging of the PB nanocrystals occurs. This has been observed by Lee *et al.*[31] where they observed in a system with matching electrolyte and solid redox potentials that redox targeting only occurred when 55% of the electrolyte was in the discharged state before being reduced by the solid. Ultimately, the rise of these slopes in Figure 3.1b at higher concentrations of ferricyanide are near identical, therefore, the subsequent data was collected using 5 molar equivalent of ferricyanide.

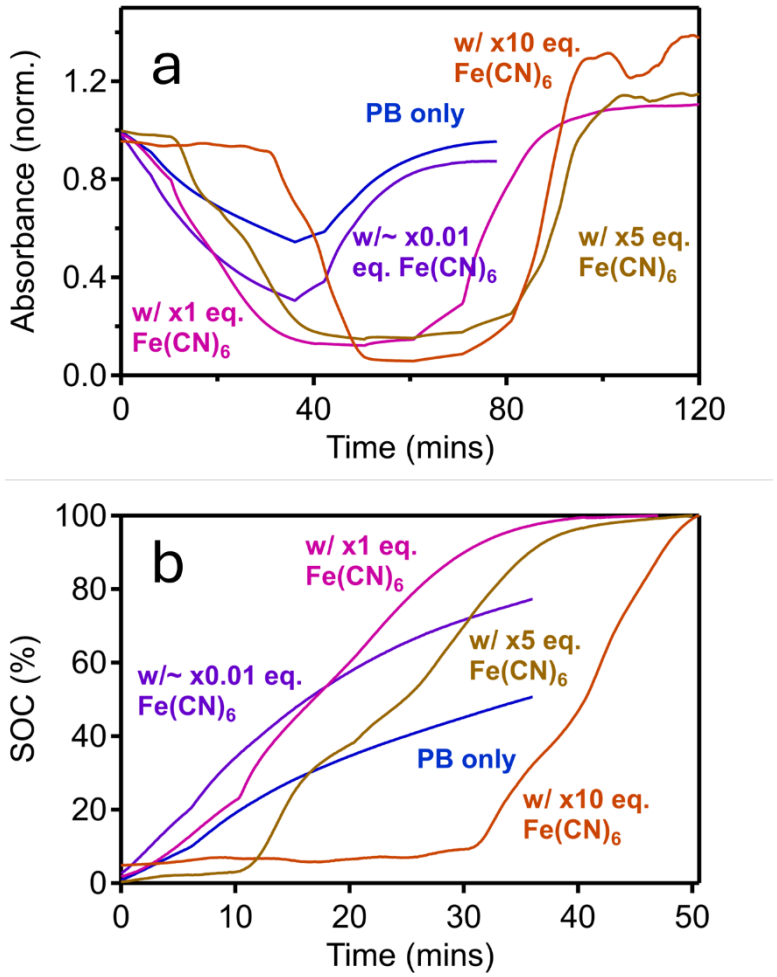

Figure 3.1 (a) Absorption change vs time for the PB nanocrystals without and with varying equivalent of ferricyanide. Absorption traces have been offset for time = 0 to represent the first -50 mV charging pulse, rather than the initial open circuit potential step. The supporting electrolyte was 0.05 M [K^+] for each potassium ferricyanide loading, adjusting the KCl supporting electrolyte salt accordingly. **(b)** State-of-charge vs time plot displaying the variance in charging rates of PB nanocrystals with increasing equivalents of ferricyanide. Traces have been offset time = 0 to represent the first -50 mV charging pulse.

Concurrently, PITT measurements were collected and employed pulse times that were significantly longer than the rest periods. Therefore, the relative concentration of reduced vs oxidized will be maintained as $[Fe^{(II)}(CN)_6]_{PB} > [Fe^{(III)}(CN)_6]_{PB}$ throughout the charging period and vice versa for the discharging period. Figure 3.2a shows the current response from the corresponding potential step with it exhibiting a Cottrell-like decay feature. This is expected from a system that is initially equilibrating from the electrical double layer at the WE. However, more

charge is injected into the electrolyte at the earlier time during a pulse when $[Fe^{(III)}(CN)_6]_{WE}$ is greater. This charge then propagates through the electrolyte via ferrocyanide diffusion and by charge-transfer collisions with ferricyanide, eventually undergoing redox reactions with PB upon the nanocrystals surface. The ferricyanide concentration is dependent on the redox targeting kinetics because this is the source of ferricyanide regeneration in the proximity of the WE. With the pulse duration, the current response continues to decay with the reduced available PB volume and rising $[Fe^{(II)}(CN)_6]_{WE}$. Due to the high mobility of ferro-/ferricyanide, the current response associated with ferrocyanide mixing with the bulk solution away from the WE was subtracted. The PITT experiment was repeated with ferricyanide alone to baseline the current response as is included in equation 3.3.

Figure 3.2b shows the ln of the current response exclusively associated with the PB nanocrystals and with a linear regression fitting (red trace) to extract the potassium ionic diffusion coefficient (D_{K^+}) via equation 3.4.

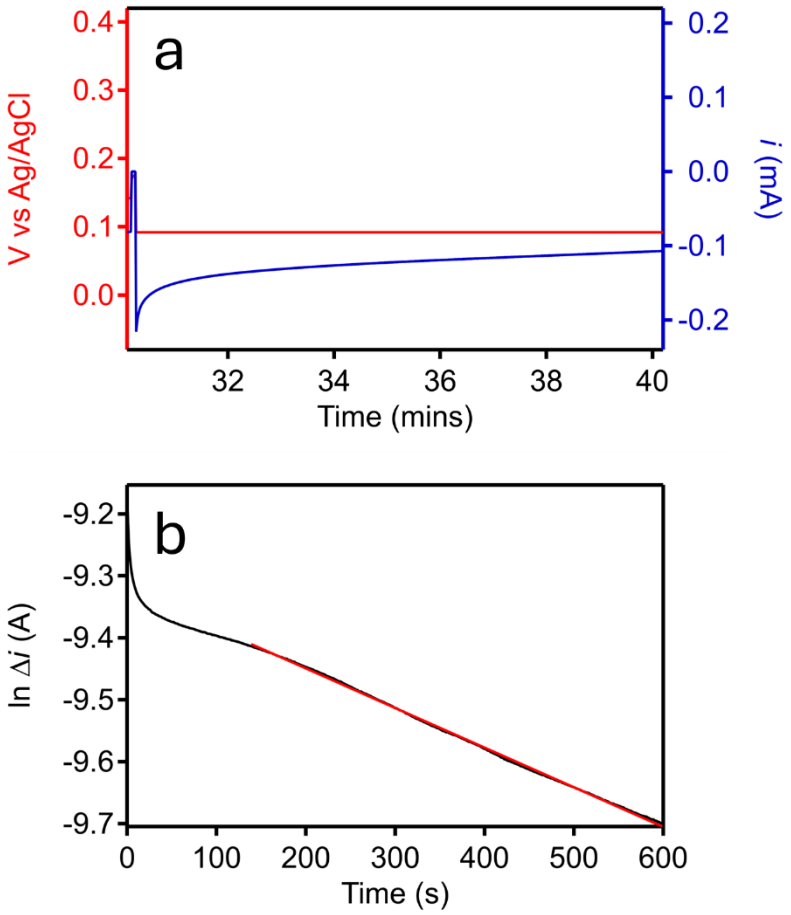

Figure 3.2 (a) The measured current response (blue trace, right axis) associated with the applied potential step (red trace, left axis). The [K^+] is 0.05 M. **(b)** The ln PB current response against time (black trace) with a linear regression fitting (red trace) to the linear tail to extract the potassium ionic diffusion coefficient.

Table 1 displays the potassium ionic diffusion coefficient values from the analysis of the absorption and PITT electrochemical data. These are remarkably similar, validating the spectrochemical approach described herein. Therefore, the subsequent data will determine ionic diffusion coefficients via absorption data exclusively.

Table 3.1 D_{K^+} values as determined from absorption and PITT data.

	Absorbance	*PITT*
D_{K^+} *(cm² s⁻¹)*	1.45 x 10^{-16} ± 0.24	1.54 x 10^{-16} ± 0.06

Supporting electrolyte concentration impacts the solution conductivity, at high salt concentrations, the mobility of redox-active species and free ions are their highest, thus, can achieve high electron injection/extraction fluxes. The ionic diffusion coefficient is independent of supporting electrolyte concentrations, however, repeating the measurement at a different supporting electrolyte concentration can validate the extracted D_{K^+} values prior. To maintain colloidally stable PB nanocrystals, the supporting electrolyte concentration was reduced so the [K^+] was halved to 0.025 M. Figure 3.3a shows that the decreased solution conductivity increases the PB charging time onset. This is due to slower ferricyanide charging at the electrode, which increases the charging time of ferricyanide before the concentration of ferrocyanide is high enough to redox target with the PB nanocrystals. Regardless, the change in absorption during the charge and discharge regions is similar at K^+ concentrations of 0.025 and 0.05 M. The 0.025 M K^+ absorption data yields a D_{K^+} of 1.41 x 10^{-16} cm^2 s^{-1}, a difference of 0.03 x 10^{-16}. Figure 3.3b translates the derivative of the absorption slopes within the charging region for both K^+ concentrations, highlighting the nuanced fluctuations. The C-rate, a measure of the charging rate, can be extracted from the derivative of the absorption curve to reveal fluctuations in the C-rate during charging/discharging. Figure 3.3b reveals there are three distinct charging regions during K^+ intercalation, independent of the supporting electrolyte concentration. There is the initial steady rise in the C-rate for both systems, followed by a drop approaching the 40% SOC, a brief spike in the C-rate follows and then another gradual rise which eventually curtails as the system approaches full charge. Interestingly, the C-rate drop off for 0.025 M K^+ begins at a 10% higher SOC than the 0.05 M K^+ system after the first C-rate rise period. For the second rise period, the drop off occurs at 80% SOC for both [K^+] systems. Furthermore, the 0.025 M K^+ exhibits more stable charging than the 0.05 M K^+, with the C-rate centered around 2 with minimal deviation between the 20 and 80% SOC. On the other hand, the 0.05 M K^+ system swings between a C-rate of 3 and 1 within the same 20 to 80% SOC region. However, the second rise period maximum

demonstrates a 20% SOC window where a stable C-rate is achieved and is a similar C-rate value to the 0.025 M K^+ system.

Upon first glance, it appears that a higher K^+ concentration facilitates faster charging. This is true in the two rise regions, the first exhibiting a C-rate that is ~50% greater and the second showing a marginally greater C-rate. Ultimately, these C-rate differences are minor fluctuations in the rate of charging, as we know from Figure 3.3a that the charge times are near identical. It is important to remember that by employing these 15.5 nm colloidal nanocrystals, the surface area to volume ratio is high, certainly much higher than traditional kinetic studies that produce films or compressed layers which are in direct contact with the WE. We hypothesize that the initial rise in C-rate stems from the reduction of iron centers at the nanocrystal surface. It is clearly evident from the 0.05 M K^+ data, that the C-rate reaches a maximum at 20% SOC and drops off to a minimum at 40%. As we know the ensemble particle size, we can calculate the number of unit cells present upon the nanocrystal surface. We note that the particles are pseudo-spherical, therefore, have a greater surface area to volume ratio than uniform spheres. However, this is counteracted by the simplified calculation for determining the number of unit cells present for a uniform sphere (see Appendix B. for calculations) which is an overestimate, as it ignores surface faceting. Based off a 7.75 nm radius for the PB nanocrystals we calculated 736 out of 1876 unit cells are at the surface of each nanocrystal, this is nearly 40% of the unit cells with *easily accessible* iron centers. This would correlate with the maximum at 20% SOC as this is the point where all the available surface iron centers – half of trivalent iron centers present in the surface unit cells – are now in the divalent state, therefore the C-rate fades beyond this maximum with the depleted surface trivalent iron center population. These surface iron centers are the first to reduce because at the interface these can be stabilized by solvated cations within the electrolyte. Beyond these surface reduction sites, the intercalant will need to desolvate prior to intercalation to facilitate charging of the core trivalent iron centers. The brief C-rate spike centered around 45% SOC is the result of a potential step occurring at that stage of charging, but the C-rate equilibrium

is quickly reestablished. The second C-rate rise is due to the diffusion of electrons and cations towards the core, as driven by the ever-increasing negative solution potential. This core diffusion regenerates trivalent iron centers at the surface, which can accept more electrons from ferrocyanide and be quickly stabilized by electrolyte cations. This increasing C-rate trend is maintained until ~60% SOC. After this, the equilibrium of ionic diffusion to the core and the available surface site, which influences the C-rate, exhibits a similar trend to the 0.025 M K^+ system as the particles approach charge saturation.

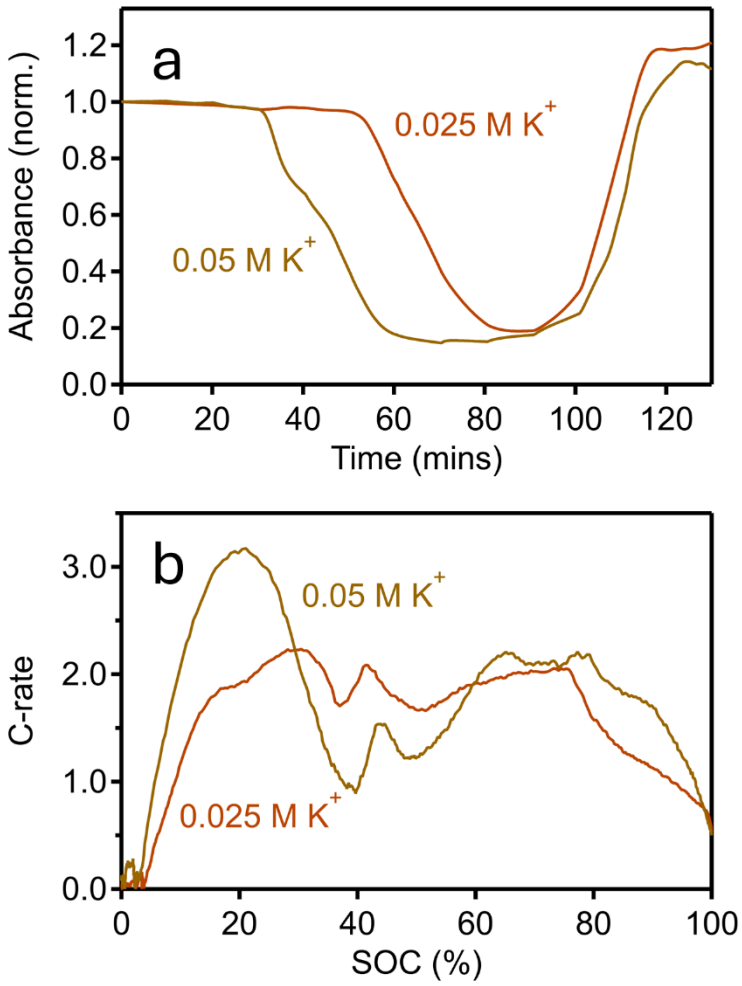

Figure 3.3 (a) Change in absorption vs time during a charge/discharge cycle at 0.05 and 0.025 M K^+ supporting electrolyte concentrations. Potassium ferricyanide would contribute 9 mM K^+ concentration, with the remaining 0.41 and 0.16 M A^+ compensated by KCl supporting electrolyte salt for 0.05 and 0.025 M A^+ electrolytes, respectively. **(b)** The C-rate vs SOC as determined from the charging region data in panel (a) for 0.05 and 0.025 M K^+ supporting electrolyte concentrations. A boxcar average has been applied to the real-time C-rate data for data smoothing, with the data representing the average C-rate per minute of data points.

Next, we explore the role of the supporting electrolytes on the charging behavior of the PB nanocrystals. PB has already been demonstrated to charge/discharge with a variety of cations including mono-, di-, and tri-valent cations.[15, 32-34] The work conducted by Phadke *et al.*[35] investigates the electrochemical properties and performance of PB with supporting electrolyte

of alkali metal salts, revealing with cyclic voltammograms (CVs) that the reversibility and redox potential is dependent on the intercalant species.

Figure 3.4a shows the absorption differences between different supporting electrolyte systems during a charge/discharge cycle. The K^+- and NH_4^+-based electrolytes exhibit near identical absorption profiles. However, the Na^+-based electrolyte demonstrates a longer dwell period before PB charging occurs. The following charging kinetics are slower as evident by the more gradual change in absorption with time under a negative charging potential. This agrees with Phadke *et al.*[35] whereby the redox potential is shifted to more negative potentials as the initial potential step is determined by the OCP of potassium ferricyanide – similar across all experiments. Furthermore, Na^+ insertion into PB generates quasi-reversible CV waves, indicating worse electrochemical performance, including sluggish kinetics.[19, 23] However, the charge vs discharge times are dramatically different in the Na^+-based electrolyte. This implies poor stabilization energy with Na^+ intercalation into the charged lattice. On the other hand, the discharge kinetics are comparable to the K^+ and NH_4^+ systems, ruling out slow Na^+ mobility within the lattice. The K^+- and NH_4^+-based electrolytes reveal a more balanced charge/discharge profile, implying the larger ionic radii intercalant better stabilize the charged lattice.

Figure B.3 extends the supporting electrolyte identity to include the remaining alkali metal elements, including lithium, a prevalent material in batteries and energy storage systems. For Li^+-based electrolyte, the absorption profile over a charge/discharge cycle shows similarities with the K^+-based electrolyte. At first, this appeared to deviate from the understanding that smaller ionic radii cations provide less lattice stabilization. However, due to the K^+ charging signature and that we know a small concentration of K^+ is in solution from the potassium ferricyanide redox mediator salt, a control experiment would identify the intercalating species. A repeat of the experiment with the redox mediator and no additional supporting electrolyte revealed that fully charging/discharging PB is possible at ultra-low K^+ concentrations with near identical

charging/discharging behavior to higher [K^+] electrolytes. From this, we can rule out any significant Li^+ insertion into PB upon charging and that Li^+ is outcompeted by the minority cation species in solution, K^+, therefore no Li^+ insertion/extraction kinetics can be interpreted from the data. Rb^+- and Cs^+-based electrolytes were also investigated, however, both of these electrolytes lacked the reversibility of the other electrolytes with visible precipitation of the nanocrystal population within the spectrochemical cell. Both electrolytes charge at higher potentials, as we expect from the larger ionic radii, but interestingly the data suggests they charge at a slower rate than K^+-based electrolyte. It cannot be ruled out that the absorption decrease is a combination of charging and nanocrystal decomposition with the larger ionic radii of Rb^+ (1.64 Å) and Cs^+ (1.73 Å). This is larger than the PB channel radius of ~1.6 Å, adding strain to the lattice framework with the intercalation of these large cations.[15] The large ionic radii make it favorable for these cations to occupy defect sites, which are prevalent in these *high-defect* nanocrystals, rather than remaining within the channels.[36, 37]

Figure 3.4b shows the C-rate fluctuation with SOC for the K^+-, Na^+-, and NH_4^+-based electrolytes, each with their own distinct charging behavior. The NH_4^+ electrolyte shows initially a slow rise in C-rate, charging at half the rate for the initial 20% of charging compared to the K^+ electrolyte. However, this rise continues to 40% SOC, reaching the same C-rate maximum as the K^+ electrolyte. With further charging, the C-rate equilibrates at 55% SOC and is very similar to the K^+ electrolyte for the remaining charging period. These two electrolytes behave similarly because they possess similar ionic radii and are weakly bound to water molecules, which promotes desolvation and intercalation into the PB lattice. The main difference is the initial 20% charge period which suggests that NH_4^+ cations gradually stabilize the reduced surface iron centers, with the C-rate increasing with intercalation. The presence of H-bonding between water molecules and NH_4^+ cations and how the water molecules pack results in a more ordered hydration shell when compared with K^+.[38] We hypothesize this slightly stronger NH_4^+-water interaction hampers the stabilization of surface iron centers and the desolvation prior to intercalation, but overall this

has a minor effect on the charge/discharge rate. The Na^+-based electrolyte, as we could elude from the slow rate of change in the absorption, shows significantly slower intercalation C-rate, hovering around 1 throughout the charge period (C-rate spikes are a result of negative potential steps). The hydration sphere of Li^+ and Na^+ cations are larger than the other alkali cations, with radii of 3.82 and 3.78 Å, respectively, whereas for K^+ and NH_4^+, the hydration shell is ~3.7 Å.[39] The concentration of positive charge within a small ionic radius results in these cations possessing high hydration enthalpy energies, therefore, these cations struggle to desolvate and intercalate, with our experiments confirming the PB nanocrystals' affinity to intercalate the low concentrations of K^+ over the higher concentration of Li^+.[40]

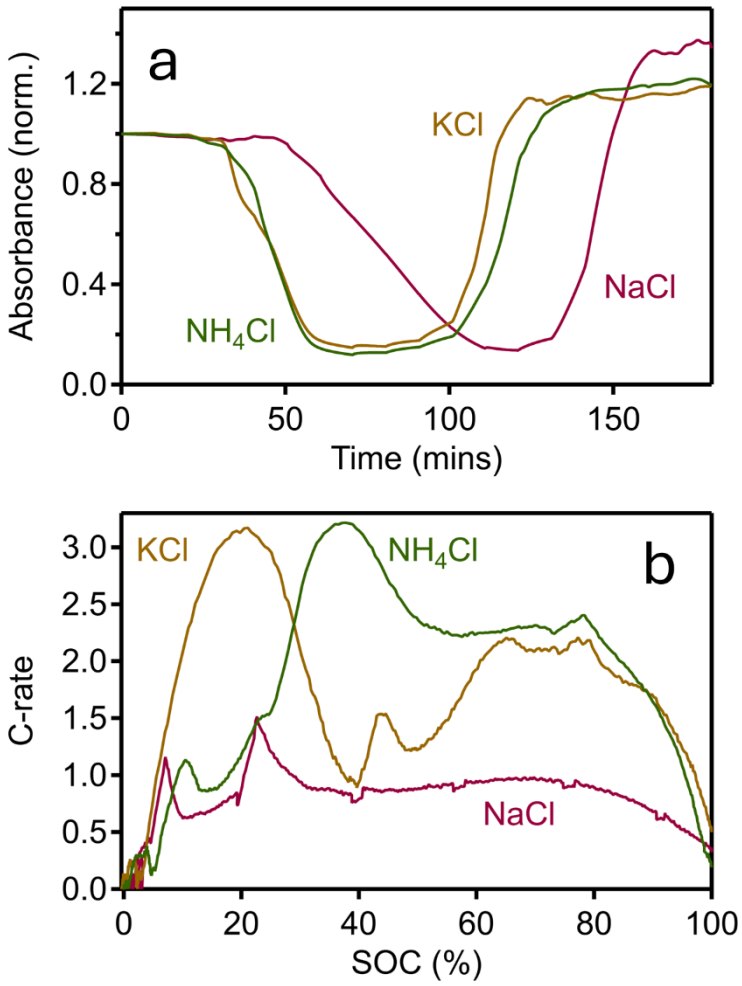

Figure 3.4 (a) An overlay of absorption variation with time during a charge/discharge cycle in 0.05 M A^+ supporting electrolyte. Potassium ferricyanide would contribute 9 mM K^+ concentration, with the remaining 0.41 M A^+ compensated by KCl/NaCl/NH_4Cl supporting electrolyte salt. **(b)** The C-rate vs SOC as determined from the charging region data in panel (a) for 0.05 M A^+ supporting electrolyte species. A boxcar average has been applied to the real-time C-rate data for data smoothing, with the data representing the average C-rate per minute of data points.

We established Li^+ intercalation is unfavorable if in the presence of a larger ionic cation, such as K^+, hence, demonstrates C-rate characteristics similar to a K^+-based electrolyte (Figure B.4). The Na^+-based electrolyte shows subdued charging kinetics vs K^+-based electrolytes, suggesting that the higher concentration of Na^+ is outcompeting the minority K^+ as the charge compensating intercalant. Figure 3.5 shows the effect on the C-rate at different Na^+-based electrolyte concentrations. Focusing on the 0.025 M A^+ electrolyte, it is evident the C-rate profile bears some resemblance to the K^+-based electrolyte, resulting in a faster charging rate across the

whole charge period vs the 0.05 M A^+ electrolyte. Na^+ is still competitive with K^+ at this lower electrolyte concentration, but this highlights the same hinderance present with the Li^+ electrolyte. The high hydration enthalpy energies contribute to the slow charging kinetics due to the desolvation process prior to intercalation being the rate determining step.

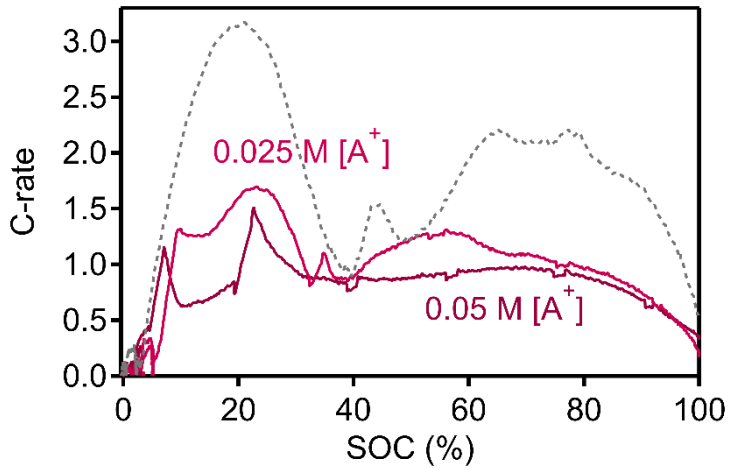

Figure 3.5 The C-rate vs SOC for 0.05 and 0.025 M A^+ supporting electrolyte species. Potassium ferricyanide would contribute 9 mM K^+ concentration, with the remaining 0.41 and 0.16 M A^+ compensated by NaCl supporting electrolyte salt for 0.05 and 0.025 M A^+ electrolytes, respectively. The dashed grey line represents the C-rate data for the 0.05 M K^+ electrolyte for comparison. A boxcar average has been applied to the real-time C-rate data for data smoothing, with the data representing the average C-rate per minute of data points.

Figure 3.6 shows the charge and discharge kinetics of PB nanocrystals in NaCl, KCl, and NH_4Cl supporting electrolytes. Regardless of the supporting electrolyte identity, the charge/discharge ionic diffusion coefficients are all comfortably within an order of magnitude, with the charging ionic diffusion coefficients of ~1 x 10^{-16} cm^2 s^{-1} and the discharge exhibiting ~2 x 10^{-16} cm^2 s^{-1}. Based of our results, K^+-based electrolytes show the fastest charge/discharge ionic diffusion coefficients vs other A^+ cation salts, although NH_4^+-based electrolytes are a good alternative, exhibiting identical charging rates and comparable discharging rates. Na^+-based electrolytes are commonly used as a lithium alternative and we demonstrate that, although not the most ideal electrolyte with a charging rate of half of the K^+ and NH_4^+-based electrolytes, still

exhibits discharge rates similar to the K^+-based electrolyte. We note that all the electrolytes consist of Cl^- anions, chosen for its prevalence within literature and that it is a strong adsorbent, important for stabilizing the surface during PB oxidation and aiding in the deintercalation mechanism, resulting in faster discharge kinetics.[41]

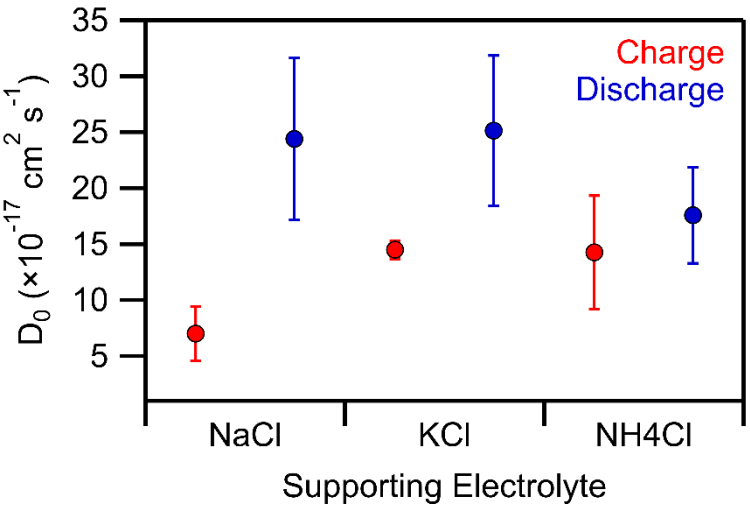

Figure 3.6 The charge and discharge ionic diffusion coefficient (D_0) for PB nanocrystals in NaCl, KCl, and NH_4Cl supporting electrolytes. The D_0 is the measure of the cation (de)intercalation kinetics within the PB nanocrystal lattice.

3.4 Summary

Herein, we have detailed a spectroelectrochemical analysis technique for probing the ionic diffusion kinetics, correlating well with electrochemical methods, such as PITT. Investigating the redox targeting system of ferricyanide and PB, our results differentiate with previous work within literature, that typically report ionic diffusion coefficients in the 10^{-8} to 10^{-11} cm^2 s^{-1}. Our results of ~10^{-17} cm^2 s^{-1} are in line with a minority, and more recent, number of literature results reporting slower diffusion kinetics.[42-44] We have demonstrated the variance in diffusion kinetics with the intercalant species. However, beyond previous reports, we can detect fluctuations in the C-rate and relate these to the chemical properties of the intercalants, thus, demonstrating the powerful insight gained from this spectroelectrochemical technique. Ultimately, the slow ionic diffusion kinetics determined within this report are not a limiting factor for this redox targeting system, demonstrating fast charge/discharge times that outperform the C-rate design requirement for long-duration discharge RT-RFBs. The C-rates demonstrated herein suggest this redox targeting system to also have limited assistance in electrical demand spikes, beyond peak shaving, due to the high-power output capability. We have only investigated colloidal PB nanocrystals grown by coprecipitation, however, low-defect PB cubes are a popular cathode material due to their enhanced cycling durability and higher theoretical specific capacity. Furthermore, RT-RFBs commonly immobilize the redox-active solid with conductive additive and organic binder into a pellet morphology. Extending the study to these other morphologies and composites will be informative to the redox targeting community for the preparation of PB as a redox-solid additives to maximize the C-rate capability of the system.

3.5 References

(1) Mongird, K.; Viswanathan, V. V.; Alam, J.; Vartanian, C.; Sprenkle, V. 2020 Grid Energy Storage Technology Cost and Performance Assessment. **2020**.

(2) Mauler, L.; Duffner, F.; Zeier, W. G.; Leker, J. Battery cost forecasting: a review of methods and results with an outlook to 2050. *Energy & Environmental Science* **2021**, *14* (9), 4712-4739, 10.1039/D1EE01530C. DOI: 10.1039/D1EE01530C.

(3) Dunn, B.; Kamath, H.; Tarascon, J.-M. Electrical Energy Storage for the Grid: A Battery of Choices. *Science* **2011**, *334* (6058), 928-935. DOI: doi:10.1126/science.1212741.

(4) Mai; Trieu; Jadun, P.; Logan, J.; McMillan, C.; Muratori, M.; Steinberg, D.; Vimmerstedt, L.; Jones, R.; Haley, B.; et al. Electrification Futures Study: Scenarios of Electric Technology Adoption and Power Consumption for the United States. *National Renewable Energy Laboratory, Golden, CO* **2018**, *NREL/TP-6A20-71500*.

(5) Yang, Z.; Zhang, J.; Kintner-Meyer, M. C. W.; Lu, X.; Choi, D.; Lemmon, J. P.; Liu, J. Electrochemical Energy Storage for Green Grid. *Chemical Reviews* **2011**, *111* (5), 3577-3613. DOI: 10.1021/cr100290v.

(6) Barton, J. P.; Infield, D. G. Energy storage and its use with intermittent renewable energy. *IEEE Transactions on Energy Conversion* **2004**, *19* (2), 441-448. DOI: 10.1109/TEC.2003.822305.

(7) Yuan, Z.; Yin, Y.; Xie, C.; Zhang, H.; Yao, Y.; Li, X. Advanced Materials for Zinc-Based Flow Battery: Development and Challenge. *Advanced Materials* **2019**, *31* (50), 1902025. DOI: https://doi.org/10.1002/adma.201902025.

(8) Soloveichik, G. L. Flow Batteries: Current Status and Trends. *Chemical Reviews* **2015**, *115* (20), 11533-11558. DOI: 10.1021/cr500720t.

(9) Hu, B.; DeBruler, C.; Rhodes, Z.; Liu, T. L. Long-Cycling Aqueous Organic Redox Flow Battery (AORFB) toward Sustainable and Safe Energy Storage. *Journal of the American Chemical Society* **2017**, *139* (3), 1207-1214. DOI: 10.1021/jacs.6b10984.

(10) Skyllas-Kazacos, M.; Chakrabarti, M. H.; Hajimolana, S. A.; Mjalli, F. S.; Saleem, M. Progress in Flow Battery Research and Development. *Journal of The Electrochemical Society* **2011**, *158* (8), R55. DOI: 10.1149/1.3599565.

(11) Yu, J.; Fan, L.; Yan, R.; Zhou, M.; Wang, Q. Redox Targeting-Based Aqueous Redox Flow Lithium Battery. *ACS Energy Letters* **2018**, *3* (10), 2314-2320. DOI: 10.1021/acsenergylett.8b01420.

(12) Chen, Y.; Zhou, M.; Xia, Y.; Wang, X.; Liu, Y.; Yao, Y.; Zhang, H.; Li, Y.; Lu, S.; Qin, W.; et al. A Stable and High-Capacity Redox Targeting-Based Electrolyte for Aqueous Flow Batteries. *Joule* **2019**, *3* (9), 2255-2267. DOI: https://doi.org/10.1016/j.joule.2019.06.007.

(13) Li, L.; Kim, S.; Wang, W.; Vijayakumar, M.; Nie, Z.; Chen, B.; Zhang, J.; Xia, G.; Hu, J.; Graff, G.; et al. A Stable Vanadium Redox-Flow Battery with High Energy Density for Large-Scale Energy Storage. *Advanced Energy Materials* **2011**, *1* (3), 394-400. DOI: https://doi.org/10.1002/aenm.201100008.

(14) Fan, L.; Jia, C.; Zhu, Y. G.; Wang, Q. Redox Targeting of Prussian Blue: Toward Low-Cost and High Energy Density Redox Flow Battery and Solar Rechargeable Battery. *ACS Energy Letters* **2017**, *2* (3), 615-621. DOI: 10.1021/acsenergylett.6b00667.

(15) Ma, L.; Cui, H.; Chen, S.; Li, X.; Dong, B.; Zhi, C. Accommodating diverse ions in Prussian blue analogs frameworks for rechargeable batteries: The electrochemical redox reactions. *Nano Energy* **2021**, *81*, 105632. DOI: https://doi.org/10.1016/j.nanoen.2020.105632.

(16) Song, Q.; Li, Z.; Gan, S.; Dong, W.; Wang, W.; Zhang, J.; Yu, Q. Progress and challenges of Prussian blue analogs for potassium-ion batteries: a perspective on redox-active transition metals. *Journal of Materials Chemistry A* **2023**, *11* (4), 1532-1550, 10.1039/D2TA08573A. DOI: 10.1039/D2TA08573A.

(17) Cheng, G.; Dong, S. Chronoabsorptometric study of Prussian blue modified film electrode. *Electrochimica Acta* **1987**, *32* (11), 1561-1565. DOI: https://doi.org/10.1016/0013-4686(87)90004-1.

(18) Kulesza, P. J.; Malik, M. A.; Miecznikowski, K.; Wolkiewicz, A.; Zamponi, S.; Berrettoni, M.; Marassi, R. Countercation-Sensitive Electrochromism of Cobalt Hexacyanoferrate Films. *Journal of The Electrochemical Society* **1996**, *143* (1), L10. DOI: 10.1149/1.1836374.

(19) Kondrat'ev, V. V.; Tikhomirova, A. V.; Yakovleva, S. V.; Malev, V. V. Effect of electrolyte cations on the charge transfer in films of prussian blue. *Russian Journal of Electrochemistry* **2000**, *36* (5), 522-532. DOI: 10.1007/BF02757416.

(20) Stilwell, D. E.; Park, K. H.; Miles, M. H. Electrochemical studies of the factors influencing the cycle stability of Prussian Blue films. *Journal of Applied Electrochemistry* **1992**, *22* (4), 325-331. DOI: 10.1007/BF01092684.

(21) Feldman, B. J.; Murray, R. W. Electron diffusion in wet and dry Prussian blue films on interdigitated array electrodes. *Inorganic Chemistry* **1987**, *26* (11), 1702-1708. DOI: 10.1021/ic00258a014.

(22) García-Jareño, J. J.; Navarro, J. J.; Roig, A. F.; Scholl, H.; Vicente, F. Impedance analysis of Prussian Blue films deposited on ITO electrodes. *Electrochimica Acta* **1995**, *40* (9), 1113-1119. DOI: https://doi.org/10.1016/0013-4686(95)00017-9.

(23) Kondratiev, V. V.; Tikhomirova, A. V.; Malev, V. V. Study of charge transport processes in Prussian-blue film modified electrodes. *Electrochimica Acta* **1999**, *45* (4), 751-759. DOI: https://doi.org/10.1016/S0013-4686(99)00254-6.

(24) Mizuno, Y.; Okubo, M.; Hosono, E.; Kudo, T.; Zhou, H.; Oh-ishi, K. Suppressed Activation Energy for Interfacial Charge Transfer of a Prussian Blue Analog Thin Film Electrode with Hydrated Ions (Li+, Na+, and Mg2+). *The Journal of Physical Chemistry C* **2013**, *117* (21), 10877-10882. DOI: 10.1021/jp311616s.

(25) Yan, R.; Ghilane, J.; Phuah, K. C.; Pham Truong, T. N.; Adams, S.; Randriamahazaka, H.; Wang, Q. Determining Li+-Coupled Redox Targeting Reaction Kinetics of Battery Materials with Scanning Electrochemical Microscopy. *The Journal of Physical Chemistry Letters* **2018**, *9* (3), 491-496. DOI: 10.1021/acs.jpclett.7b03136.

(26) Jennings, J. R.; Huang, Q.; Wang, Q. Kinetics of LixFePO4 Lithiation/Delithiation by Ferrocene-Based Redox Mediators: An Electrochemical Approach. *The Journal of Physical Chemistry C* **2015**, *119* (31), 17522-17528. DOI: 10.1021/acs.jpcc.5b03561.

(27) Konopka, S. J.; McDuffie, B. Diffusion coefficients of ferri- and ferrocyanide ions in aqueous media, using twin-electrode thin-layer electrochemistry. *Analytical Chemistry* **1970**, *42* (14), 1741-1746. DOI: 10.1021/ac50160a042.

(28) Wen, C. J.; Boukamp, B. A.; Huggins, R. A.; Weppner, W. Thermodynamic and Mass Transport Properties of " LiAl " *Journal of The Electrochemical Society* **1979**, *126* (12), 2258. DOI: 10.1149/1.2128939.

(29) Dereka, B.; Lewis, N. H. C.; Zhang, Y.; Hahn, N. T.; Keim, J. H.; Snyder, S. A.; Maginn, E. J.; Tokmakoff, A. Exchange-Mediated Transport in Battery Electrolytes: Ultrafast or Ultraslow? *Journal of the American Chemical Society* **2022**, *144* (19), 8591-8604. DOI: 10.1021/jacs.2c00154.

(30) Landstorfer, M.; Jacob, T. Mathematical modeling of intercalation batteries at the cell level and beyond. *Chemical Society Reviews* **2013**, *42* (8), 3234-3252, 10.1039/C2CS35050E. DOI: 10.1039/C2CS35050E.

(31) Lee, G.; Wong, C. M.; Sevov, C. S. Single vs Dual Shuttle Cycling of Polyferrocenyl Cathodes for Redox Targeting Flow Batteries. *ACS Energy Letters* **2022**, *7* (10), 3337-3344. DOI: 10.1021/acsenergylett.2c01794.

(32) Shiga, T.; Kondo, H.; Kato, Y.; Inoue, M. Insertion of Calcium Ion into Prussian Blue Analogue in Nonaqueous Solutions and Its Application to a Rechargeable Battery with Dual Carriers. *The Journal of Physical Chemistry C* **2015**, *119* (50), 27946-27953. DOI: 10.1021/acs.jpcc.5b10245.

(33) Vo, T. N.; Kang, J. E.; Lee, H.; Lee, S.-W.; Ahn, S.-k.; Hur, J.; Kim, I. T. Ultra-stable calcium ion batteries with Prussian blue nanodisks. *EcoMat* **2023**, *5* (2), e12285. DOI: https://doi.org/10.1002/eom2.12285.

(34) Hurlbutt, K.; Wheeler, S.; Capone, I.; Pasta, M. Prussian Blue Analogs as Battery Materials. *Joule* **2018**, *2* (10), 1950-1960. DOI: https://doi.org/10.1016/j.joule.2018.07.017.

(35) Phadke, S.; Mysyk, R.; Anouti, M. Effect of cation (Li+, Na+, K+, Rb+, Cs+) in aqueous electrolyte on the electrochemical redox of Prussian blue analogue (PBA) cathodes. *Journal of Energy Chemistry* **2020**, *40*, 31-38. DOI: https://doi.org/10.1016/j.jechem.2019.01.025.

(36) Wang, R. Y.; Shyam, B.; Stone, K. H.; Weker, J. N.; Pasta, M.; Lee, H.-W.; Toney, M. F.; Cui, Y. Reversible Multivalent (Monovalent, Divalent, Trivalent) Ion Insertion in Open Framework Materials. *Advanced Energy Materials* **2015**, *5* (12), 1401869. DOI: https://doi.org/10.1002/aenm.201401869.

(37) Moritomo, Y.; Igarashi, K.; Kim, J.; Tanaka, H. Size Dependent Cation Channel in Nanoporous Prussian Blue Lattice. *Applied Physics Express* **2009**, *2* (8), 085001. DOI: 10.1143/APEX.2.085001.

(38) Aydin, F.; Zhan, C.; Ritt, C.; Epsztein, R.; Elimelech, M.; Schwegler, E.; Pham, T. A. Similarities and differences between potassium and ammonium ions in liquid water: a first-principles study. *Physical Chemistry Chemical Physics* **2020**, *22* (4), 2540-2548, 10.1039/C9CP06163K. DOI: 10.1039/C9CP06163K.

(39) Xu, C.; Yang, Z.; Zhang, X.; Xia, M.; Yan, H.; Li, J.; Yu, H.; Zhang, L.; Shu, J. Prussian Blue Analogues in Aqueous Batteries and Desalination Batteries. *Nano-Micro Letters* **2021**, *13* (1), 166. DOI: 10.1007/s40820-021-00700-9.

(40) Hayamizu, K.; Chiba, Y.; Haishi, T. Dynamic ionic radius of alkali metal ions in aqueous solution: a pulsed-field gradient NMR study. *RSC Advances* **2021**, *11* (33), 20252-20257, 10.1039/D1RA02301B. DOI: 10.1039/D1RA02301B.

(41) Lamprecht, X.; Speck, F.; Marzak, P.; Cherevko, S.; Bandarenka, A. S. Electrolyte Effects on the Stabilization of Prussian Blue Analogue Electrodes in Aqueous Sodium-Ion Batteries. *ACS Applied Materials & Interfaces* **2022**, *14* (2), 3515-3525. DOI: 10.1021/acsami.1c21219.

(42) Shrivastava, A.; Smith, K. C. Electron Conduction in Nanoparticle Agglomerates Limits Apparent Na+ Diffusion in Prussian Blue Analogue Porous Electrodes. *Journal of The Electrochemical Society* **2018**, *165* (9), A1777. DOI: 10.1149/2.0861809jes.

(43) Qin, M.; Ren, W.; Jiang, R.; Li, Q.; Yao, X.; Wang, S.; You, Y.; Mai, L. Highly Crystallized Prussian Blue with Enhanced Kinetics for Highly Efficient Sodium Storage. *ACS Applied Materials & Interfaces* **2021**, *13* (3), 3999-4007. DOI: 10.1021/acsami.0c20067.

(44) Komayko, A. I.; Arkharova, N. A.; Presnov, D. E.; Levin, E. E.; Nikitina, V. A. Resolving the Seeming Contradiction between the Superior Rate Capability of Prussian Blue Analogues and the Extremely Slow Ionic Diffusion. *The Journal of Physical Chemistry Letters* **2022**, *13* (14), 3165-3172. DOI: 10.1021/acs.jpclett.2c00482.

Appendix A. Redox Targeting of Sodium Superionic Conductors in Aqueous Anolytes for High-Energy-Density Batteries

A.1 Materials

Chrysazin (≥98.0%), was purchased from TCI America. Sodium hydrosulfite tech. ($Na_2S_2O_4$, ≥85%), hydrochloric acid ACS grade (HCl, 37%) was purchased from Thermo Scientific Chemicals. Glyoxylic acid (50 wt.% in H_2O), triethanolamine (TEOA, 99.0%), manganese (II) chloride tetrahydrate ($MnCl_2.4H_2O$, ≥98%), sodium hydroxide pellets (≥98%), sodium ferrocyanide decahydrate (≥98.0%), and poly(vinylidene fluoride) (PVDF, average M_w ~534,000) were purchased from Sigma-Aldrich. Iron (II) chloride tetrahydrate ($FeCl_2.4H_2O$, 99%), potassium ferricyanide ($K_3[Fe(CN)_6]$, 99.9%) and 1-methyl-2-pyrrolidinone ACS grade (NMP, ≥99.0%) were purchased from Alfa Aesar. Anthraquinone-2,7-disulfonic acid disodium salt (2,7-anthraquinone disulfonate, or 2,7-ADS, ≥80%) and anthraflavic acid (≥92%) were purchased from Santa Cruz Biotechnology Inc. Iron (III) chloride hexahydrate ($FeCl_3.6H_2O$, 99.7%), o-phosphoric acid (85%, H_3PO_4), and sodium phosphate monobasic hydrate (99%, NaH_2PO_4) were purchased from Fisher Chemicals. Titanium dioxide (Aeroxide P25, TiO_2) was purchased from Degussa. Chemical-resistant 121 x 121 plastic mesh and polyurethane (PU) foam (1/8” thickness, 60 pores per inch) were purchased from McMaster-Carr. Acrylic dowel rods (Ø 1”), Gorilla® waterproof clear caulk, Dawn® detergent, and 1” diameter, 0.22 μm polypropylene mesh hydrophilic filters were purchased from Amazon. Nafion 115 sheets, Nafion ionomer dispersion (5 wt.% in alcohol), carbon cloth (Panex PW03, 0.4 mm uncompressed thickness, Zoltek Carbon Fiber), and soft graphitic felt were purchased from Fuel Cell Store. All chemicals were used without further purification.

A.2 Electrolyte preparation

The $[Fe(TEOA)OH]^{2-}$ anolyte was prepared according to literature procedures[1, 2] by first dissolving 3.96 g (20 mmol) $FeCl_2•4H_2O$ in 21 mL of deionized water with stirring and N_2 sparging for 20 minutes to form a light green solution. Then, 2 equivalents of TEOA (5.4 mL, 40 mmol) were added to the Fe^{2+} flask, upon which a pastel-blue slurry was formed. Meanwhile, 9–10 equivalents of NaOH (7.22 g, 180 mmol) were dissolved in 10 mL of deionized water. The NaOH solution was cooled, then added to the Fe^{2+}-TEOA mixture, changing the pastel-blue slurry to a forest-green solution. The final volume was adjusted to 40 mL to create a 0.5 M stock solution. $[Fe(TEOA)OH]^-$ was prepared by replacing $FeCl_2•4H_2O$ with $FeCl_3•6H_2O$. This stock was diluted in 5 M NaOH for H-cell measurements.

0.1 M $[Mn(TEOA)OH]^{2-/-}$ was prepared according to literature procedures[3] by dissolving 0.40g (2 mmol) $MnCl_2•4H_2O$ in 2 ml of deionized water with stirring and N_2 sparging for 20 minutes. Afterwards, 30 equivalents of TEOA (7.96 mL, 60 mmol) were added to the Mn^{2+} flask, upon which a pale-yellow solution was formed. Furthermore, 2.00 g NaOH (50 mmol) were dissolved in deionized water and made up to 10 ml in a volumetric flask. Once cooled, this solution was added to the Mn^{2+}-TEOA mixture. Finally, the $[Mn(TEOA)OH]^{2-}$ solution was sparged with air for 5 minutes, changing the pale-yellow solution to a dark green solution, indicating Mn oxidation and the presence of $[Mn(TEOA)OH]^-$. Electrolytes with organic compounds were prepared in 5–10 mM concentrations by dissolving in 0.1–1 M NaOH solution as the supporting electrolyte. Inorganic compounds were prepared in 5 mM concentration by diluting in 5 M NaOH.

Functionalized Chrysazin (FnChrysazin) was prepared according to literature procedure[4] by dissolving 2.0 g Chrysazin (8.3 mmol) in 70 mL 1 M NaOH solution with stirring and N_2 sparging for 30 minutes. This was transferred to an N_2-filled wetbox. The first addition of $Na_2S_2O_4$ (1.94 g, 11.1 mmol) was added to the dispersion to give a dark red solution. Then 3.7 g of N_2-sparged aqueous glyoxylic acid solution (50 wt%., 3eq.) was added to the reaction and left to stir for 1 hour

at room temperature. Afterward, a second addition of $Na_2S_2O_4$ (1.84 g, 10.6 mmol) was added to the reaction and the temperature was raised to 80 ºC. This was held for 30 minutes, after which the reaction was cooled to room temperature and exposed to air. The solution was acidified with 2 M HCl to precipitate the crude solid, which was collected by centrifugation. The crude product was redispersed in 1 M NaOH solution, subsequently acidified again with 2 M HCl and centrifuged. A final deionized water wash and centrifuge, followed by drying in an 80 ºC oven overnight, yields 2.2 g of an orange-yellow solid (74%). The ^{1}H NMR spectrum of deprotonated FnChrysazin is shown in Figure A.10.

A.3 Synthesis of $NaTi_2(PO_4)_3$ (NTP) powder

NTP was synthesized *via* solvothermal methods as described in literature.[5, 6] Briefly, 5.0 g TiO_2 (60 mmol), 4.4 g $NaH_2PO_4•H_2O$ (30 mmol), 5.0 mL H_3PO_4 (74 mmol), and 5.0 mL deionized water were mixed thoroughly within a 23 ml PTFE vessel to form a thick white paste. The vessel was transferred to a stainless-steel pressure reactor and heated to 150 ℃ for 6 h, then cooled overnight. In both cases, the product was washed 3 times with deionized water and centrifugation. The white product was then dispersed in ~5 mL isopropanol and poured onto a watchglass to dry.

A.4 NTP immobilization strategies and preparation

A.4.1 NTP foam synthesis

NTP was synthesized with a porous foam morphology directly by using PU foam substrates. Briefly, an NTP precursor paste was prepared as described above. Disks of PU foam (60 pores per inch, 0.125” thick, McMaster Carr) were cut with a cork borer (0.710” diameter). The NTP precursor paste was then worked into the PU disks. Excess paste was gently squeezed out

to leave foam disks that were fully coated with the precursor while still maintaining their porosity. The disks were then placed on the flat side of a fire brick and heated in a muffle furnace to 900 °C over a 6 h period. The temperature was maintained at 900 °C for 6 h before turning off the furnace and allowing the products to cool naturally. Disks were then placed on paper towels and 1 mL of a 1% w/v Nafion ionomer dispersion (diluted in isopropanol from 5%) was added evenly to each disk. The disks were then gently flipped and another mL of the Nafion dispersion was added to the other side. After allowing the Nafion dispersion to wick through, the disks were placed on a watchglass and transferred to an 80 °C oven to dry fully overnight.

A.4.2 NTP foam composite preparation

NTP powder was bound to a porous PU foam to achieve a flexible redox-active foam substrate. Briefly, NTP powder was prepared as described above. Disks of PU foam (60 pores per inch, 0.125” thick, McMaster Carr) were cut with a cork borer (0.710” diameter). Caulk was then worked into the PU disks. Excess caulk was gently squeezed out to leave foam disks that were fully coated with caulk while still maintaining their porosity. The caulk-prepared substrates were then hooked with a 22 G copper wire, for ease of handling, and dredged in NTP powder on both sides of the disk. The excess powder was tapped off and the dredging process was repeated one more time. The prepared NTP foam composites were left to set overnight.

A.4.3 Loose NTP redox filter preparation

Figure A.1 shows an image and a schematic of the fully constructed powder redox filter. Acrylic rods were machined on a lathe to form a body and cap component which constitutes the outer redox filter components. We fabricated a custom filter from acrylic material by machining an acrylic rod on a lathe. The filter consists of two pieces, the main body and a cap. The main body is simply an NTP flow through cavity. The cap contains a 0.22 μm particle exclusion mesh to filter NTP from the electrolyte prior to the battery stack inlet line.

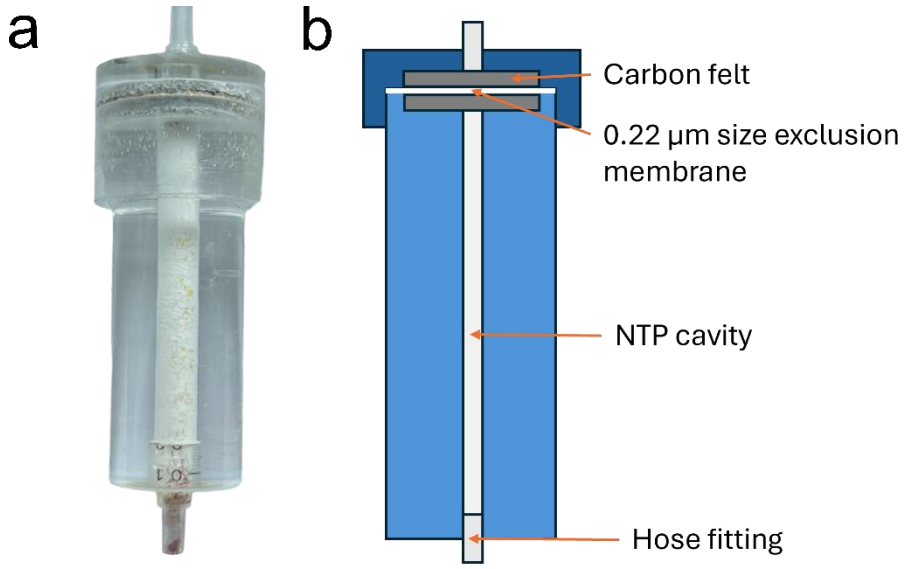

Figure A.1 (a) Image of assembled powder redox filter. **(b)** Schematic of assembled powder redox filter.

A.4.4 Redox strip filter preparation

Redox-active strips of NTP on polypropylene mesh were prepared by cutting a ~7 × 82 cm strip of polypropylene (121 × 121, 0.0041" opening size, McMaster-Carr). A solution of PVDF (5% w/v) was prepared by dissolving 1 g of PVDF in 20 mL of NMP with stirring, heating, and sonication. Next, 2 g of NTP were mixed with 5 mL of the PVDF solution and 35 mL of isopropanol were added to create a dilute slurry and facilitate evaporation. The polypropylene mesh was secured with clips at a ~70° angle, and the NTP slurry was added slowly and evenly from the top down. The slurry was allowed to dry before adding more layers of the NTP slurry. The container was shaken vigorously between additions to ensure proper mixing. The strip was allowed to dry overnight. Assembly of redox filter was achieved using two 20 mL syringes for the body to house the tightly rolled redox strip (Figure A.2b). Roughly 30 pieces of 1 mm PTFE tubing the same width as the strip to act as spacers for improved electrolyte flow. The body was epoxied to seal the redox strip filter.

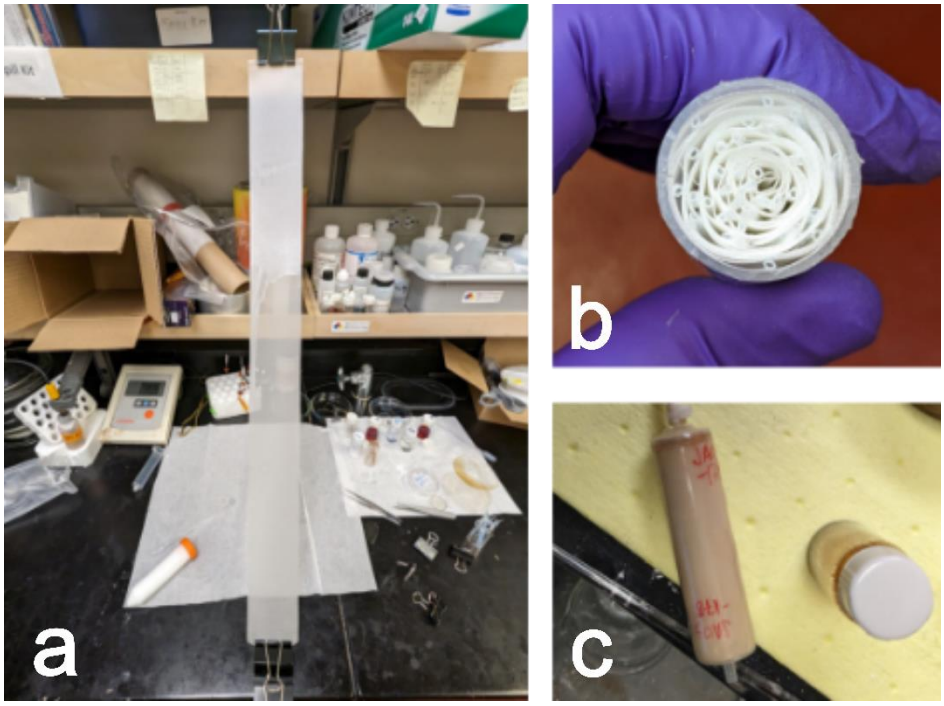

Figure A.2 (a) Preparation of NTP strip *via* dropcasting. **(b)** Rolled NTP strip within syringe body, fitted with PTFE spacers. **(c)** The fully assembled redox strip filter after a battery cycling experiment.

A.4.5 NTP foam redox filter preparation

A home-built inline filter was constructed from 3/4" PVC fittings. The main container was a 3" tube with NPT threads on both ends. Holes were drilled in the center of ¾" NPT caps. 1 mL syringes were used as fittings by removing the plunger and cutting at the ~50 µm mark. The syringe fittings were then attached to the holes of the PVC end caps with epoxy and allowed to fully cure. To ensure proper filtration of any loose solids, two small pieces of carbon felt were added into the syringe fitting on the outlet side and a large circle of carbon felt (~0.866") was added to the endcap before connecting to the PVC tubing. A small amount of anti-seize thread lock was added to the fittings to ensure a water-tight fit. Next, Nafion-treated NTP foam disks were added into the tube by gently pushing down with the plunger of a syringe. The tube was then filled with 5 M NaOH and the filter outlet was plugged. A syringe plunger was placed in the tube to keep the Nafion/NTP disks from floating out of the solution, and the disks were allowed to soak in the NaOH overnight

to allow for a full exchange of protons to sodium ions in the Nafion. The filter was then drained and rinsed out with 400 – 500 mL of DI water to remove any loose NTP powder.

Figure A.3 Image of fully constructed NTP foam redox filter.

A.4.6 NTP foam composite redox filter preparation

A bespoke inline filter was machined from acrylic rods on the lathe. The filter consists of three components, a lower electrolyte outlet piece, a mid-body piece, and an electrolyte inlet cap. The lower piece is a countersunk double well, the initial well has a diameter of 0.875” and a depth of 0.6”. The inner well has a diameter of 0.710” and a depth of 0.6”. The length of the piece is 1.6” with a 0.253” hole drilled out in the middle for the hose fitting. The mid-body length is 3” with an outer diameter of 0.875” and an inner diameter of 0.710”. The inlet cap has an inner diameter of 0.875” to a depth of 0.6”. The cap length is 1” with a 0.253” hole drilled out in the middle for the hose fitting. A hose fitting (as described earlier) was fitted to the lower electrolyte outlet piece.

The prepared NTP foam composites are hydrophobic and require a prewetting procedure before the redox filter assembly. The foams are placed in a vacuum chamber and filled with a

deionized water:Dawn® solution (9:1). Attached to a Schlenk line, the chamber is slowly opened to the vacuum line, to reduce the amount of lathering to avoid Schlenk line contamination, over the course of one hour. Once the foams have sunk to the bottom of the chamber and are no longer releasing any trapped gases within its pores, foams are retrieved from the vacuum chamber, rinsed with plenty of deionized water. The foams, three acrylic body pieces, and a soft graphitic felt disk (0.710” in diameter) constitute the inline filter components. The graphitic felt disk is placed in the bottom of the lower outlet piece, acting as a coarse filter and as a spacer to improve the fluid dynamics over the foams. The foams are then placed on top of the graphitic felt until the deeper countersunk well has been filled, the remaining foams are placed at one end of the mid-body piece. A thin layer of caulk is applied to the mating sections of the lower and mid-body pieces and pressure was applied for one minute. The volume was filled with deionized water, allowing water to flow through the outlet; after the initial water flow, the outlet was plugged so the foams were submerged. The inlet cap is simply placed on top of the open mid-body section. The caulk became waterproof after one hour of setting. Prior the inserting to the flow battery electrolyte line, 1 M NaOH was pumped through for 10 minutes.

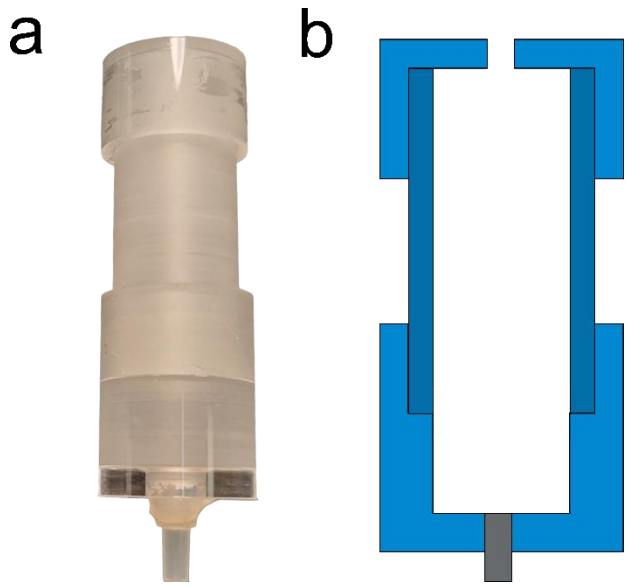

Figure A.4 (a) Image of assembled composite foam redox filter. **(b)** Schematic of assembled composite foam redox filter.

A.5 Physical characterization

Powder X-ray diffraction data were taken by drop-casting samples on silicon wafers and measuring in a Bruker D8 Discover Microfocus diffractometer using a Cu-K X-ray source, operating at 50 kV and 1000 μA. Sample stage was set to oscillate throughout the measurement.

Scanning electron microscopy (SEM) imaging was taken of either drop-cast samples on silicon wafers or, in the case for the NTP foams, were directly imaged on the Phenom-Pharos Desktop SEM (Thermo Scientific) operating at 10 kV.

Nuclear magnetic resonance (NMR) was carried out on the Bruker Avance 300. Sample preparation consisted of dissolving ~5 mg of sample in 1 mL of D_2O/NaOH.

A.6 Electrochemical characterization

Cyclic voltammograms were performed using a 3-mm diameter glassy carbon working electrode (WE), a 6 mm leakless Ag/AgCl electrode (eDAQ) was the reference electrode (RE), and a platinum wire counter electrode (CE). Measurements were carried out on a Squidstat potentiostat (Admiral Instruments). Solutions were sparged with N_2 for at least 5 minutes prior to measurement. For CVs of NTP, the NTP powder or carbon-coated NTP were mixed with carbon black and PVDF binder in a 28:12:1 mass ratio of NTP:C:PVDF and dispersed in a mixture of isopropanol and NMP. This mixture was drop-cast on a glassy carbon electrode to dry.

Galvanostatic H-cell measurements were carried out in an H-shaped glass cell separated in by a Nafion 115 membrane. The membrane was soaked in 5 M NaOH for at least 2 hours to exchange protons for Na^+. Carbon felt was used for the working electrode, Pt wire for the CE, and a 1 mm Ag/AgCl leakless electrode (eDAQ) was the reference. Both sides of the cell were sparged with N_2 for at least 15 minutes, and the cells were kept under N_2 for the entire measurement. Charge/discharge cycling was measured with a Squidstat potentiostat (Admiral Instruments). The inorganic electrolyte was sparged with N_2 for 1 hour prior to measurement.

Flow battery measurements were carried out in fuel cell hardware purchased from Fuel Cell Technologies (Albuquerque, NM). The active area was 5 cm^2 with a machined serpentine flow pattern on graphite blocks that were treated with a cured furan resin. 0.01" silicone gaskets were used on both plates. The electrodes were carbon cloth (Panex PW03, 0.4 mm uncompressed thickness, Zoltek Carbon Fiber). The ion exchange membrane (Nafion 212) was soaked in 5.0 M NaOH solution for at least an hour prior to assembling the cell. A Masterflex L/S peristaltic pump and Versilon L/S 14 tubing were used to pump the electrolytes through the electrochemical cell (100 rpm). A Squidstat potentiostat (Admiral Instruments) was used for charge/discharge measurements. The potential limits were set from 1.4 – 0.5 V, and the current was set between 12.5 – 50 mA (2.5 – 10 mA cm^2). All measurements were performed at room temperature with no

active temperature control at the electrochemical cell or electrolyte tanks. For measurements incorporating the NTP redox filter described above, the filter outlet was attached to the Versilon tubing and the anolyte solution was added through the top of the filter before adding in the inlet tubing.

A.7 Supporting relationships and calculations

According to Randles-Sevcik equation (eq. A.1) describes how the peak i_p (A) increases linearly with the square root of the scan rate υ (V s^{-1}), where n is the number of electrons transferred in the redox event, A (cm^2) is the electrode surface area (usually treated as the geometric surface area), D_o (cm^2 s^{-1}) is the diffusion coefficient of the oxidized analyte, and C^o (mol cm^{-3}) is the bulk concentration of the analyte.

$$i_p = 0.446nFAC°(\frac{nF_\nu D_o}{RT})^{\frac{1}{2}} \quad \text{(A.1)}$$

$$i_p \propto C° \quad \text{(A.2)}$$

The concentration of redox-active species within the electrolyte is proportional to the CV current response (eq. A.2)

A.7.1 Calculations for the theoretical specific capacity (C_{NTP}, mAh g^{-1})

$$C_{NTP} = \frac{nF}{M \times 3.6} \quad \text{(A.3)}$$

Where n is the number of moles of electrons transferred by one mole of NTP to N_3TP (n=2, theoretically), F is the Faraday constant (96,485 C mol^{-1}), and M is the molecular weight of NTP (402.99 g mol^{-1}). Hence, C_{NTP} is 133 mAh g^{-1}.

A.7.2 NTP foam composite volume calculation

The calculated NTP density is 2.94 g cm^{-3}.[7] Water displacement was used to determine the density of the PU foam and silicone caulk, these are 1.24 and 1.13 g cm^{-3}, respectively.

$$V = \frac{m}{\rho} \tag{A.4}$$

Where V is the volume (cm^3), m is the mass (g), and ρ is the density (g cm^{-3}).

Table A.1 Volume contributions from individual components of NTP foam composites

	V_{PU} (cm^3)	V_{NTP} (cm^3)	V_{Si} (cm^3)	V_{TOTAL} (cm^3)
FnChrysazin	0.08	0.08	0.46	0.63
FnChrysazin & 2,7-ADS	0.08	0.10	0.39	0.57

A.7.3 Theoretical volumetric capacity calculations

Working with the parameters of FnChrysazin and 2,7-ADS solubility limits of 1.3 and 0.74 M, respectively,[4, 8] and 50% of the reservoir volume is NTP solid. The other 50% reservoir volume is electrolyte. The demonstrated flow battery NTP utilization is 57%.

$$VC_{NTP} = \frac{n \times V \times \rho \times F \times \alpha}{M \times 3600} \tag{A.5}$$

Where n is the number of moles of electrons transferred by one mole of NTP to N_3TP (n=2, theoretically), V is the volume, ρ is the density (2.94 g cm^{-3}), F is the Faraday constant (96,485 C mol^{-1}), α is the material utilization factor, and M is the molecular weight of NTP (402.99 g mol^{-1}).

$$VC_{AQ} = \frac{n \times V \times C^{o} \times F}{3600} \quad \text{(A.6)}$$

Where n is the number of moles of electrons transferred by one mole of anthraquinone (AQ) to reduced AQ (n=2, theoretically), V is the volume, C^o is the concentration, and F is the Faraday constant (96,485 C mol^{-1}).

A.8 Physical characterization additional figures

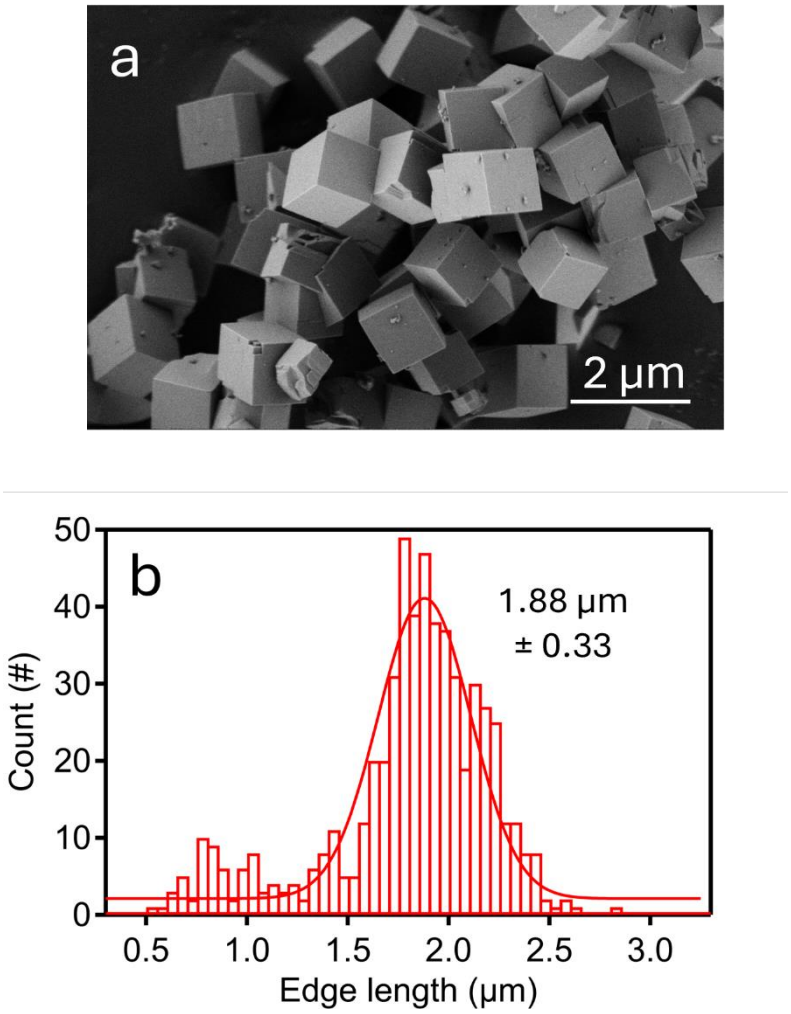

Figure A.5 (a) Scanning electron microscope image of NTP microcubes synthesized via hydrothermal sol-gel methods. **(b)** Size distribution for the cube edge length is 1.88 µm ± 0.33 µm as calculated with a Gaussian fit. Distribution represents 500 individual NTP cubes, measured by SEM.

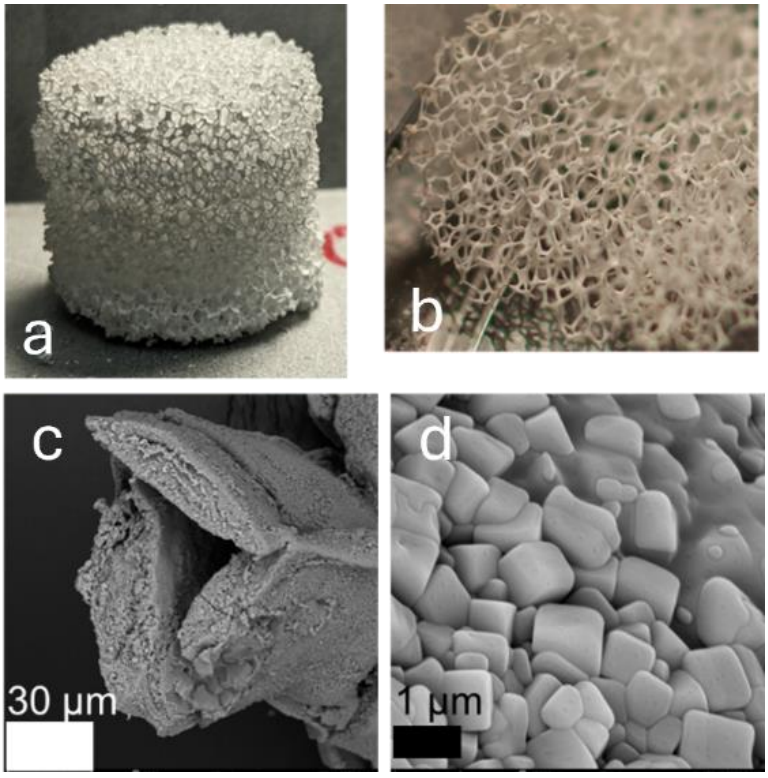

Figure A.6 (a-b) Images of free-standing pure NTP foam structures and **(c-d)** scanning electron microscope images of NTP synthesized on 60 pores per inch PU substrates.

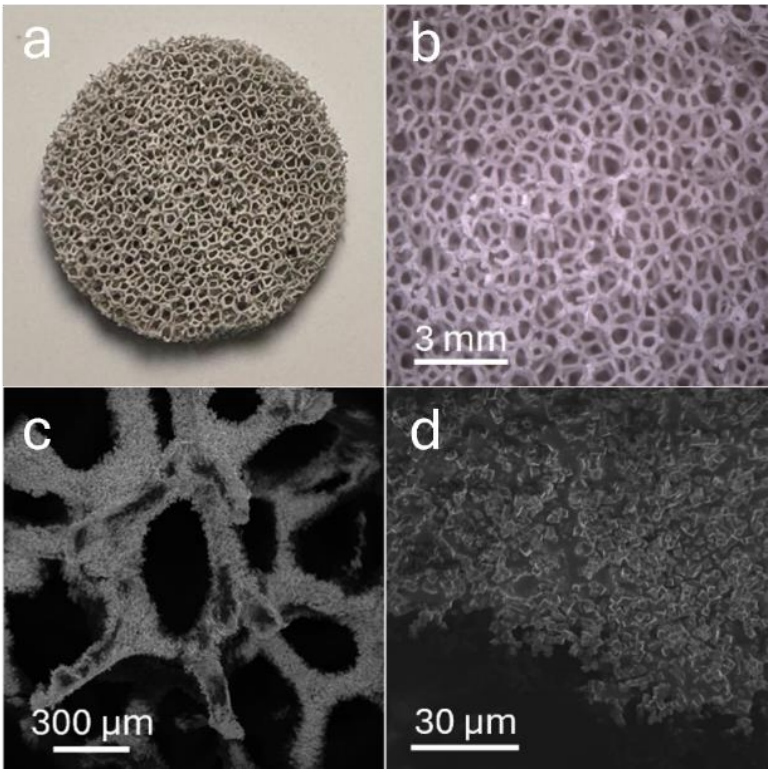

Figure A.7 (a-b) Images and **(c-d)** scanning electron microscopy images of NTP foam composites fabricated on 60 pores per inch PU substrates.

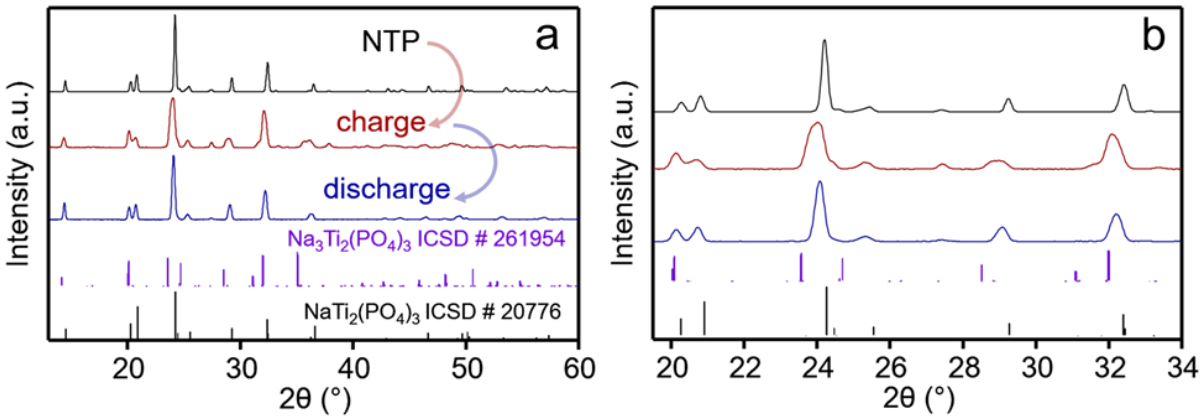

Figure A.8 (a) Powder X-ray diffraction patterns of as-made NTP (top), after reduction through one charge cycle (middle, red), and after reoxidation with one discharge cycle (middle, blue) in an H-cell. The H-cell anolyte was 5 mM each of anthraflavic acid and 2,7-ADS in 0.1 M NaOH, along with 2 molar equivalents (0.2 mmol) of NTP powder. The catholyte was 0.1 M NaOH and the current was +/-5 mA. The purple and black diffraction patterns at the bottom are literature reference for $Na_3Ti_2(PO_4)_3$ (ICSD # 261954) and $NaTi_2(PO_4)_3$ (ICSD # 20776), respectively. **(b)** Zoom-in of the data in panel (a) showing changes in relative peak intensities at ~10 2θ and the growth of additional peaks at 23.75, 28.7, and 31.5 2θ.

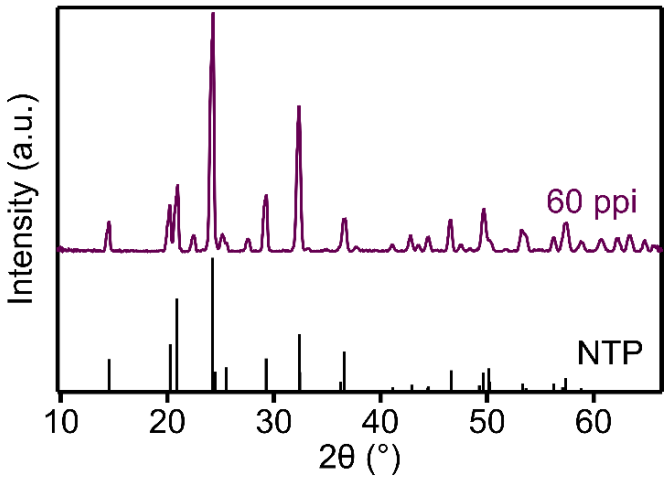

Figure A.9 Powder X-ray diffraction pattern of as-made foam templated NTP on 60 pores per inch PU foam (top). The black diffraction pattern (bottom) is the literature reference for $NaTi_2(PO_4)_3$ (ICSD # 20776).

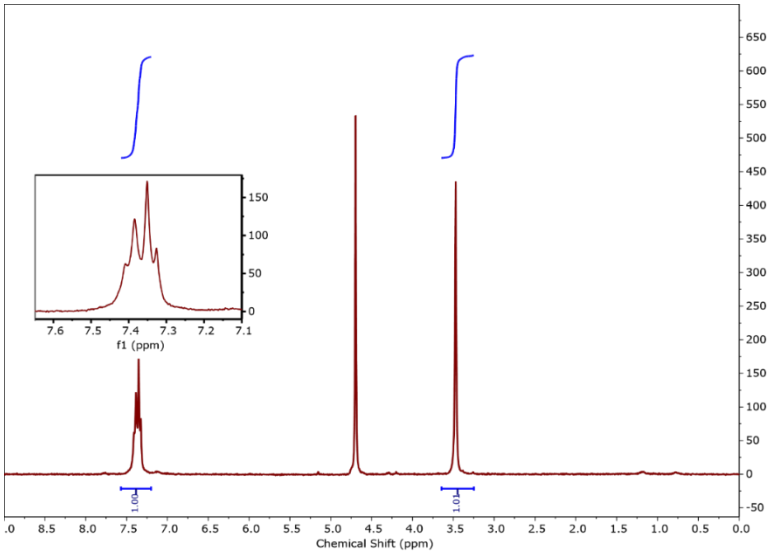

Figure A.10 ^{1}H NMR spectrum of FnChrysazin in D_2O/NaOH. Carboxylic acid and alcohol substituents are deprotonated. Solvent peaks are those that are not integrated. ^{1}H NMR (300 MHz, D_2O/NaOH) δ 7.41 (dd, J=7.5 Hz, 2H), 7.34 (dd, J=7.5 Hz, 2H), 3.49 (s, 4H)

A.9 Electrochemical characterization additional figures

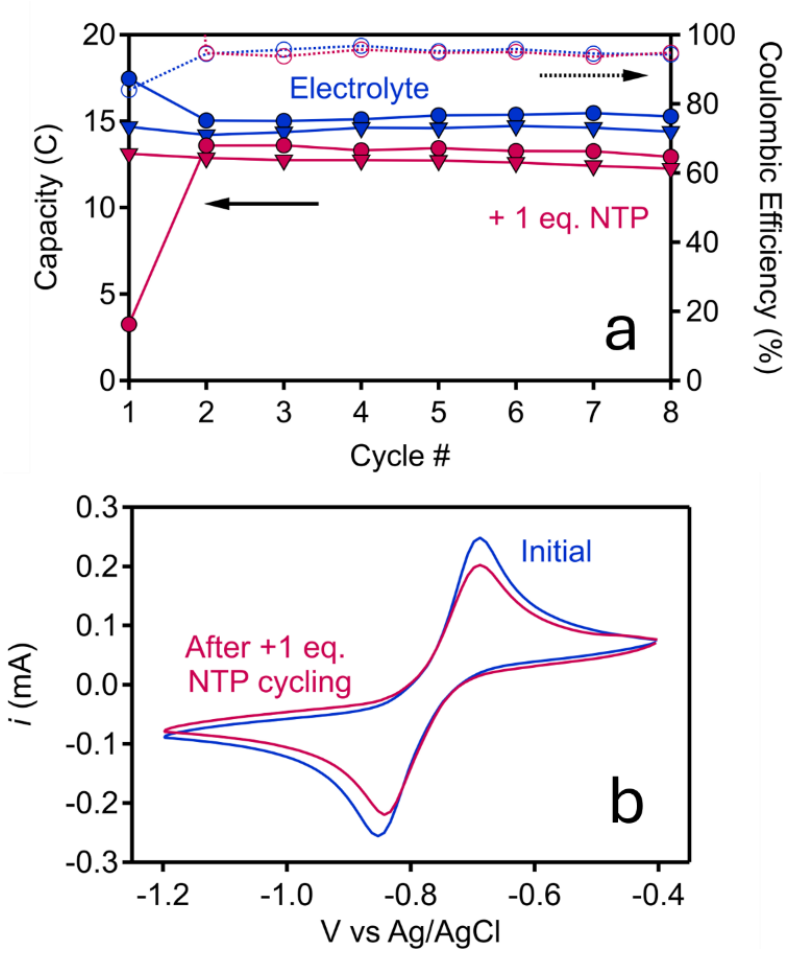

Figure A.11 (a) Galvanostatic H-cell cycling showing the capacities (left axis, solid lines) and Coulombic efficiency (right axis, dashed lines) vs cycle number of 10 mM 1,5-DHAQ in 1 M NaOH without (blue traces) and with the addition of 1 molar equivalent (0.1 mmol, red traces) of NTP powder to the anolyte reservoir. The catholyte was 1 M NaOH and the current was ±5 mA. Charge capacity is indicated by circles, and discharge capacity is indicated by triangles. **(b)** Cyclic voltammograms of 1,5-DHAQ before and after galvanostatic cycling.

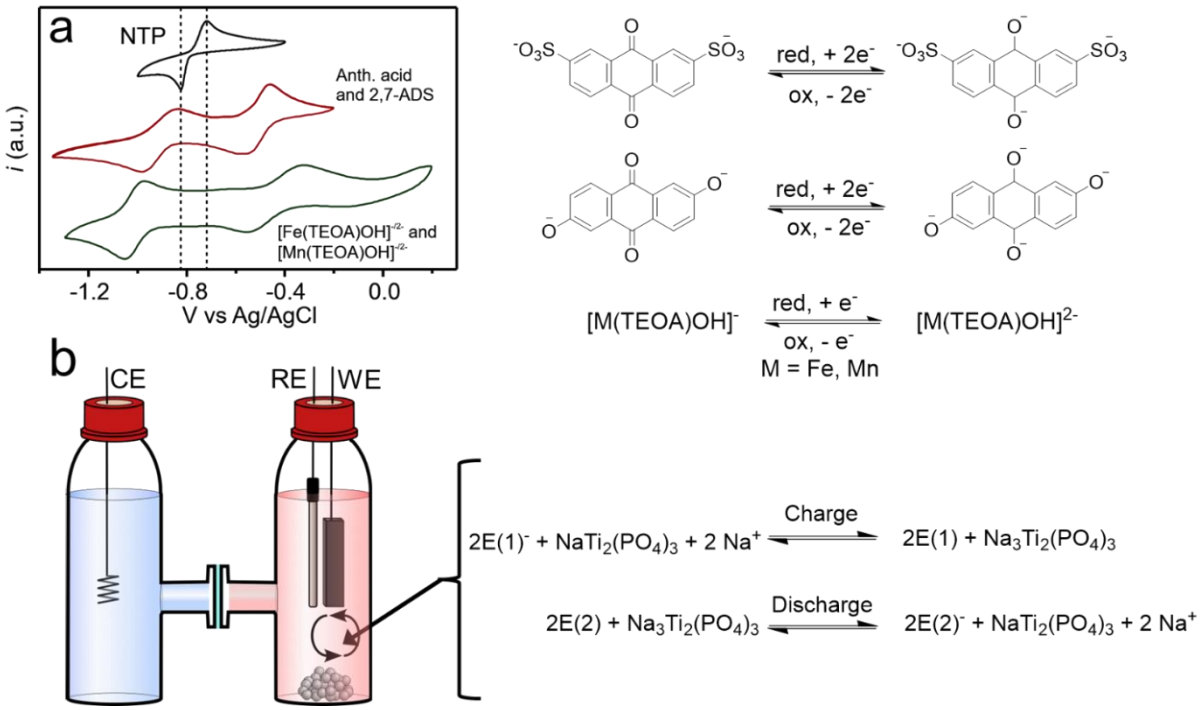

Figure A.12 (a) Cyclic voltammograms of NTP (on glassy carbon electrode, 0.5 mV s^{-1} in 1 M Na_2SO_4), an organic mixed electrolyte (5 mM anthraflavic acid, 5 mM 2,7-ADS, 0.1 M NaOH, 50 mV s^{-1}), and a transition-metal mixed electrolyte (10 mM $[Fe(TEOA)OH]^{-/2-}$, 10 mM $[Mn(TEOA)OH]^{-/2-}$, 5 M NaOH, 50 mV s^{-1}), offset vertically for clarity. The dashed vertical lines indicate the potentials of the peaks of NTP. Relevant redox reactions are shown on the right. **(b)** Schematic representation of an H-cell containing electrodes, electrolyte, and solid NTP, and a summary of the redox-targeting reactions, where E(1) and E(2) are the two components of a given mixed electrolyte.

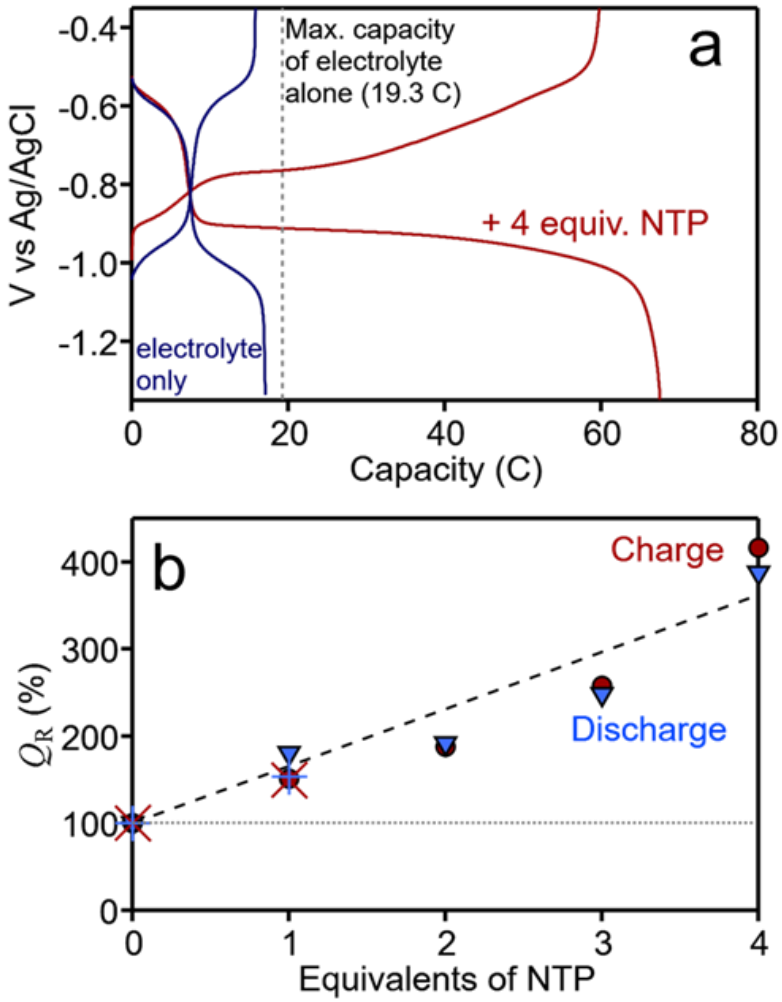

Figure A.13 (a) Voltage profiles of an H-cell containing 5 mM each of anthraflavic acid and 2,7-ADS measured at ±5 mA without (blue curves) and with addition of 4 equivalents (0.4 mmol, red curves) of NTP powder to the anolyte reservoir. The dashed vertical line indicates the maximum capacity of the electrolyte alone based on its concentration (19.3 C). The supporting electrolyte was 0.1 M NaOH (pH ~ 13). The catholyte was 1 M Na_2SO_4. **(b)** Capacity relative to the capacity of the electrolyte alone (Q_R(%) = (Q_{exp}/Q_{el}) x 100%), plotted against equivalents of NTP added to the anolyte. Charging is represented by circles and discharging is represented by triangles. The data shown as solid symbols were collected using 5 mM of each electrolyte component. The × (charge) and + (discharge) data were collected using 10 mM of each. Capacities were obtained by averaging over 12 cycles for the 0 – 2 equivalents data, and 5 cycles for the 3 equivalents data. The capacity for the 4 equivalents data is for the first cycle. The sloping dashed line is a guide to the eye showing increasing capacity with added NTP. The slope of this line corresponds to ~60% $Ti^{4+/3+}$ cycling in the NTP. The horizontal dotted line indicates the electrolyte's charge/discharge capacity before adding NTP (Q_{exp} = Q_{el}, Q_R = 100%).

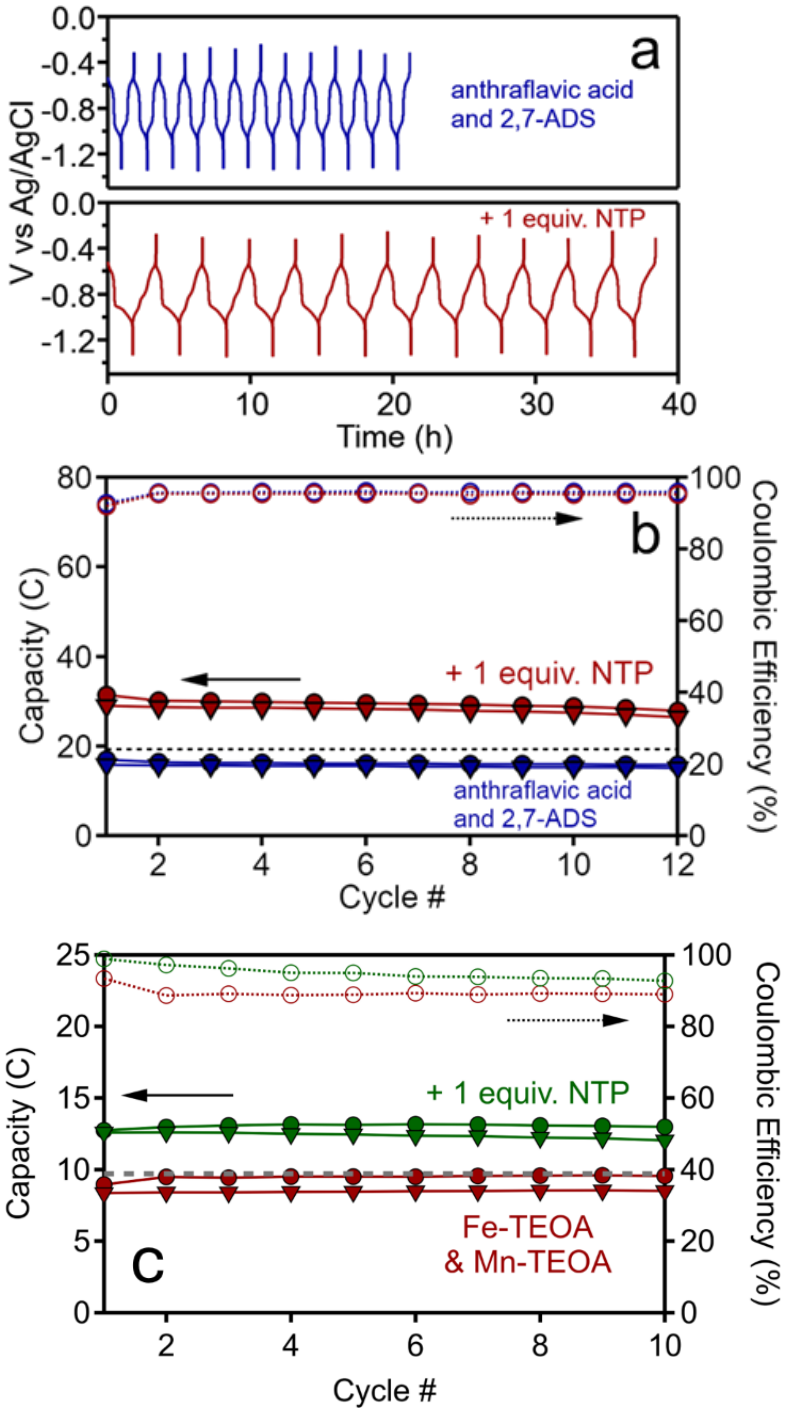
a
anthraflavic acid
and 2,7-ADS
+ 1 equiv. NTP
V vs Ag/AgCl
Time (h)
b
+ 1 equiv. NTP
anthraflavic acid
and 2,7-ADS
Capacity (C)
Coulombic Efficiency (%)
Cycle #
c
+ 1 equiv. NTP
Fe-TEOA
& Mn-TEOA
Capacity (C)
Coulombic Efficiency (%)
Cycle #

Figure A.14 (a) H-cell cycling data showing potential vs time for a solution containing 5 mM each of anthraflavic acid and 2,7-ADS in 0.1 M NaOH, before (blue) and after (red) addition of 1 molar equivalent (0.1 mmol) of NTP powder. The catholyte was 1.0 M Na_2SO_4 and the current was ±5 mA. **(b)** Capacity (left axis, solid lines) and Coulombic efficiency (right axis, dashed lines) vs cycle number from the data in panel (a). Charge capacity is indicated by circles, and discharge capacity is indicated by triangles. The blue data are for the electrolyte mixture, and the red data were collected after adding 1 equivalent of NTP. The dashed gray line represents the maximum capacity of the electrolyte alone (19.3 C) based on its stoichiometry. **(c)** Capacity (left axis, solid lines) and Coulombic efficiency (right axis, dashed lines) vs cycle number for H-cell cycling data representing 5 mM each of $[Fe(TEOA)OH]^{-/2-}$ and $[Mn(TEOA)OH]^{-/2-}$ without (red) and with 1 equivalent (0.1 mmol, green) of NTP powder. The supporting electrolyte was 5 M NaOH. The concentration of free TEOA was 160 mM. The catholyte was 3.6 M NaOH and the current was ±1 mA. Charge capacity is indicated by circles, and discharge capacity is indicated by triangles. The red data are for the pure electrolyte mixture, and the green data are after adding 1 equivalent of NTP. The dashed gray line represents the maximum capacity of the electrolyte alone (9.65 C) based on its stoichiometry.

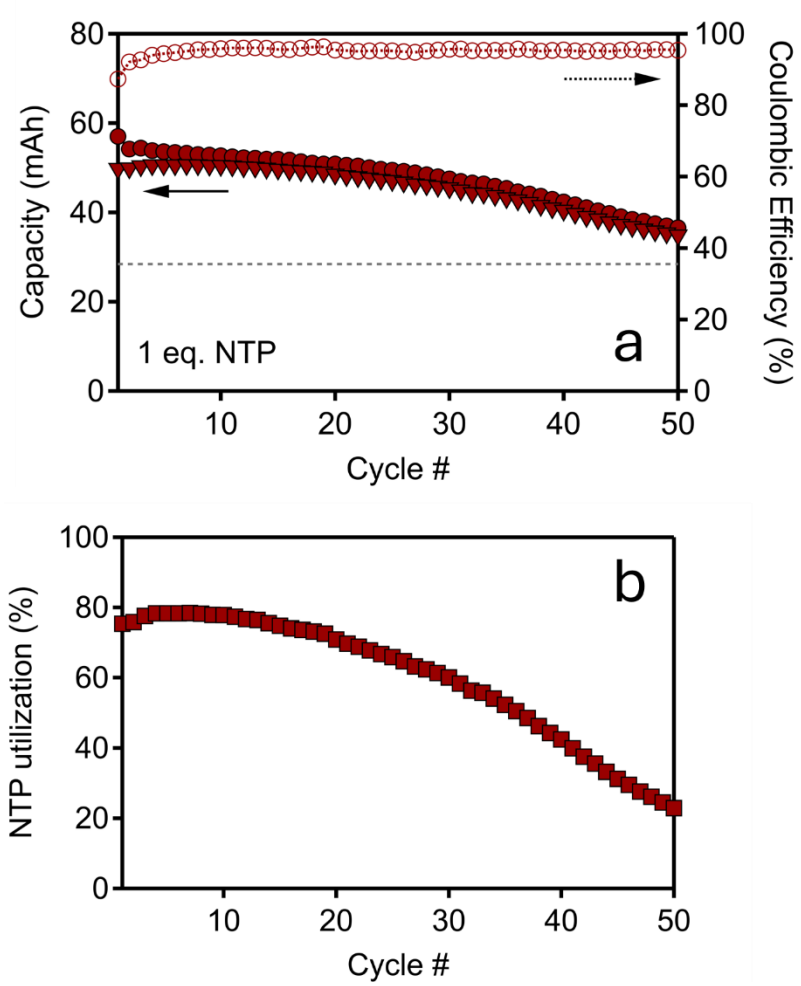

Figure A.15 Flow battery cycling data of 25 mM each of anthraflavic acid and 2,7-ADS measured at ±50 mA, fitted with an NTP inline powder filter containing one molar equivalent of NTP. This anolyte used 1 M NaOH for the supporting electrolyte and was the capacity-limiting reservoir. The catholyte was 100 mL 100 mM of $Na_4[Fe(CN)_6]$ in 1 M NaOH. **(a)** Capacity (left axis, solid lines) and Coulombic efficiency (right axis, dashed lines) vs cycle number. Charge capacity is indicated by circles, and discharge capacity is indicated by triangles. The dashed gray line represents the average capacity of the electrolyte alone (28.4 mAh) based off 5 cycles. **(b)** NTP utilization vs cycle number.

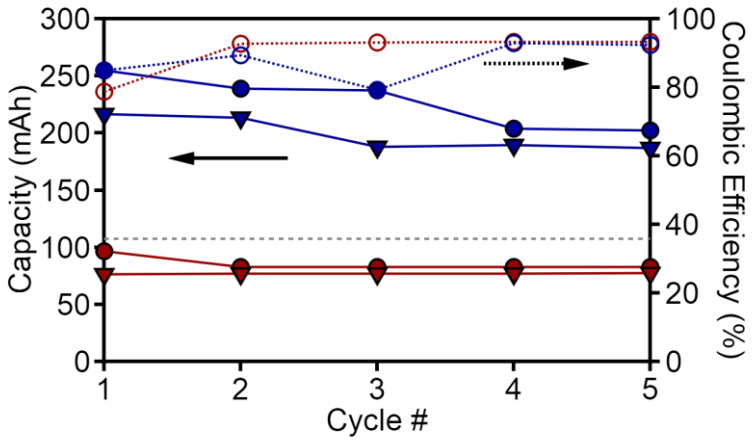

Figure A.16 Flow battery cycling data showing capacity (mAh, left axis, solid lines) and Coulombic efficiency (%, right axis, dotted lines) vs cycle number before and after adding an NTP redox strip filter to the anolyte flow path. The anolyte was a 40 mL solution 25 mM each in anthraflavic acid and 2,7-ADS in 1 M NaOH. The catholyte was a 200 mL 100 mM $Na_4[Fe(CN)_6]$ in 1 M NaOH. The redox filter contained ~1.6 g NTP (214 mAh, double the anolyte capacity). The horizonal dashed line represents the theoretical maximum capacity of the electrolyte alone. Charge is represented by circles, and discharge is represented by triangles. The Coulombic efficiency is represented by dotted lines and hollow symbols. The red symbols are the electrolyte alone, and the blue lines are after adding the redox filter. The current was ±50 mA.

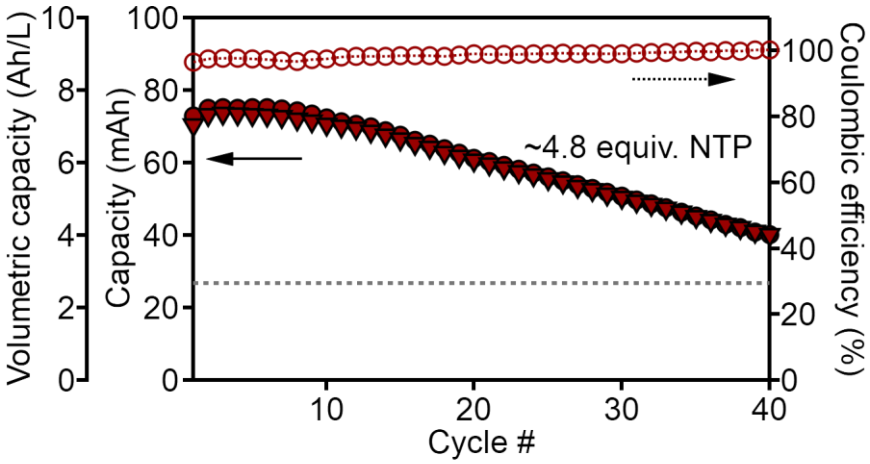

Figure A.17 Flow battery cycling data showing capacity (mAh, left axis, solid lines) and Coulombic efficiency (%, right axis, dotted lines) vs cycle number with an NTP foam flow-through filter fitted to the anolyte flow path. The anolyte was a 10 mL solution 25 mM each in anthraflavic acid and 2,7-ADS in 1 M NaOH. The catholyte was a 200 mL 100 mM $Na_4[Fe(CN)_6]$ in 1 M NaOH. The redox filter contained ~4.8 equivalents of 60 pores per inch NTP (125 mAh) and was added to the anolyte flow path. The horizonal dashed line represents the theoretical maximum capacity of the electrolyte alone. Charge is represented by circles, and discharge is represented by triangles. The Coulombic efficiency is represented by dotted lines and hollow symbols. The current was ±50 mA.

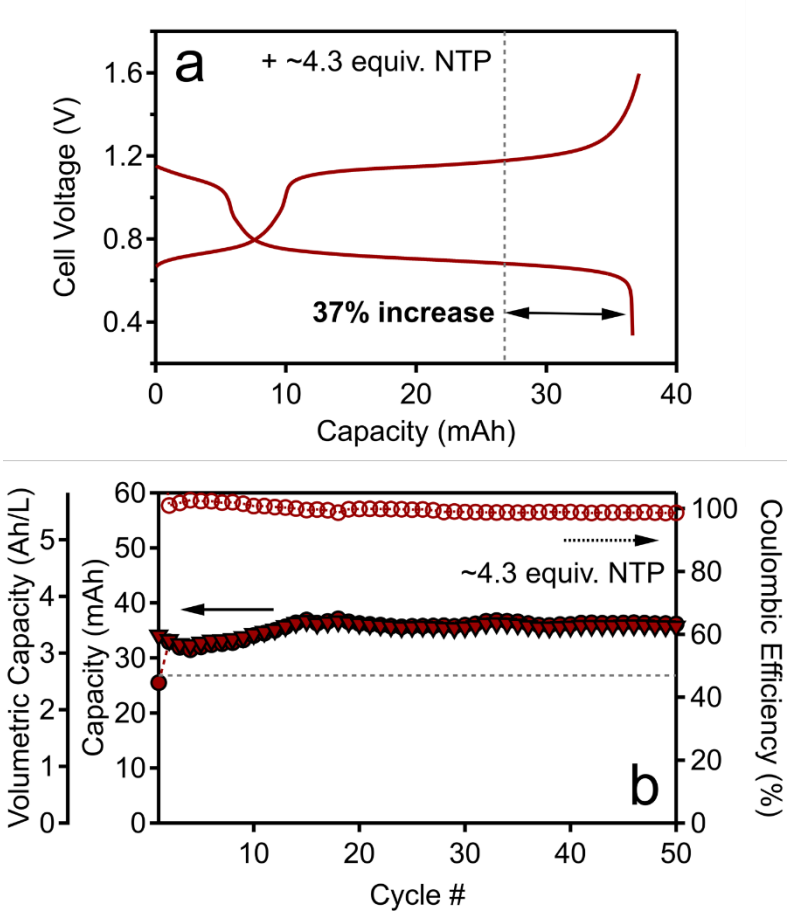

Figure A.18 (a) Voltage profile of a flow battery charge-discharge cycle with Nafion-coated dense NTP foams (100 pores per inch). The anolyte was a 10 mL solution 25 mM each in anthraflavic acid and 2,7-ADS in 1 M NaOH. The catholyte was a 200 mL 100 mM $Na_4[Fe(CN)_6]$ in 1 M NaOH. The redox filter contained ~4.5 equivalents of 100 pores per inch NTP (117 mAh) and was added to the anolyte flow path. **(b)** Flow battery cycling data showing capacity (mAh, left axis, solid lines) and Coulombic efficiency (%, right axis, dotted lines) vs cycle number of the data in panel (a). The horizontal dashed line represents the theoretical maximum capacity of the electrolyte alone. Charge is represented by circles, and discharge is represented by triangles. The Coulombic efficiency is represented by dotted lines and hollow symbols. The current was ±25 mA.

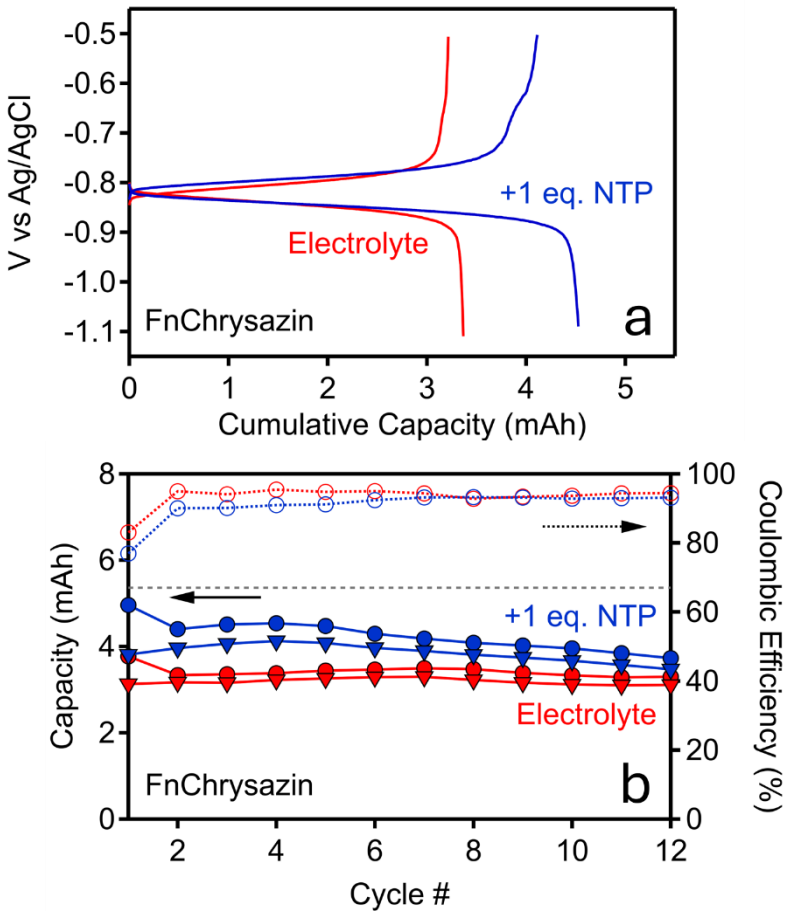

Figure A.19 (a) H-cell cycling data showing potential vs time for a solution containing 10 mM each of FnChrysazin in 1 M NaOH, before (red) and after (blue) addition of 1 molar equivalent (0.1 mmol) of NTP powder. The catholyte was 1 M NaOH and the current was ±5 mA. **(b)** Capacity (left axis, solid lines) and Coulombic efficiency (right axis, dashed lines) vs cycle number from the data in panel (a). Charge capacity is indicated by circles, and discharge capacity is indicated by triangles. The red data are for the electrolyte mixture, and the blue data were collected after adding 1 equivalent of NTP. The dashed gray line represents the maximum capacity of the electrolyte alone (5.36 mAh) based on its stoichiometry.

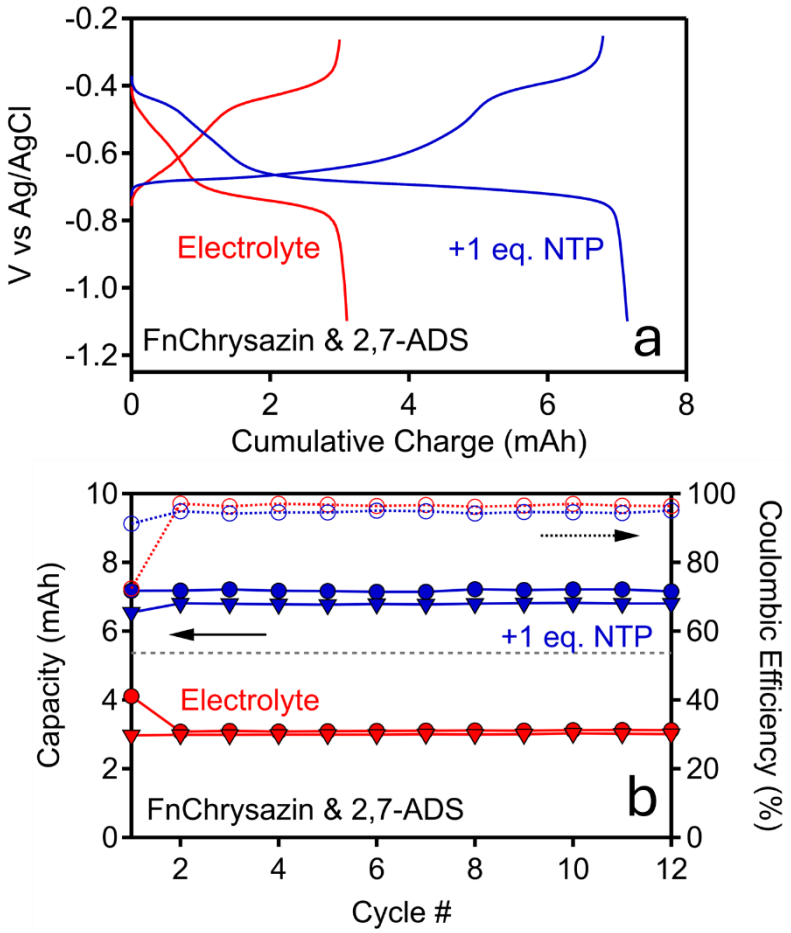

Figure A.20 (a) H-cell cycling data showing potential vs time for a solution containing 5 mM each of FnChrysazin and 2,7-ADS in 1 M NaOH, before (red) and after (blue) addition of 1 molar equivalent (0.1 mmol) of NTP powder. The catholyte was 1 M NaOH and the current was ±5 mA. **(b)** Capacity (left axis, solid lines) and Coulombic efficiency (right axis, dashed lines) vs cycle number from the data in panel (a). Charge capacity is indicated by circles, and discharge capacity is indicated by triangles. The red data are for the electrolyte mixture, and the blue data were collected after adding 1 equivalent of NTP. The dashed gray line represents the maximum capacity of the electrolyte alone (5.36 mAh) based on its stoichiometry.

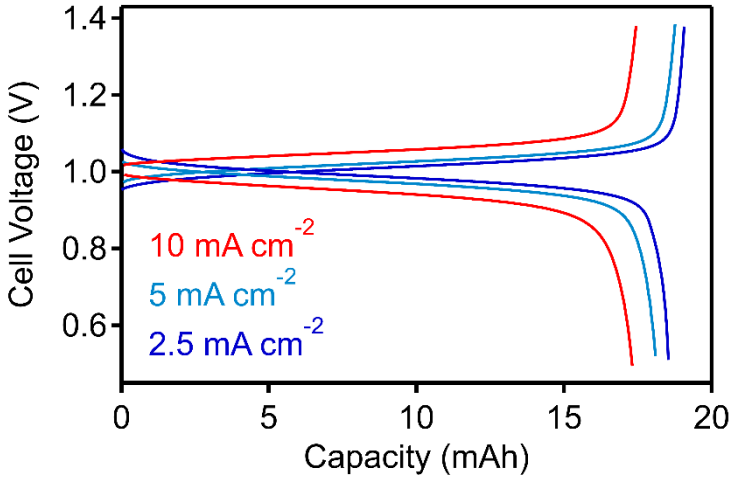

Figure A.21 Voltage profile of single charge-discharge cycles at 10, 5, and 2.5 mA cm^{-2}. The anolyte was an 8 mL 50 mM FnChrysazin in 1 M NaOH. The catholyte was a 100 mL 100 mM $Na_4[Fe(CN)_6]$ in 1 M NaOH. The theoretical maximum capacity is 21.4 mAh.

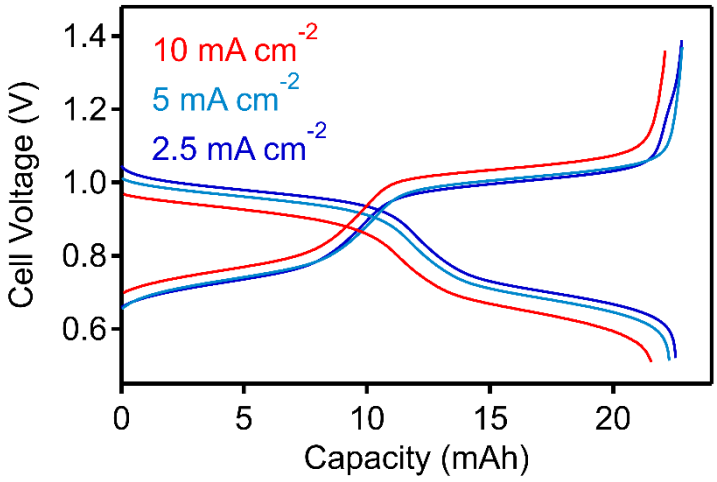

Figure A.22 Voltage profile of single charge-discharge cycles at 10, 5, and 2.5 mA cm^{-2}. The anolyte was a 10 mL 25 mM each of FnChrysazin and 2,7-ADS in 1 M NaOH. The catholyte was a 100 mL 100 mM $Na_4[Fe(CN)_6]$ in 1 M NaOH. The theoretical maximum capacity is 26.8 mAh.

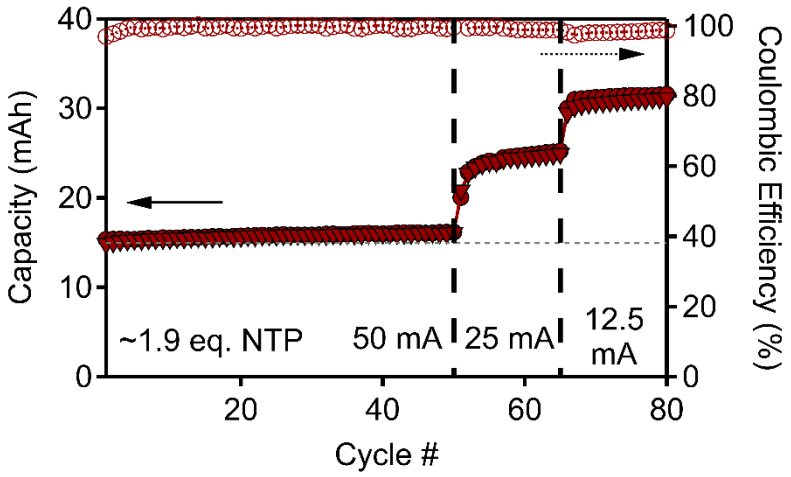

Figure A.23 Flow battery measurement of capacity (left axis, solid lines) and Coulombic efficiency (right axis, dashed lines) vs cycle number of 8 mL 25 mM each of FnChrysazin and 2,7-ADS in 1 M NaOH with ~1.9 molar equivalents (0.306 g) of NTP foam composites. The catholyte is 100 mL $Na_4[Fe(CN)_6]$ in 1 M NaOH. Charge capacity is indicated by circles, and discharge capacity is indicated by triangles. The dashed gray line represents the discharge capacity of the electrolyte alone based on prior cycling without NTP foam composite redox filter. The initial 50 cycles employed a current of ±10 mA cm^{-2}, subsequent 15 cycle were ±5 mA cm^{-2} and the following 15 cycles were ±2.5 mA cm^{-2}.

A.10 References

(1) Arroyo-Currás, N.; Hall, J. W.; Dick, J. E.; Jones, R. A.; Bard, A. J. An Alkaline Flow Battery Based on the Coordination Chemistry of Iron and Cobalt. *J. Electrochem. Soc.* **2014**, *162* (3), A378-A383. DOI: 10.1149/2.0461503jes.

(2) Gong, K.; Xu, F.; Grunewald, J. B.; Ma, X.; Zhao, Y.; Gu, S.; Yan, Y. All-Soluble All-Iron Aqueous Redox-Flow Battery. *ACS Energy Letters* **2016**, *1* (1), 89-93. DOI: 10.1021/acsenergylett.6b00049.

(3) Alfaro, H.; Doležal, J.; Zýka, J. Study of the oxidation-reduction reactions of manganese and cobalt in alkaline triethanolamine medium. *Z. Anal. Chem.* **1966**, *224* (1), 365-374. DOI: 10.1007/bf00502665.

(4) Wu, M.; Bahari, M.; Fell, E. M.; Gordon, R. G.; Aziz, M. J. High-performance anthraquinone with potentially low cost for aqueous redox flow batteries. *Journal of Materials Chemistry A* **2021**, *9* (47), 26709-26716, 10.1039/D1TA08900E. DOI: 10.1039/D1TA08900E.

(5) Hung, T.-F.; Lan, W.-H.; Yeh, Y.-W.; Chang, W.-S.; Yang, C.-C.; Lin, J.-C. Hydrothermal Synthesis of Sodium Titanium Phosphate Nanoparticles as Efficient Anode Materials for Aqueous Sodium-Ion Batteries. *ACS Sustainable Chem. Eng.* **2016**, *4* (12), 7074-7079. DOI: 10.1021/acssuschemeng.6b01962.

(6) Yang, J.; Wang, H.; Hu, P.; Qi, J.; Guo, L.; Wang, L. A High-Rate and Ultralong-Life Sodium-Ion Battery Based on $NaTi_2(PO_4)_3$ Nanocubes with Synergistic Coating of Carbon and Rutile TiO_2. *Small* **2015**, *11* (31), 3744-3749. DOI: 10.1002/smll.201500144.

(7) Ivanov, Y. A.; Belokoneva, E. L.; Egorov Tismenko, Y. K.; Simonnov, N. V. The crystal structure of Na, Ti-orthophosphate NaTi2(PO4)3. *Doklady Akademii Nauk SSSR* **1980**, *252*, 1122 - 1125.

(8) Hasan, F.; Mahanta, V.; Abdelazeez, A. A. A. Quinones for Aqueous Organic Redox Flow Battery: A Prospective on Redox Potential, Solubility, and Stability. *Advanced Materials Interfaces* **2023**, *10* (24), 2300268. DOI: https://doi.org/10.1002/admi.202300268.

Appendix B. Spectroelectrochemical Revelations of Prussian Blue Redox Targeting Reaction Kinetics

B.1 Materials

Potassium ferrocyanide trihydrate ($K_4[Fe(CN)_6].3H_2O$, ≥98%, Alfa Aesar), potassium ferricyanide ($K_3[Fe(CN)_6]$, 99.9%, Alfa Aesar), iron (II) chloride tetrahydrate ($FeCl_2.4H_2O$, ≥99%, Acros Organics), potassium chloride ACS reagent (KCl), and sodium chloride ACS grade (NaCl) were purchased from Fisher Scientific. Sodium hydroxide pellets (NaOH, ≥98%), ammonium chloride ACS grade (NH_4Cl, 99.5%), rubidium chloride (RbCl, ≥99.0%, ReagentPlus®), cesium chloride (CsCl, ≥99.9%, ReagentPlus®), and lithium chloride ACS grade (LiCl, ≥99.%) were purchased from Sigma Aldrich. Sodium acetate anhydrous ACS grade (99.9%, J.T. Baker) and acetic acid glacial ACS grade (Macron Fine Chemicals) were purchased form VWR. Ethylenediaminetetraacetic acid disodium salt dihydrate (EDTA, ≥99%) was purchased from EMD Millipore.

B.2 Synthesis of Prussian blue (PB)

PB was synthesized via coprecipitation methods, modified from the procedure as described by Neale *et al*.[1] A 1 M acetate buffer solution was first prepared by combining 13.3 g sodium acetate (162 mmol), 14.3 g acetic acid glacial (238 mmol), and 320 mL deionized water. 10 mL 5 M NaOH solution is prepared by dissolving 2 g (50 mmol) in 10 mL deionized water. The 5 M NaOH solution is added dropwise to adjust the pH of the acetate solution to pH 4.4. Once adjusted, add additional deionized water to produce 400 mL acetate solution. 200 mL of buffer solution was used to prepare 100 mM $K_4[Fe(CN)_6].3H_2O$ (8.45 g, 20 mmol). The remaining 200 mL

buffer solution prepared 150 mM $FeCl_2.4H_2O$ (5.96 g, 30mmol) and 150 mM EDTA (11.2 g, 30mmol). Add the iron/EDTA solution quickly to the ferrocyanide solution and age for 24 hours with stirring. Particles were washed and collected with deionized water and ethanol three times through centrifugation. The product was dried in air overnight in an 80ºC oven.

B.3 Physical characterization

Powder X-ray diffraction data were taken by drop-casting samples on silicon wafers and measuring in a Bruker D8 Discover Microfocus diffractometer using a Cu-K X-ray source, operating at 50 kV and 1000 μA. Sample stage was set to oscillate throughout the measurement.

Transmission electron microscopy (*TEM) imaging* was taken of dilute drop-cast samples on 300-mesh carbon-coated copper grids (TED Pella) on the FEI TECNAI F20 microscope operated at 200 kV.

B.4 Spectroelectrochemical characterization

UV-Vis absorbance was collected on the Agilent Cary 5000 spectrometer in an air-tight GL14 screw cap-fitted 2 mm quartz cuvette.

Potentiometric intermittent titration technique (PITT) measurements were carried out in an air-tight GL14 screw cap-fitted 2 mm quartz cuvette. A platinum mesh electrode was used for the working electrode (WE), a platinum wire for the counter electrode (CE), and a 1 mm leakless Ag/AgCl electrode (eDAQ) was the reference electrode (RE). The cuvette was sparged out for 15 minutes with N_2 prior to the measurements. The PITT measurements were carried out on the Squidstat potentiostat (Admiral Instruments). To minimize the WE/RE potential difference, the two electrodes were in ~1 mm proximity. The initial potential step is the open circuit potential

(OCP) with each applied potential step was ±50 mV with a 600 s pulse duration, followed by a subsequent 5 s rest period.

B.5 Physical characterization additional figures

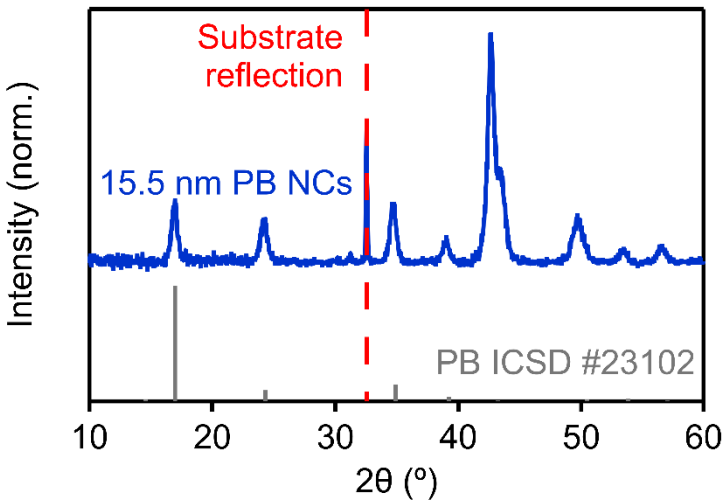

Figure B.1 Powder X-ray diffraction pattern of as-made PB nanocrystals. The grey diffraction patterns at the bottom are literature reference for PB (ICSD # 23102). Additional reflection at 32.5° 2θ is a substrate reflection. Scherrer analysis reveals the nanoparticle ensemble diameter is 15.5 nm.

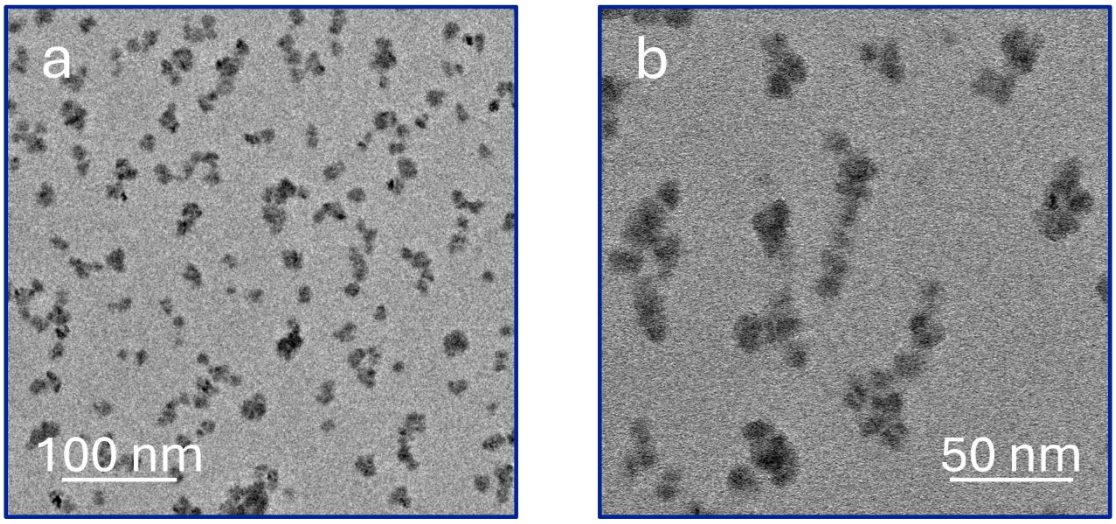

Figure B.2 (a-b) Transmission electron microscope images of as-made PB nanocrystals.

B.6 Spectroelectrochemical additional figures

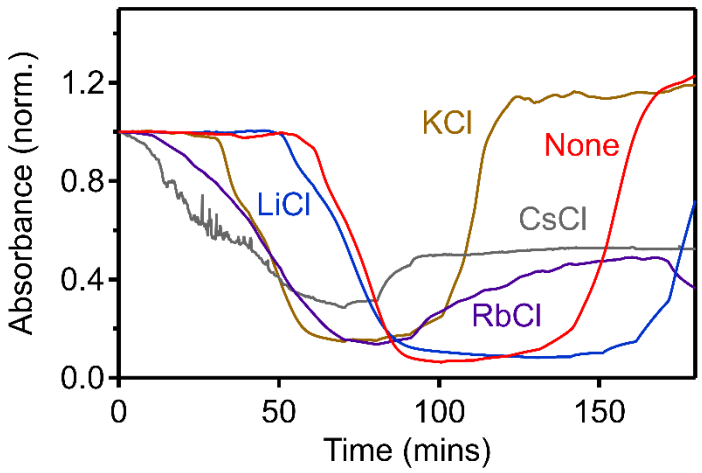

Figure B.3 Absorption change vs time for the PB nanocrystals and 5 molar equivalent of potassium ferricyanide without (red trace) and with LiCl/KCl/RbCl/CsCl supporting electrolyte. The supporting electrolyte was 0.041 M LiCl/KCl/RbCl/CsCl, with 9 mM K^+ already in the PB electrolyte from potassium ferricyanide.

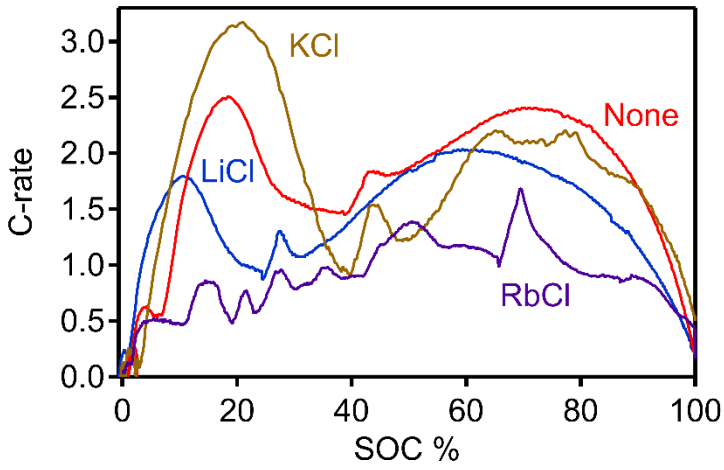

Figure B.4 The C-rate vs SOC PB nanocrystals and 5 molar equivalent of potassium ferricyanide with no addition supporting electrolyte (red trace) and 0.041 M LiCl/KCl/RbCl supporting electrolyte. A boxcar average has been applied to the real-time C-rate data for data smoothing, with the data representing the average C-rate per minute of data points.

B.7 Additional calculations

For a uniform sphere the surface area to volume ratio can be described by equation B.1:

$$SA{:}V = {}^{3}/_{r} \tag{B.1}$$

Where *SA* is the surface area, *V* is the volume, and *r* is the nanoparticle radius. The radius is 7.75 nm, yielding 736 unit cells upon the nanocrystal surface.

PB unit cell is cubic with an edge length of 10.13 Å. This would translate to the area of a single face of a unit cell to equal 102.6 Å. This would also translate to a unit cell volume of 1040 Å.

The total number of unit cells per nanocrystal can be determined by equation B.2:

$$UC_{TOT} = \frac{(4/3)\pi r^3}{UC_{Vol}} \tag{B.2}$$

Where UC_{TOT} is the number of unit cells per nanocrystal and UC_{Vol} is the volume of a single unit cell. This yields 1876 unit cells per nanocrystal. Therefore, ~40% of the unit cells are present upon the surface of the nanocrystals.

B.8 References

(1) Neale, Z. G.; Liu, C.; Cao, G. Effect of synthesis pH and EDTA on iron hexacyanoferrate for sodium-ion batteries. *Sustainable Energy & Fuels* **2020**, *4* (6), 2884-2891, 10.1039/D0SE00120A. DOI: 10.1039/D0SE00120A.